Die approbierte gedruckte Originalversion dieser Dissertation ist an der TU Wien Bibliothek verfügbar.
The approved original version of this doctoral thesis is available in print at TU Wien Bibliothek.

DISSERTATION

Capturing the Essential Aspects of Reliable Vehicular Communications

Thomas Blazek

Advisor: Univ. Prof. Christoph F. Mecklenbräuker

ausgeführt zum Zwecke der Erlangung des akademischen Grades eines Doktors der technischen Wissenschaften

November 2019

Thomas Blazek
geboren am 1. November 1988
Matrikelnummer 00825395
Obkirchergasse 38/4/8, 1190 Wien

institute of telecommunications

Die approbierte gedruckte Originalversion dieser Dissertation ist an der TU Wien Bibliothek verfügbar.
The approved original version of this doctoral thesis is available in print at TU Wien Bibliothek.

“There is an art, it says, or rather, a knack to flying.
The knack lies in learning how to throw yourself at the ground and miss.
... Clearly, it is this second part, the missing, which presents the difficulties.”
— Douglas Adams, Life, the Universe and Everything

Die approbierte gedruckte Originalversion dieser Dissertation ist an der TU Wien Bibliothek verfügbar.
The approved original version of this doctoral thesis is available in print at TU Wien Bibliothek.
TU Bibliothek Your knowledge hub WIEN

Die approbierte gedruckte Originalversion dieser Dissertation ist an der TU Wien Bibliothek verfügbar.
The approved original version of this doctoral thesis is available in print at TU Wien Bibliothek.

Acknowledgements

I want to thank Christoph F. Mecklenbräuker for the possibility to pursue this research and the continous support. His special brand of *tight leash*[1] allowed me to freely identify challenges, develop concepts and solutions and ensure that this thesis is truly my own.
Furthermore, I want to thank all colleagues whose cooperation made this thesis possible. First and foremost, Golsa Ghiaasi Hafezi and the channel emulator set me on the initial trajectory and continuously accompanied me. I also want to thank Dieter Smely and Alexander Paier for input in the early stages of my research. Additionally, I appreciate the cooperation of Stefan Pratschner, Erich Zöchmann, Herbert Groll, Martin Lerch, as well as all the other colleagues I had fruitful discussions with. I am also deeply grateful for the cooperation with the FH Hagenberg, with Christian Backfrieder, Manuel Lindorfer and Gerald Ostermayer. I want to thank the whole institute of telecommunications, as I felt at home and supported by every one working at the institute, and made very dear friends.
I want to thank my family for their infinite patience and support. My father always provided a source of calmness and a possibility for a talk. My mother pushed to reach out even when I was being difficult to reach and showed her caring. My sister helped me greatly to keep me grounded and keep my priorities in balance.
Finally, the person who is most important to me, and who helped me like no one else, is Doris, the love of my life. Thank you so much.

Wien, 5. November 2019 Thomas Blazek

[1] Formulation by Torbjørn Ekman

Die approbierte gedruckte Originalversion dieser Dissertation ist an der TU Wien Bibliothek verfügbar.
The approved original version of this doctoral thesis is available in print at TU Wien Bibliothek.
TU Bibliothek Your knowledge hub WIEN

Die approbierte gedruckte Originalversion dieser Dissertation ist an der TU Wien Bibliothek verfügbar.
The approved original version of this doctoral thesis is available in print at TU Wien Bibliothek.

Abstract

Vehicular communications promise to be an essential driver for roadside safety in the future, as well as an important building block of autonomous driving. Communication standards that consider this communication mode specifically have been published as early as 2007 and continue to be refined. However, the nature of this application makes it especially challenging to achieve a required reliability, with channels having large delay spreads and large Doppler spectra. Low-latency requirements are in place to ensure that emergency information is disseminated sufficiently quickly, favoring ad-hoc network setups. High vehicular densities can however cause problems through hidden node communications in such an environment. Testing all these aspects for a given communication scheme at once is a daunting task. It is infeasible to deploy enough vehicles to replicate all aspects in dense traffic scenarios. Hence, many people resort to simulations. These simulations have to introduce simplifications, and not all of these simplifications are valid.

This thesis aims at identifying the aspects of vehicular communications that have to be modeled, from the physical channel over channel estimation to network performance. I do this by integrating mathematical models with software defined radios that act as transmitter and receiver for IEEE 802.11p, as well as vehicular channel emulators. The first step is to analyze the vehicular channel and identify the required emulator complexity. I work with vehicular channel measurements, and apply sparse techniques and Akaike's information criterion to identify the number of multipath clusters observed in a vehicular channel. The results show that modeling four to six clusters already provides a representative channel compared to the measurements. Then, I use sparsely fitted measurement data, as well as stationary channel models defined by ETSI, to measure the performance of IEEE 802.11p in a single link communication setup. This evaluation proves that considering the underlying channel is essential, as the achievable packet performance depends strongly on the delay-Doppler configuration of the small-scale fading channel. I further include mobility simulations of cars to simulate dense communication networks. Based on this network data, I introduce an algorithm to reduce the network complexity, which allows me to measure the network effects at the same time as the channel effects with a small number of communication nodes. Finally, I introduce a stochastic approach to modeling burst-behavior based on the Gilbert-Elliott model. I use maximum-likelihood estimates for the Gilbert-Elliott model, which is modified to become nonstationary, and combine them with modeling of the interference. The results show that the channel characteristics and the interference have to be modeled in tandem, as neglecting one means the simulation is overestimating the achievable performance.

Die approbierte gedruckte Originalversion dieser Dissertation ist an der TU Wien Bibliothek verfügbar.
The approved original version of this doctoral thesis is available in print at TU Wien Bibliothek.
TU Bibliothek Your knowledge hub WIEN

Die approbierte gedruckte Originalversion dieser Dissertation ist an der TU Wien Bibliothek verfügbar.
The approved original version of this doctoral thesis is available in print at TU Wien Bibliothek.

Zusammenfassung

Vehikulare Kommunikation verspricht in der Zukunft sowohl ein essentieller Treiber von Straßensicherheit zu sein, als auch ein wichtiger Bestandteil des Autonomen Fahren. Die ersten Kommunikationsstandards, die speziell für diese Anwendung definiert wurden, erschienen bereits 2007, und wurden seither kontinuierlich weiterentwickelt. Allerdings verursacht die Natur dieser Anwendung, dass notwendige Verlässlichkeit der Kommunkation besonders schwer zu erreichen ist, da den Kanälen große Frequenz- und Zeitaufspreizungen widerfahren. Da Notfallkommunikation nur wertvoll ist, wenn sie rechtzeitig ankommt, gibt es stringente Latenzanforderungen, was wiederum dazu führt, dass die Kommunikationsnetzwerke ad-hoc eingerichtet werden. Hohe Fahrzeugdichten verursachen allerdings Probleme durch versteckte Störer. All diese Aspekte auf einmal zu testen für eine spezielle Kommunikationsart ist allerdings fast nicht machbar. Es ist unmöglich, genug Autos mit Equipment auf die Straße zu schicken, um die erreichbare Performance in dichten Szenarien zu testen. Daher gehen stattdessen viele über zu Simulationen. Diese treffen wiederum Annahmen und Vereinfachungen, und nicht alle Vereinfachungen sind notwendigerweise gültig.

In dieser Arbeit ist das Ziel, die Aspekte an vehikularer Kommunikation zu identifizieren, die modelliert werden müssen, vom physischen Kanal über Kanalschätzung bis hin zu Netzwerkperformance. Ich verwende hierzu Software Defined Radios die als Sender und Empfänger für IEEE 802.11p fungieren, wie auch als Kanalemulator. Als erstes analysiere ich den vehikularen Kanal um die benötigte Modellkomplexität zu identifizieren. Dazu verwende ich vehikulare Kanalmessungen, und verwende sparse Schätzmethoden gemeinsam mit Akaikes Informationskriterium um die Anzahl an Mehrwege-Clustern zu identifizieren. Die Ergebnisse zeitgen, dass es reicht, vier bis sechs Mehrwege-Cluster zu modellieren um einen repräsentativen Kanal zu emulieren. Ich nehme dann den so approximierten Kanal, gemeinsam mit stationären Kanalmodellen von ETSI, und messe die IEEE 802.11p Performance für einen Link mit hilfe des Kanalemulators aus. Diese Analyse zeigt dass es essentiell ist, den Kanal zu modellieren, da die erreichbare Paket-Performance stark von Frequenz- und Zeitaufspreizung des zugrundeliegenden Kanales abhängt. Dann verwendet ich Mobilitätssimulationen von Autos als Grundlage, um ein ganzes Auto-Netzwerk zu simulieren. Um dieses Netzwerk modelieren zu können, führe ich einen Algorithmus ein, der die Topologie des Netzwerkes vereinfacht, wodurch ich sowohl den Kanal als auch Netzwerkeffekte in einer Messung mit einer kleinen Anzahl an Geräten messen kann. Schlussendlich präsentiere ich einen stochastischen Modellierungszugang für Burst-Verhalten der auf dem Gilbert-Elliott-Modell basiert. Ich verwende Maximum-Likelihood-Schätzer für das Gilbert-Elliott-Modell, welches abgeän-

Die approbierte gedruckte Originalversion dieser Dissertation ist an der TU Wien Bibliothek verfügbar.
The approved original version of this doctoral thesis is available in print at TU Wien Bibliothek.
TU Bibliothek Your knowledge hub WIEN

dert wurde um nichtstationäre Prozesse zu modellieren. Das Ergebnis wird dann mit einem stochastischen Modell für Interferenz-Muster kombiniert. Die Ergebnisse zeigen, dass sowohl die Kanalcharakteristik als auch die Interferenz gemeinsam modelliert werden müssen, da das Ignorieren von einem Aspekt das Model dazu führt, dass die erreichbare Performance überschätzt wird.

Die approbierte gedruckte Originalversion dieser Dissertation ist an der TU Wien Bibliothek verfügbar.
The approved original version of this doctoral thesis is available in print at TU Wien Bibliothek.

Contents

Acknowledgements v

Abstract vii

Zusammenfassung ix

1 Introduction 1
- 1.1 Intelligent Transportation Systems . . . 2
- 1.2 Vehicular Communication Schemes . . . 3
- 1.3 IEEE 802.11p System Overview . . . 6
  - 1.3.1 The Physical Layer . . . 7
  - 1.3.2 The MAC Layer . . . 10
- 1.4 Current State of the Research . . . 11
- 1.5 Contribution of this Thesis . . . 11
- 1.6 Notation . . . 12
- 1.7 Structure of the Thesis . . . 13

2 Reduced Complexity Channel Modeling 15
- 2.1 Vehicular Channel Modeling . . . 15
- 2.2 Emulator Implementation . . . 17
- 2.3 Sparse Channel Models and Estimation . . . 20
  - 2.3.1 Channel Representations . . . 21
  - 2.3.2 Sparse Estimation: The c-LASSO . . . 26
- 2.4 Propagation Channel Data . . . 30
  - 2.4.1 Saleh-Valenzuela Channels . . . 30
  - 2.4.2 mmWave Vehicle-to-Vehicle (V2V) Channel Sounding Campaign . . . 32
- 2.5 Results . . . 34
  - 2.5.1 Performance Evaluation . . . 34
  - 2.5.2 Performance Analysis for Synthetic Data . . . 36
  - 2.5.3 Performance Analysis for Tapped and Clustered Delay Line Estimates . . . 37
  - 2.5.4 Delay-Doppler Grid . . . 41
- 2.6 Discussion . . . 46

3 Reduced Complexity Network Performance Modeling 47

Die approbierte gedruckte Originalversion dieser Dissertation ist an der TU Wien Bibliothek verfügbar.
The approved original version of this doctoral thesis is available in print at TU Wien Bibliothek.
TU Bibliothek Your knowledge hub WIEN

3.1 Performance Modeling . . . 47
3.1.1 Decomposition of the Packet Error Probability . . . 48
3.1.2 Estimating the Packet Error . . . 49
3.2 Single Link Performance Evaluations . . . 50
3.2.1 Emulator Testbed . . . 51
3.2.2 Channel Models and Parameter Settings . . . 51
3.2.3 Results . . . 54
3.2.4 Mean and Burst Small-Scale Fading Behavior . . . 58
3.3 Network Performance Analysis . . . 61
3.3.1 Mobility Simulations: TraffSim . . . 61
3.3.2 Connectivity Modeling Approach . . . 62
3.3.3 Physical Parameters and Medium Access Control . . . 63
3.3.4 Representative Channel Performance Model . . . 64
3.3.5 Graph Based Complexity Reduction . . . 65
3.3.6 MAC Level Approximation . . . 65
3.3.7 Channel Approximation . . . 67
3.4 Network Performance Evaluation . . . 68
3.4.1 Performance under Clique of Hidden Nodes . . . 69
3.4.2 Performance in Traffic Simulations . . . 70
3.5 Discussion . . . 72

4 Network Abstraction 73
4.1 The Gilbert-Elliott Model . . . 74
4.2 Maximum Likelihood Estimation . . . 76
4.2.1 Block Constant Channel . . . 77
4.2.2 Scenario Classification by Mean SNR . . . 78
4.2.3 Fading Aware Parameter Estimation . . . 79
4.3 Results . . . 82
4.4 Model Fitting . . . 82
4.4.1 Block-Constant Fit . . . 82
4.4.2 Mean SNR Grouped Fit . . . 82
4.4.3 Fading Aware Fit . . . 84
4.5 Evaluation of the Goodness of Fit . . . 85
4.5.1 PER Estimation Performance . . . 87
4.5.2 Burst Estimation Performance . . . 87
4.5.3 Discussion: Necessity of Burst Modeling . . . 88
4.5.4 Discussion: Model Complexity . . . 89
4.6 Combining Network Effects and Channel Effects . . . 90
4.6.1 The Information Bottleneck . . . 90
4.6.2 Resulting Highway Scenarios . . . 92
4.6.3 Results . . . 93
4.6.4 Total Resulting Packet Error Probabilities . . . 97

Die approbierte gedruckte Originalversion dieser Dissertation ist an der TU Wien Bibliothek verfügbar.
The approved original version of this doctoral thesis is available in print at TU Wien Bibliothek.
TU Bibliothek Your knowledge hub WIEN

4.7 Discussion 97

5 Conclusions **99**

A 5.6 GHz Channel Estimation **101**
A.1 Channel Sounding Campaign 101
A.2 Estimation Results 102

B Real-Time Emulator Design **105**

C Stationary Channel Models **107**
C.1 Fading Trace Generation 107
C.2 Tapped Delay Line Models 108

List of Acronyms **112**

List of Figures **117**

List of Tables **121**

Bibliography **131**

Die approbierte gedruckte Originalversion dieser Dissertation ist an der TU Wien Bibliothek verfügbar.
The approved original version of this doctoral thesis is available in print at TU Wien Bibliothek.

Die approbierte gedruckte Originalversion dieser Dissertation ist an der TU Wien Bibliothek verfügbar.
The approved original version of this doctoral thesis is available in print at TU Wien Bibliothek.

1 Introduction

Die approbierte gedruckte Originalversion dieser Dissertation ist an der TU Wien Bibliothek verfügbar.
The approved original version of this doctoral thesis is available in print at TU Wien Bibliothek.

At the turn of the millennium, the evolution in communication systems accelerated to the point that many people considered communication and information the defining features of the current time. Hence, the term "Information Age" became relevant in the mid of the 1990s [1–4]. At this point, it was foreseeable that new emerging communication and data technologies would impact the social and economic behavior. However, communication was still tied to physical locations by means of wired terminals (computers or telephones). The endpoints of the communications were almost always human. People were considering applications of technologies beyond this setup. Mark Weiser introduced the concept of what is today called ubiquitous computing [5]. Ubiquitous computing introduces the concept of *invisible computing*. That is, a computer should not be a device that a human has to explicitly interface to and, just as importantly, learn how to interface. Instead, the interface should be completely intuitive, and the computer should operate autonomously, without requiring the human's supervision or intervention.

From a communications point of view, Weiser's propositions implied completely new applications for communications. Firstly, the computers have to be the endpoints of communications themselves, instead of just the communication means. This is required by the autonomous concepts. Furthermore, the requirements of flexibility and ubiquity ask for wireless, flexible communication means. These requirements for *things* to connect culminated in the occurrence of the term "Internet of Things (IoT)" (documented as early as 1999 [6]).

The principal challenge with this concept is that various applications of the IoT have vastly different requirements on the communication schemes, power consumption, throughput challenges, and communication constraints such as latency and quality. Instead, the specific application of the IoT concept has to define these parameters. This in turn hinders universal interoperability between arbitrary devices. Thus, for IoT applications to emerge, it is important that a given application expects enough deployed devices for it to be commercially viable. Two application domains that were expected early to fulfill this requirement are the internet of medical things and smart homes/home automation. Another application that was envisioned, and already worked on in the early 2000s, are Intelligent Transportation Systems (ITS).

ITS are of special interest due to their potential to enhance traffic safety. *Road incidents* consistently rank among the top ten causes of death worldwide, and even at fourth most common cause in the age group of 15 to 49 [7]. Hence, investing in systems that alleviate this problem is a natural step. At the same time, the deployment of IoT concepts on vehicles proves to be an especially challenging one. Outdoor scenarios and high mobility are notoriously challenging problems for communications. Additionally, designing applications for safety-relevant use cases means that they have to fulfill a high degree of reliability. Therefore, it is vital to have a good grasp of the essential aspects of vehicular communications.

1.1 Intelligent Transportation Systems

ITS base their concept of "intelligent" on being autonomous, as well as being connected via communications. Autonomous driving means that the vehicle can act on its own, without the driver intervening. The range of actions a vehicle can do autonomously is often grouped into the *degrees of automation*, which classify based on the question of "Who is acting?", "Who is checking?" and "Who is managing?" [8]. Low degree automation actions are for example parking assistants, which often only provide additional information to the driver, who is still the main executor. Intermediate systems are for example braking assistants, that act autonomously, but only in tandem with the driver, and only in specified scenarios. High automation degrees refer to vehicles driving autonomously, with or without mandatory driver assistance. All those concepts are fundamentally egoistic. They benefit the driver, but other traffic participants can only see indirect benefit from autonomous cars. The opposite is true for another component of ITS: connectedness.

Unconnected vehicles gather information based exclusively on onboard sensors. Hence, they are fundamentally limited in their sensing range to similar limits as humans are. Connecting vehicles via mobile communication systems allows sharing data beyond this sensing reach. This however means, that the vehicle providing information does not gain directly from this act, only the receiving vehicle collects new information. Connectedness is only a benefit for the *other* vehicles. The information gain for connected vehicles is thus proportional to the number of communication partners. Since vehicles are a technology with a very slow turnover, acceptance of communication capabilities in vehicles is generally slower than autonomous concepts. Nevertheless, acceptance has been picking up and communications will be an increasingly important part of ITS. The communication aspects of ITS are split into two concepts with very distinct design goals, restraints and philosophies. On the one hand, there is *safety relevant* communications, on the other hand there is *infotainment*. Infotainment encompasses communication about road conditions, traffic jams and weather changes, as well as streaming applications. These have in common that high latency of the communication link is not harmful and short disruptions will only be noticed as minor inconveniences. Especially the streaming applications do however expect high throughput links in order to sustain the required data rate. In contrast to this, safety relevant communications do not attempt to achieve high data rates. In fact, most safety-relevant communication schemes try to use as

Die approbierte gedruckte Originalversion dieser Dissertation ist an der TU Wien Bibliothek verfügbar.
The approved original version of this doctoral thesis is available in print at TU Wien Bibliothek.
TU Bibliothek Your knowledge hub WIEN

little of the channel's capacity as possible. This is done to ensure that *if* critical information has to be communicated, there is still free capacity available immediately. Safety-relevant communications however do have stringent latency constraints, and are vulnerable to short-term disruptions.

Ensuring that a communication system is resilient with respect to aspects such as throughput, latency and immediate packet error probability requires careful deployment tests. Such tests need to be repeatable, standardized, and cover a sufficient amount of use cases. Finally, the test cases need to be representative for the actual usage conditions. Only then, the communication reliability can be assessed. Defining physical deployment test conditions that cover all aspects of Vehicular Ad-Hoc Network (VANET) communications is however infeasible, since it would imply replicating scenarios with up to hundreds of vehicles. Additionally, these scenarios should encompass setups with near-collisions and collisions. Finally, the whole scenario has to be tested in a repeatable fashion. Thus, all-encompassing real-world tests are not implementable. Hence, the testing of the systems has been compartmentalized into partial tests. Physical communication performance is often analyzed in single link communications, where one transmitter and one receiver are present. This simple setup allows evaluation of diverse scenarios while allowing for repeatability. Such a setup gives deep insights in actual propagation phenomena, but it excludes the influence of communication networks at Medium Access Control (MAC) layer. As the setup with physical nodes does not scale to larger networks, other approaches are required.

Large networks of communicating vehicles on the other hand are usually tested in simulations. These simulations incorporate as many details on the inter-working of the network of communicating nodes as complexity allows. However, often abstractions are introduced that limit the representativeness with respect to the physical propagation phenomena. Hence, simulations often fail to capture these physical channel properties. However, as the aspects of networking effect and physical propagation phenomena influence each other, partial tests can't cover the whole picture.

The aim of this thesis is to approach this split from a different direction. Instead of choosing between physical layer abstractions or ignoring of networking effects, this thesis considers both aspects. Then, simplifications for both aspects are introduced that allow to keep the overall complexity low. In this way, I ensure that no aspects suffers from oversimplifications.

1.2 Vehicular Communication Schemes

Vehicular communication schemes are, due to the mobile nature of the communication nodes, necessarily wireless. Among the wireless communication schemes relevant for wireless communications, one can distinguish two dominant organization structures for the communication network, *cellular* and *ad-hoc*. Figure 1.1 demonstrates these two concepts. In a cellular network, an infrastructure consisting of base-stations and a centralized backend is deployed, where mobile nodes can join in a hierarchical manner. In such a cellular network,

Die approbierte gedruckte Originalversion dieser Dissertation ist an der TU Wien Bibliothek verfügbar.
The approved original version of this doctoral thesis is available in print at TU Wien Bibliothek.
TU Bibliothek Your knowledge hub WIEN

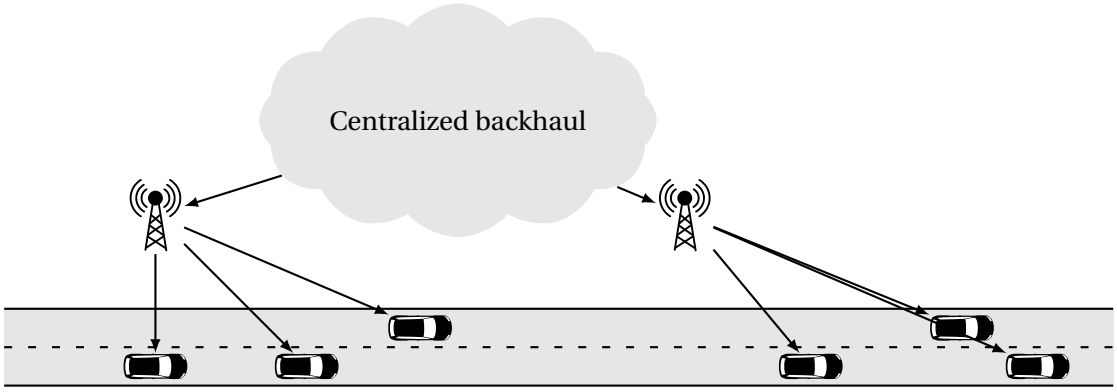

(a) Cellular vehicular network.

(b) Vehicular ad-hoc network.

Figure 1.1: Comparison between cellular connectivity and vehicular ad-hoc connectivity.

the infrastructure controls connection establishment and resource allocation. The advantage of this approach is the high efficiency that can be achieved when a centralized infrastructure is in charge of resource-allocation. The downside of such a system is the requirement for availability of such a central infrastructure, as well as a mandatory minimum complexity. On the other hand, if two communication nodes establish connections directly without a governing authority, this approach is called *ad-hoc* communication. The advantage of ad-hoc communication is that no presence of infrastructure is required to make it work, and thus presence of equipped vehicles suffices to enable communication anywhere. This also means that no unnecessary intermediate steps are taken in the communication path. The downside of an ad-hoc approach is the difficulty of resource allocation if a large amount of vehicles wants to access resources due to the lack of authority. MAC is often greatly facilitated by a governing authority. Both modes of operation are defined in standards for Vehicle-to-Everything (V2X) communications and I present give a quick overview over these modes.

Cellular schemes for data communication are the preferred choice when overall communication efficiency is of the highest interest. This means that throughput can be maximized over all nodes, at the cost of requiring backend infrastructure. This is a good approach for any type of infotainment, which encompasses streaming music and video, as well as updated information of traffic conditions for route planning and similar aspects. The crucial component is that the driver does not rely on the information being available. A loss of connection is at worst an inconvenience. For this application several technologies have been applied and researched. For high-throughput streaming services, Long Term Evolution (LTE) is the first generation of model communications that is able to support the demand, both in terms of achievable throughput and the ability to work under high mobility conditions. Thus, LTE is the first generation to see a chance of widespread deployment in vehicles from the manu-

Die approbierte gedruckte Originalversion dieser Dissertation ist an der TU Wien Bibliothek verfügbar.
The approved original version of this doctoral thesis is available in print at TU Wien Bibliothek.
TU Bibliothek Your knowledge hub WIEN

facturer [9]. For lower throughput requirements, other systems are also used. For example, *Advanced Automatic Collision Notification* is a system that automatically reports incidents that is made to work with as wide an array of technologies as possible to ensure maximum coverage for the functionality. Austria, Germany and the Netherlands have deployed IEEE 802.11p infrastructure units along a corridor of highways to provide up-to-date traffic information [10].

Cellular approaches add a non-negligible latency that is to the system. For example, the latency of standard LTE in one use-case was measured to be between 20 and 70 ms for one direction [11]. This exceeds the allowed latency thresholds for safety relevant communications, for example as given by the EU project METIS (5 ms, [12]). Furthermore, the presence of the correct infrastructure is required for the communication. Thus, cellular schemes are not the best fit for safety-relevant information broadcast between neighboring vehicles. For this application, ad-hoc communication is preferred. The fifth generation of cellular network technology (5G) promises to allow cellular structures with low latency performance [13], as well as New Radio (NR) V2X solutions [14].

The IEEE defined a version of IEEE 802.11 in 2007 that was specifically designed for VANET communications, which was originally called 802.11p. It has since been included in the core standard, and the "p" was dropped. However, to increase readability, I will continue to use 802.11p to make clear I am referring to this mode of the standard. This was the first standard designed from the start with vehicular safety applications in mind. The standard works at 5.9 GHz and supports a bandwidth of 10 MHz. The core pillars of the standard are handshake-less ad-hoc broadcast communications, low latency and ease of implementation to facilitate adaption. It is worth to point out that 802.11p only defines Physical Layer (PHY) and MAC layer, leaving the other aspects to be implemented by other standards. The EU has opted here for European Telecommunications Standards Institute (ETSI) ITS at 5.9 GHz (ITS-G5), while the USA uses Wireless Access in Vehicular Environments (WAVE). The standards are however extremely similar in many implementation aspects. LTE on the other hand added principal functionalities for Device-to-Device (D2D) communications in Release 12 in 2015. Specific communication modes that allow safety-relevant V2V communications were added in Release 14 via Mode 4 ofD2D communications [15]. This operation mode is commonly referred to as LTE-V. Due to the quick development cycles of mobile communication standards and the long deployment times of vehicles, there is currently a strong debate about the optimal choice, and coexistence and cooperation of these standards is a likely outcome to enhance communication capabilities. This approach has been favored as base concept for vehicular safety in Europe [16]. The IEEE is currently working on an update scaling to Millimeter Wave (mmWave) and tackling the shortcomings of 802.11p under the name 802.11bd [14]. I contrast to 5G New Radio, this approach strives for backwards compatibility with 802.11p to ensure that the old devices remain usable.

This basestation-less approach allows to achieve the stringent low latency requirements, but only in simplified transmission modes (no multi-hop, no re-transmissions). Instead, assessing such networks reduces to the question of how likely a packet is received successfully on the

Die approbierte gedruckte Originalversion dieser Dissertation ist an der TU Wien Bibliothek verfügbar.
The approved original version of this doctoral thesis is available in print at TU Wien Bibliothek.
TU Bibliothek Your knowledge hub WIEN

first attempt. To answer this question, all contributing factors have to be addressed. How does the current communication channel look like? How does the current communication channel interact with the chosen protocol? How does the presence of other transmitting nodes influence the performance? And finally, what are the dominating factors that determine the success rate in a given situation? In the next section, I present an overview over IEEE 802.11p in order to identify the relevant aspects of these questions.

1.3 IEEE 802.11p System Overview

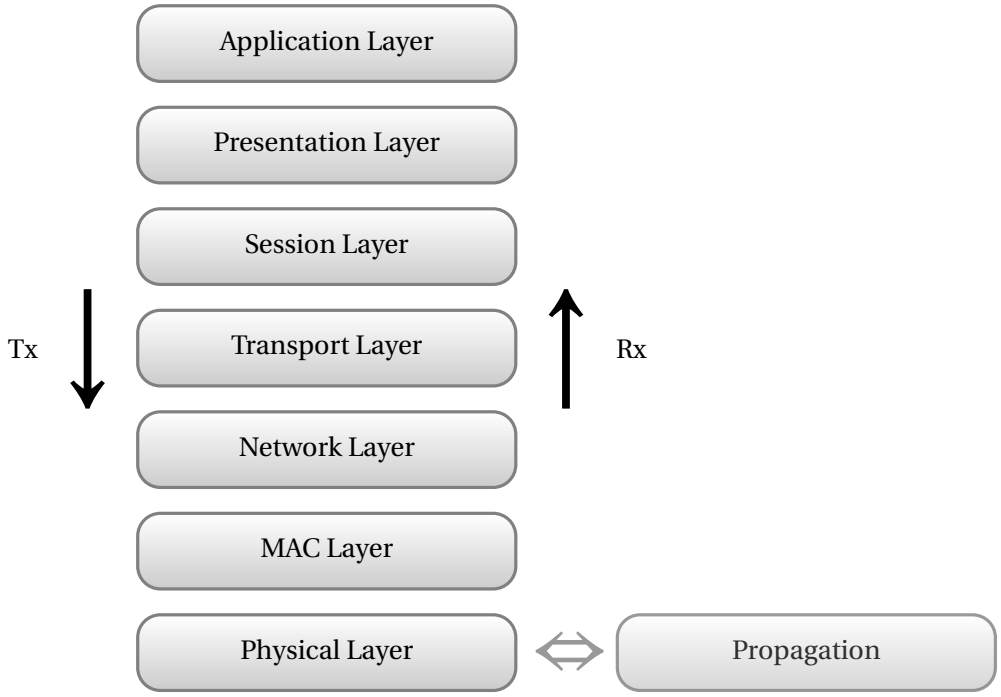

Figure 1.2: The OSI Layer model. A transmission (Tx) passes through the layers from top to bottom before being transmitted over the channel. Then, the transmission is received at the physical layer again, and passes upwards through the layers at the receiver (Rx).

IEEE 802.11p communications follows the layered approach that is described by the ISO Open Systems Interconnection (OSI) model as depicted in Fig. 1.2. The focus of this thesis is performance and reliability of the network for safety relevant communications. Performance and reliability aspects are mostly defined by the protocols and parameters defined at layer 1 and 2. The layers 3 – 7 on the other hand standardize the type of data that flows over the connection. This is reflected in the fact that IEEE 802.11p only defines layers 1 and 2. The higher layers are defined by complementary standards WAVE and ETSI ITS-G5. Thus, I concentrate the analysis on the bottom layers and use simple example use cases for the higher layers. IEEE 802.11p has been created by taking the IEEE 802.11n standard, and halving the baseband sampling rate. The system operates at 5.9 GHz, which is now reserved in many countries for safety-relevant V2X communications. In the following sections, I will give an

Die approbierte gedruckte Originalversion dieser Dissertation ist an der TU Wien Bibliothek verfügbar.
The approved original version of this doctoral thesis is available in print at TU Wien Bibliothek.
TU Bibliothek Your knowledge hub WIEN

overview over the key properties of IEEE 802.11p, and the approaches at capturing the PHY and MAC performance of the system. The following will give a short overview of the key aspects of this standard, especially the weaknesses that may lead to decreased performances.

1.3.1 The Physical Layer

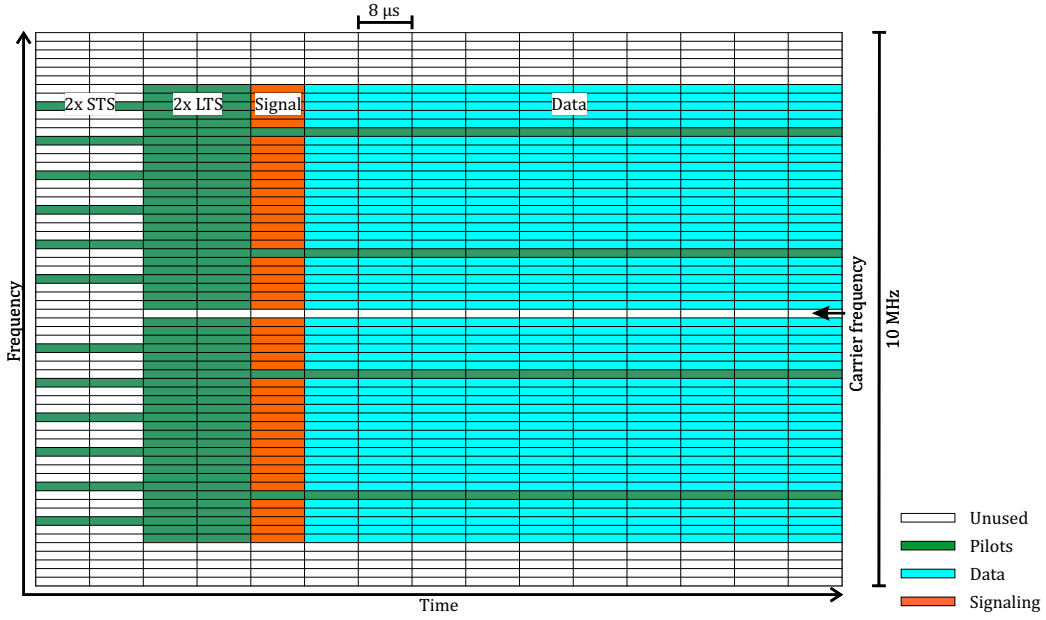

Figure 1.3: PHY structure of an IEEE 802.11p frame.

The PHY frame structure of IEEE 802.11p is depicted in Fig. 1.3. IEEE 802.11p uses a 64 subcarrier Orthogonal Frequency-Division Multiplexing (OFDM) system, with the subcarriers depicted on the vertical axes. The total bandwidth is 10 MHz, at a center frequency near 5.9 GHz. 25 % of the OFDM signal is prefixed in the Cyclic Prefix (CP), resulting in 8 μs symbol durations [17, 18]. The PHY frame starts with 2 OFDM symbols for time-frequency synchronization (so called Short Training Sequences (STSs)) and 2 OFDM symbols for channel estimation and equalization (so called Long Training Sequences (LTSs)). These ensure high quality channel synchronization and estimation at the beginning of a frame. For the remainder of the frame, IEEE 802.11p uses 4 tracking pilots at fixed subcarrier indices. Eleven subcarriers are left empty, which are split between six at the top and five bottom of the frequency assignment to produce a total guard band of 1.72 MHz. Independent of the length of a packet, STSs and LTSs are only placed at the beginning of a frame.

Die approbierte gedruckte Originalversion dieser Dissertation ist an der TU Wien Bibliothek verfügbar.
The approved original version of this doctoral thesis is available in print at TU Wien Bibliothek.
TU Bibliothek Your knowledge hub WIEN

Table 1.1 shows the Modulation and Coding Schemes (MCSs) that are used in IEEE 802.11p. The system uses a convolutional code with code rates $R \in \{1/2, 3/4\}$ and constellations of BPSK, QPSK, 16-QAM and 64-QAM are used. MCS-2 (QPSK, 1/2) is defined as default choice. The table also illustrates the total transmission durations for 100 and 200 byte beacon transmissions. Given the multi-layered structure of the communication systems, the aspects have to

Mode	MCS	Data rate	Sensitivity	Minimum SINR	Duration of 100 B packet	Duration of 200 B packet
0	BPSK, 1/2	3 Mbps	−85 dBm	10 dB	320 μs	584 μs
1	BPSK, 3/4	4.5 Mbps	−84 dBm	11 dB	224 μs	408 μs
2	QPSK, 1/2	6 Mbps	−82 dBm	13 dB	184 μs	312 μs
3	QPSK, 3/4	9 Mbps	−80 dBm	15 dB	136 μs	224 μs
4	16-QAM, 1/2	12 Mbps	−77 dBm	18 dB	112 μs	176 μs
5	16-QAM, 3/4	18 Mbps	−73 dBm	22 dB	88 μs	136 μs
6	64-QAM, 1/2	24 Mbps	−69 dBm	26 dB	80 μs	112 μs
7	64-QAM, 3/4	27 Mbps	−68 dBm	27 dB	72 μs	104 μs

Table 1.1: Allowed MCSs, along with the required channel quality and packet durations. [19]

be identified that have strong impact on the packet error performance. Specifically, I have to define which aspects are important in this analysis. The two basic channel effects that are expected are time dispersion due to multipath propagation with different path delays and time selectivity due to the movement of transmitter, receiver and scatterers.

Time Dispersion of the signal results in frequency selectivity and has two major impacts on the signal that cause performance degradation. The first one is Inter-Symbol-Interference (ISI) caused by one packet transmission echoing into the next transmission due to excess channel delay. This effect is mitigated by the CP, under the condition that the CP duration is at least as long as the excess channel delay. IEEE 802.11p's CP duration is 1.6 μs, which translates to a wave traveling an excess distance of $\approx$ 480 m at the speed of light. Considering that these 480 meters are calculated in excess of the direct path length, the effective travel distance for these late multipaths would be more than this distance and will be lost below the receiver sensitivity. The second effect of time dispersion is imperfect channel estimation and noise enhancement due to frequency selectivity. Frequency selectivity leads to subcarriers with low subband Signal-to-Noise Ratio (SNR) and, makes the channel harder to estimate correctly. Furthermore, updating the channel estimates can become an issue. Specifically, considering that IEEE 802.11p uses only four pilots after the channel estimation preamble. Given that the coherence bandwidth, or bandwidth in which I can assume the frequency response to be approximately flat, can be approximated as (c.f. [20])

$$B_{\text{coh}} \approx \sqrt{\frac{9}{16\pi}} \frac{1}{\tau_D}, \tag{1.1}$$

TU Bibliothek Your knowledge hub WIEN
Die approbierte gedruckte Originalversion dieser Dissertation ist an der TU Wien Bibliothek verfügbar.
The approved original version of this doctoral thesis is available in print at TU Wien Bibliothek.

with τ_D being the delay spread. For measured delay spreads of up to 1 μs, which were measured in [21], this relates to coherence bandwidths as low as 420 kHz. Thus, the pilots are not sufficient to estimate the channel if the estimation preamble is not sufficient.

Time Selectivity results in frequency dispersion, which again leads to two major impacts on the transmission quality. If the frequency dispersion is large enough to destroy orthogonality between subcarriers, Inter-Carrier Interference (ICI) occurs. This happens if the largest occurring Doppler shifts are noticeable fractions of the subcarrier spacing. As the subcarrier spacing of IEEE 802.11p is 156.25 kHz, the system is able to tolerate strong Doppler shifts. Figure 1.4 demonstrates the worst-case SIR that occurs as a result of ICI as a function of the maximum relative speed given a Jake's spectrum. Thus, even for the highest relative speeds occurring

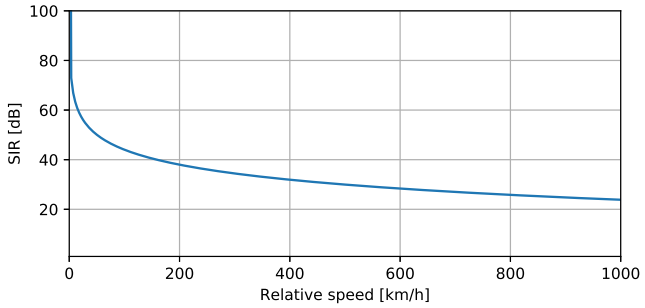

Figure 1.4: Worst case Signal-to-Interference Ratio (SIR) due to ICI.

between vehicles, the ICI will only have very limited impact. The second influence of time selectivity is that the channel changes over time. Due to the OFDM frame structure of IEEE 802.11p, a full pilot-based channel estimation is only possible at the beginning of the frame and subsequently channel changes can only be tracked via the four pilots, unless complex iterative decision feedback schemes are used. This is irrelevant if transmitted packets are shorter than the channel coherence time, which is approximated in [20] as

$$\tau_{\text{coh}} \approx \sqrt{\frac{9}{16\pi}} \frac{1}{f_D}, \tag{1.2}$$

with f_D being the maximal occurring Doppler bandwidth. For Doppler bandwidths of up to 2000 Hz, this coherence time can be as low as $\tau_{\text{coh}} \approx 100$ to 200 μs. This is far shorter than the length of IEEE 802.11p frames of more than 100 Byte with MCS 2. Therefore, the main focus of this thesis with respect to the channel lies in the question of how fast the channel becomes outdated, and how this is made worse by highly frequency selective channels.

The chosen MCS and the packet sizes then dictate how strong those influences can be, and thus what reliability is achievable.

Die approbierte gedruckte Originalversion dieser Dissertation ist an der TU Wien Bibliothek verfügbar.
The approved original version of this doctoral thesis is available in print at TU Wien Bibliothek.
TU Bibliothek Your knowledge hub WIEN

1.3.2 The MAC Layer

I consider the Cooperative Awareness Message (CAM) beacon from the ITS-G5 standard [**?**]. The CAM is a periodically transmitted *hello* message without response or acknowledgments. The CAM is a good choice as it is expected to make up for the bulk of the transmitted messages. Furthermore, other messages like the Decentralized Environmental Notification Message (DENM), are all broadcast type messages of varying length. These messages all have in common that retransmissions are not considered an option, since the latency may make them too outdated to be relevant. Thus, as test cases I limit myself single shot broadcast packets of varying sizes (≈ 100 to 500 bytes), without the possibility of retransmission. As baseline, the beacon frequency of the CAM message is used, which is defined (unless congestion is encountered) as $10\,s^{-1}$ [22]. Both ITS-G5 and WAVE allocate seven 10 MHz bands between 5.855 and 5.925 GHz (see Fig. 1.5), with one Control Channel (CCH) and six service channels ([23, 24]). ETSI ITS-G5 assigns three of the seven channels for traffic safety applications (ITS-G5A) and IEEE WAVE has a similar assignment. Within one channel Enhanced Distributed Channel Access (EDCA) is used as channel access scheme, which is based on Carrier Sense Multiple Access with Collision Avoidance (CSMA/CA), but distinguishes quality of service that needs to be achieved. It is a fully decentralized random access scheme. Due to the ad-hoc

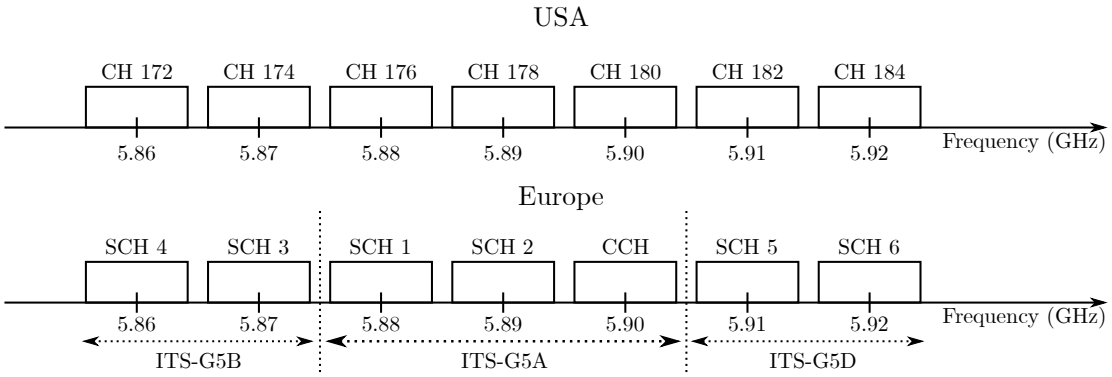

Figure 1.5: Frequency allocations for IEEE 802.11p in the WAVE and ETSI ITS-G5 standards. ETSI has defined blocks of ITS-G5A to ITS-G5D, where ITS-G5C lies outside the 5.9 GHz bands at 5.4 to 5.7 GHz [23].

nature, interference occurs as a result of simultaneous transmissions either due to timing issues (2 nodes switch from receiving to transmitting simultaneously), or the *hidden node problem* [25]. Here, two nodes that are not within communication range of each other, but are within range of a third node, may transmit simultaneously and interfere at the third node (see Fig. 1.6). The focus on safety and low latency means that the standard transmitted packets are broadcast messages that do not use Acknowledgements (ACKs) and are not retransmitted. Thus, interference of hidden nodes is the main concern of the MAC layer.

Die approbierte gedruckte Originalversion dieser Dissertation ist an der TU Wien Bibliothek verfügbar.
The approved original version of this doctoral thesis is available in print at TU Wien Bibliothek.
TU Bibliothek Your knowledge hub WIEN

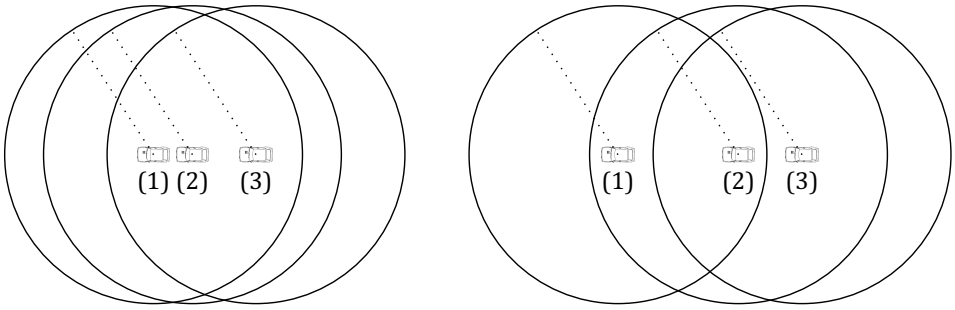

a) No hidden nodes. b) Hidden nodes exist.

Figure 1.6: Illustration of the hidden node problem. In a), all nodes are within communication range of each other. However, in b), nodes (1) and (3) are not able to sense each other. They are *hidden* with respect to each other, and may interfere.

1.4 Current State of the Research

The vehicular channel has been analyzed and studied diligently, both in conventional frequencies [21, 26–31] and the millimeter WAVE range [32, 33]. However, these works usually work to reproduce the channel with the maximum accuracy [34–37]. Few works have focused on parsimonious channel representations. Notable examples are [38, 39], where discrete prolate spheroidal sequences are used to emulate the vehicular channel in hardware. Conversely, the packet error performance has also been studied well. However, there exists a strong split in the research. In-depth packet loss analysis that includes the influence of the underlying communication channel usually only considers a single link. This includes measurement based analysis [40], as well as analytical work [41]. Protocol analysis with respect to hidden nodes and channel access on the other hand is often done in simulations that consider the full communication stack and movement models, but do not consider in-depth channel influences [15, 42–45]. They may focus on the channel access scheme [46, 47], or the influence of the vehicular distribution [25]. These results are highly valuable, but in terms of total performance provide a best case scenario. Few research works have considered the combination of link level and system level. Real world tests have often result to specific, small scenarios [19].

1.5 Contribution of this Thesis

In this thesis, I present a general approach for identifying key influences on the vehicular communication performance. I furthermore provide a modeling approach that incorporates these influences for accurate performance estimation while avoiding over-complicating the model. The first main contribution is a framework of finding sparse channel representations from channel measurements. I apply the Complex Least Absolute Shrinkage and Selection Operator (c-LASSO) to ensure sparsity [48] and the Akaike Information Criterion (AIC) to

Die approbierte gedruckte Originalversion dieser Dissertation ist an der TU Wien Bibliothek verfügbar.
The approved original version of this doctoral thesis is available in print at TU Wien Bibliothek.
TU Bibliothek Your knowledge hub WIEN

avoid overfitting [49]. The work has been published in [50], with supporting results published in [51–54].

In the second main contribution, I emulate the resulting sparse fits in hardware and estimate packet error performance for the IEEE 802.11p scheme via hardware transmission over emulated channels. This is done by connecting physical IEEE 802.11p transceivers to the physical channel. I first consider the single link analysis, which is published in [55]. Then, I extend the work to modeling a network of nodes. Here, I show that for the given scenario of a highly dense traffic jam, the communication network properties are retained while reducing its complexity. A small number of hardware nodes (transceivers and channel emulators) is sufficient to estimate the achievable performance considering both the network and the emulator. This was published in [56]. Supplementary results have been published in [57–59].

Finally, if only a high level description is required, I tackle the problem of packet probability modeling based on measured packet success events. The Gilbert-Elliott model is used to capture the effects of error bursts on the channel. This is published in [60]. Then, the information bottleneck theory is used to reduce the resulting model complexity [61] and a stochastic model for the interference is combined with the AIC to provide a low-complexity model that takes number of neighbors and SNR as input and gives Gilbert-Elliott parameters as output.

1.6 Notation

The probability of event $\mathscr{X}$ is written as $\Pr(\mathscr{X})$. Matrices $\boldsymbol{Z}$ and vectors $\boldsymbol{z}$ are denoted by bold letters. Entries of matrices or vectors are indexed via square brackets. If the indexed result is a scalar, it is not written bold anymore, while in case of partial indexing, the result is still boldface to indicate the matrix-nature. E.g. if $\boldsymbol{Z}$ is two-dimensional, $Z[1,2]$ is a scalar, while $\boldsymbol{Z}[1]$ is a vector consisting of the first row of $\boldsymbol{Z}$. Sometimes, in the interest of compactness, this will be written as subscript $Z_{0,1}$, but this usage will be highlighted. Matrix or vector dimensions are indicated via superscripts, for example, $\boldsymbol{z}^{1\times 7}$, whenever necessary. The all zeros vector (matrix) is expressed by $\mathbf{0}$, the all ones vector (matrix) is expressed by $\mathbf{1}$ and the identity matrix is expressed by $\boldsymbol{I}$. The Euclidean norm is symbolized by $\|\cdot\|_2$, the Manhattan norm by $\|\cdot\|_1$, accordingly. The dagger $(\cdot)^\dagger$ is used for pseudo inverses, $(\cdot)^{-1}$ is used for matrix inverses, $(\cdot)^{\mathrm{T}}$ is used for transposition and $(\cdot)^{\mathrm{H}}$ is used for conjugate transposition. Kronecker and Hadamard (element-wise) matrix products are denoted by $\otimes$ and $\odot$, respectively. $\mathrm{Diag}(\cdot)$ is a function that takes a vector and creates a diagonal matrix with the vector as main diagonal. Finally, $\mathrm{peak}(\cdot,k)$ is a function that returns the magnitude of the kth largest local maximum of the first argument. The ceiling operator is donated by $\lceil\cdot\rceil$.

In general, the communication channel is described, among other descriptions, by a time-variant frequency selective transfer function $h(f,t)$. In case I consider a discrete-time system, I replace the braces by square brackets, resulting in $h[t,f]$. Note that in this case, t and f are indices instead of physical quantities. They relate to the physical quantities via the sampling frequency f_s and arbitrary offsets f_0 and t_0 as

Die approbierte gedruckte Originalversion dieser Dissertation ist an der TU Wien Bibliothek verfügbar.
The approved original version of this doctoral thesis is available in print at TU Wien Bibliothek.
TU Bibliothek Your knowledge hub WIEN

$$f_{\text{discrete}} = \frac{f_{\text{continuous}} - f_0}{f_s}\,, \tag{1.3}$$

$$t_{\text{discrete}} = (t_{\text{continuous}} - t_0)\, f_s\,. \tag{1.4}$$

1.7 Structure of the Thesis

Chapter 2 explains in-detail the sparse channel estimation algorithm provided. I present a general framework and analyze the algorithm both with 2 sets of measurement data, synthetic data and different configurations. The results show that the vehicular channel is modeled sufficiently well with a small set of parameters given a well-chosen basis.

Based on the results from Chapter 2, Chapter 3 estimates the packet transmission performance. The chapter first provides single link performance analysis that is obtained by connecting transceivers to a hardware channel emulator. Then, I extend the approach to a network of nodes. An algorithm is presented that allows to reduce the complexity and calculate the performance with just a few devices.

Chapter 4 abstracts the system into a purely stochastic model. First, a Gilbert-Elliott based model is presented that captures the single link and is able to capture error bursts as well as average behavior. Then, interference is introduced and parsimonious model parameters are calculated.

Finally, in Chapter 5, I present my overall conclusions from this thesis.

Die approbierte gedruckte Originalversion dieser Dissertation ist an der TU Wien Bibliothek verfügbar.
The approved original version of this doctoral thesis is available in print at TU Wien Bibliothek.
TU Bibliothek Your knowledge hub WIEN

Die approbierte gedruckte Originalversion dieser Dissertation ist an der TU Wien Bibliothek verfügbar.
The approved original version of this doctoral thesis is available in print at TU Wien Bibliothek.

2 Reduced Complexity Channel Modeling

The task of this chapter is to find low complexity — high fidelity descriptions of the vehicular communication channel. One of my goals for the remainder of the thesis is to implement a channel model with feasible complexity on a hardware channel emulator. This emulator has a defined architecture based on a tapped delay line with limited complexity. Therefore, one goal of this chapter is to find a channel modeling approach that reproduces the underlying channel on that architecture adequately. However, I choose an approach that is more general. I introduce an optimization approach that finds a sparse description in any basis of choice, not just the tapped delay line. I also demonstrate the results with various bases for comparison. The optimization algorithm is based on the c-LASSO [48]. The resulting fits are evaluated for a model order determined by the AIC, which penalizes overfitting of noisy data. The results are evaluated based on mmWave measurements. These show that the mmWave measurements are naturally sparse if the correct basis is chosen. The same analysis is also presented for a measurement set at 5.6 GHz in Appendix A.

This chapter is based on [50]. Additional results come from [51–53, 62].

2.1 Vehicular Channel Modeling

In this section, I describe how to assess the influence of the channel on the packet transmission. Figure 2.1 shows the general concept of the process. State **1)** illustrates a possible momentary channel between two vehicles. Given a transmit sequence $x(t)$, the output sequence $y(t)$ is a formed by a noise-free doubly selective channel $g(\tau, t)$ as given by

$$y(t) = \int_{-\infty}^{\infty} x(t-\tau) g(\tau, t) \mathrm{d}\tau. \tag{2.1}$$

The final goal here is to evaluate this equation, or at least an approximate, in hardware, as shown in state **3)** of Fig. 2.1. To achieve this, $g(\tau, t)$ needs to be known, and provide an approximation of Eq. (2.1) that can be realized in a hardware setup. These aspects are discussed

Die approbierte gedruckte Originalversion dieser Dissertation ist an der TU Wien Bibliothek verfügbar.
The approved original version of this doctoral thesis is available in print at TU Wien Bibliothek.
TU Bibliothek Your knowledge hub WIEN

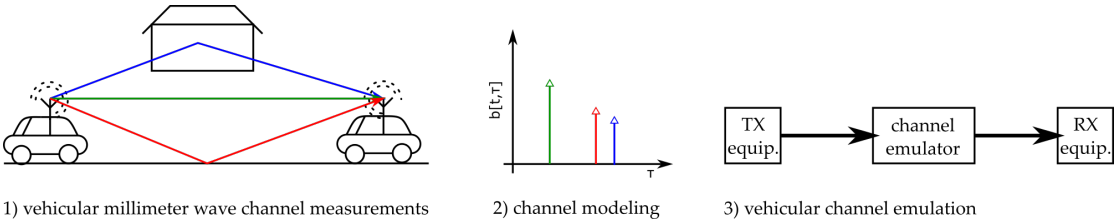

1) vehicular millimeter wave channel measurements 2) channel modeling 3) vehicular channel emulation

Figure 2.1: Necessary stages for channel emulation. **1)** depicts the encountered Multipath Components (MPCs) of a V2V transmission, **2)** shows a simplified channel impulse response representation of **1)**, and **3)** shows how a physical device applies the model from **2)** to a signal going from Transmitter (TX) to Receiver (TX).

in the following sections. Considering Fig. 2.1, the first goal is to find a channel description $g(\tau, t)$ that is representative of a *vehicular channel*. In the figure, the multipath-components are shown in stage **1)** are mapped to a tapped delay line in stage **2)**. There are different approaches to doing this with different merits and drawbacks. Their main distinguishing feature is the trade-off between how strongly they are steeped in real-world scenarios and how many stochastic assumptions they introduce. The most straightforward way of obtaining $g(\tau, t)$ is through a channel sounding campaign. One step of abstraction further, there are *geometry-based channel models*. These are not directly linked to measurements. Instead, they combine actual geometric scenarios (such as a car driving around a corner), with stochastic modeling approaches to obtain the statistical channel description for such a scenario. Finally, channel descriptions based on *stochastic models* operate on a high level of abstraction and the impulse response is typically the result of a purely stochastic process. In the following sections, I briefly delineate the benefits and drawbacks of the different approaches.

Measurement Playback Here the hardware attempts at replaying previously recorded channel sounder data as faithfully as possible [55]. In this case, the importance of stage **2)** is reduced as much as possible, ideally making it a completely transparent adaption from **1)** to **3)**. The advantage of this approach is that no statistical model assumptions have to be introduced, and uncertainty only stems from the measurements themselves. The downside of the approach on the other hand is that the measured channel is not inherently representative of a larger scenario. Furthermore, limitations when implementing the playback have to be accounted for. Thus, only an approximation of the measured channel can actually be played back, and the resulting SNR of the emulation is limited by the measurement quality.

Geometry-Based Channel Emulation In this modeling approach, a vehicular channel is generated from geometric data, employing tools like Geometry-based Stochastic Channel Models (GSCMs) [38, 39]. These models take the general approach of building on transmitter and receiver positions. This directly results in the dominant transmission paths. Then, scatterer clouds are generated from the geometry according to stochastic models [63]. They can be viewed as greatly simplified raytracing with added stochastic models. Alternatively,

Die approbierte gedruckte Originalversion dieser Dissertation ist an der TU Wien Bibliothek verfügbar.
The approved original version of this doctoral thesis is available in print at TU Wien Bibliothek.
TU Bibliothek Your knowledge hub WIEN

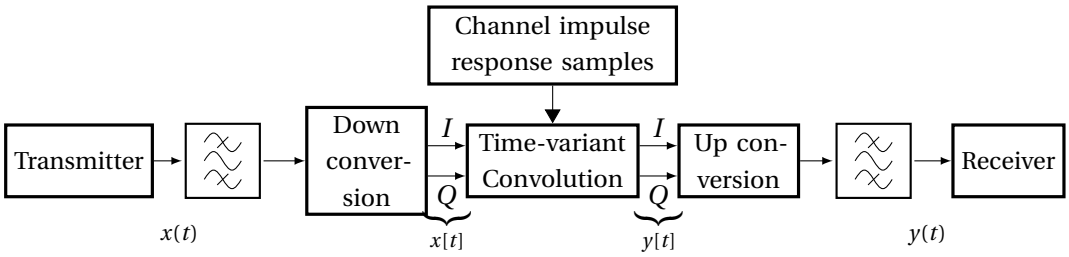

Figure 2.2: System view of the emulator.

raytracing can be applied directly [37, 64]. While these types have to make model assumptions to arrive at emulation, the benefit of this approach is that it can be executed online. As the geometry can be simulated live, an implementation that is sufficiently fast can translate the geometry to emulation at runtime, and thus provide reactive channel emulations that allow virtual drive tests. Furthermore, due to the inclusion of stochastic models, it is easier to define comparable scenarios, and thus the resulting models can be tuned between being specific and general, depending on whether the geometry or the stochastic components are dominating. Here, stage **1)** and **2)** are equally important and have to be modeled in conjunction.

Model-Based Channel Emulation Finally, this is the conventionally most popular method. Model based channel estimation is based on stochastic channel models (e.g. [65]). Examples of such models are the Cooperation in Science and Technology (COST) model [66] or the WINNER model [67]. These models are often defined in standards as standardized reference channel models for a given standard. This lends them especially well to benchmarking and comparison of applications and implementations. If done correctly, such models may be representative for a whole class of scenarios, making the emulation results highly interesting. Furthermore, due to the stochastic simplifications, these models tend to be of low complexity to enable hardware implementation. The downside of such model-based emulation, is that the emulation quality is completely dependent on the model quality. Thus, the model is difficult to adapt to more specific scenarios. For example a typical urban channel model is usually not representative of turning a corner. Here the emulator is completely defined at stage **2)**, and stage **1)** channel measurements are only taken into account as validation and for tuning purposes, not as a model driving influence.

2.2 Emulator Implementation

A channel emulator's goal is to replicate the output $y(t)$ according to Eq. (2.1) as close as possible on an input sequence $x(t)$ with a given channel impulse response $g(\tau, t)$, or its transfer function $h(f, t)$. The first simplification that is introduced is that the emulator works in the digital domain in the complex baseband. Thus, I consider the sampled, down-converted

Die approbierte gedruckte Originalversion dieser Dissertation ist an der TU Wien Bibliothek verfügbar.
The approved original version of this doctoral thesis is available in print at TU Wien Bibliothek.
TU Bibliothek Your knowledge hub WIEN

signals $x[t]$, $y[t]$ and $g[\tau,t]$ [1]. The correspondence is clarified in the system view in Fig. 2.2. Thus, the emulator's task is to execute

$$y[t] = \sum_{\tau=-\infty}^{\infty} x[t-\tau]g[\tau,t]. \tag{2.2}$$

I now introduce common assumptions. First, I assume the impulse response to be *causal*, that is

$$g[\tau,t] = 0 \quad \forall(t,\tau) \quad | \quad t \in \mathbb{Z} \wedge \tau \in \mathbb{Z}_-, \tag{2.3}$$

where $\mathbb{Z}$ denotes the whole numbers and $\mathbb{Z}_-$ the negative whole numbers. Furthermore, I introduce the assumption of an *approximately* finite impulse response. By this I mean that it can be assumed that the energy contained in a finite impulse response cut off at length D approximates the original potentially infinite impulse response sufficiently well

$$\left| \sum_{\tau=0}^{D-1} |g[\tau,t]|^2 - \sum_{\tau=0}^{\infty} |g[\tau,t]|^2 \right| < \epsilon, \tag{2.4}$$

with a sufficiently small ϵ. Theoretically, this criterion needs to be formulated in the continuous time domain. However, considering Fig. 2.2, I assume that the receiver's first two blocks are a sufficiently well working bandpass filter and down-converter. If that is the case, the up-and-down-conversion cancel each other, and the receiver directly observes the complex baseband channel Eq. (2.2).

After these two assumptions, I write the sequence of impulse responses as $\boldsymbol{g}[t]$, which is a sequence of vectors $\boldsymbol{g} \in \mathbb{C}^D$ where the entries are delay taps. This relates to a snapshot of the transfer function $h[f,t]$, rewritten as sequence of vectors $\boldsymbol{h}[t]$, where the entries are the subcarrier weights. They relate through the Discrete Fourier Transform (DFT) matrix $\boldsymbol{F}$ via $\boldsymbol{h}[t] = \boldsymbol{F}\boldsymbol{g}[t]$. This leads to the vector notation of the convolution

$$y[t] = \boldsymbol{g}[t]^T \underbrace{\begin{bmatrix} x[t-D+1] \\ x[t-D+2] \\ \vdots \\ x[t] \end{bmatrix}}_{\mathbf{x}[t]}. \tag{2.5}$$

Here, I also introduce my notation for a transmit vector being equal to a snapshot of transmit sequence of length D.

Evaluating this equation requires D multiplications and $D-1$ additions, and is therefore in the linear complexity of $\mathcal{O}(D)$, with $\mathcal{O}$ being the Landau symbol, which describes the asymptotic behavior [68]. Finally, D elements of $g[\tau,t]$ need to be in memory for every sampling time. It

[1] Here I use the convention of reusing the continuous variables for their sampled representations according to Section 1.6.

Die approbierte gedruckte Originalversion dieser Dissertation ist an der TU Wien Bibliothek verfügbar.
The approved original version of this doctoral thesis is available in print at TU Wien Bibliothek.
TU Bibliothek Your knowledge hub WIEN

is obvious that the *order* of the model, at this time determined by the number of elements in the impulse response D, determines the minimum complexity of the system. The next goal is to find a model representation where this model order can be reduced. The channel sounding campaigns used in this thesis provide snapshot samples of the transfer function arguments on the transfer function.

The transfer function $\boldsymbol{h}[t]$ tends to be highly dense, that is, no entry is zero, or even close to zero. Hence, the model order when using the frequency response is D, which is equal to the number of resolved frequencies in the considered bandwidth $B = 1/T_0$. However, the vector $\boldsymbol{h}[t]$ can be represented via a general basis $\boldsymbol{A}$ and the corresponding basis expansion $\boldsymbol{b}[t]$ as

$$\boldsymbol{h}[t] = \boldsymbol{A}\boldsymbol{b}[t]. \tag{2.6}$$

Here $\boldsymbol{A}$ is of dimension $D \times B$ where B is the number of basis vectors considered. Given a good choice of the basis $\boldsymbol{A}$, the vector $\boldsymbol{b}[t]$ may have few dominant contributions, with the rest of the entries being close to zero. I call that approximately sparse. In such a scenario, a vector $\hat{\boldsymbol{b}}[t]$ is found that is K-sparse[2] and approximates the transfer function

$$\boldsymbol{h}[t] \approx \boldsymbol{A}\hat{\boldsymbol{b}}[t]. \tag{2.7}$$

Given such a basis, the convolution in (Eq. (2.5)) is rewritten as

$$y[t] \approx \hat{\boldsymbol{b}}[t]^T \boldsymbol{A}^T \boldsymbol{F}^* \boldsymbol{x}[t]. \tag{2.8}$$

Since the matrices $\boldsymbol{A}$ and $\boldsymbol{F}$ are constant, the amount of data to be streamed is reduced to the sparsity K of the vector $\hat{\boldsymbol{b}}[t]$. Furthermore, the computational complexity of evaluating the channels can be controlled by choosing $\boldsymbol{A}^T\boldsymbol{F}^*$ in a smart manner.

In the remaining chapter I consider two approaches. For the hardware benchmarking that I employ in the remaining thesis, I choose $\boldsymbol{A} = \boldsymbol{F}$. This has significant complexity implications. The architecture has a shift register that keeps D elements of the transmitted signal, and convolves them with a K-sparse impulse response $\boldsymbol{g}[t]$. By enforcing sparsity, I ensure that the computational complexity remains at $\mathcal{O}(K^2)$ operations, and $2K$ parameters have to be loaded for each sampling time (2 for the complex values and their positions in the array).

On the other hand, I keep the estimation process more general to allow also to find other solutions. In that case , from Eq. (2.8), one can directly estimate upper and lower bounds on the computational complexity for general channel emulators. I first introduce the *weighting*

[2] K-sparse means the vector has exactly K nonzero entries.

Die approbierte gedruckte Originalversion dieser Dissertation ist an der TU Wien Bibliothek verfügbar.
The approved original version of this doctoral thesis is available in print at TU Wien Bibliothek.
TU Bibliothek Your knowledge hub WIEN

matrix $\boldsymbol{W} = \boldsymbol{A}^T \boldsymbol{F}^*$ The equation when written out is given as

$$y = \sum_{\tau=0}^{K-1} \hat{b}[\tau] \sum_{q=0}^{D-1} W[\tau, q] x[q] \tag{2.9}$$

$$= \sum_{\tau=0}^{K-1} \sum_{q=0}^{D-1} \hat{b}[\tau] W[\tau, q] x[q] \tag{2.10}$$

This equation has an upper limit of $2KD$ multiplications, and $KD-1$ additions, resulting in a complexity of $\mathcal{O}(KD)$. However, if the matrix $\boldsymbol{W} = \boldsymbol{A}^T \boldsymbol{F}^*$ itself is sparse, the complexity can be reduced further, namely to the number of nonzero entries $\mathcal{O}(K_W)$ with

$$K_W = \sum_{\tau=0}^{K-1} \sum_{q=0}^{D-1} \mathcal{I}(W[\tau, q]), \tag{2.11}$$

with $\mathcal{I}(\cdot)$ being the indicator function that is 0 if the argument is 0 and 1 otherwise. In the extreme case, where $\boldsymbol{W}$ is a diagonal matrix, or more generally has only one nonzero entry per row, the complexity reduces to $\mathcal{O}(K)$.

2.3 Sparse Channel Models and Estimation

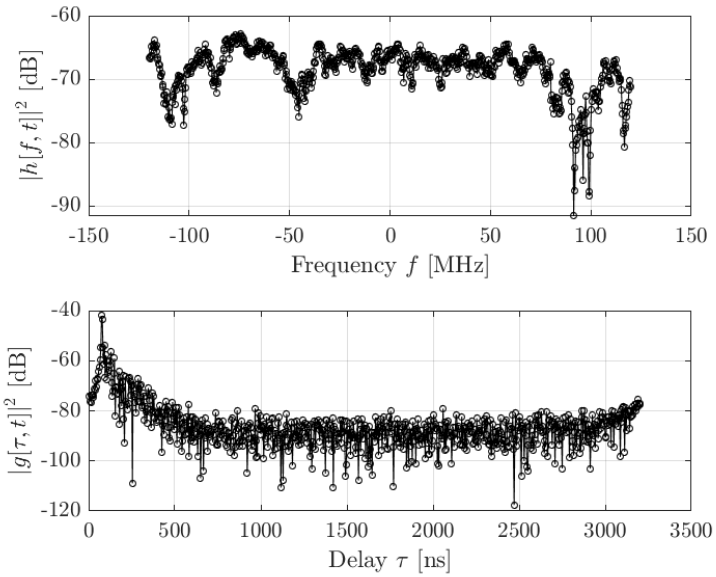

Figure 2.3: Magnitude realization of frequency response $\boldsymbol{h}$ and corresponding impulse response $\boldsymbol{g}$. The figure indicates the distribution of channel energy in different domains.

In the discrete-time domain, the transfer function which considers D frequency slots at time t is described by the vector-notation $\boldsymbol{h}[t] = [h[1,t], h[2,t], \ldots, h[D,t]]^T$, with $\boldsymbol{h}[t] \in \mathbb{C}^{N\times 1}$. The main interest now lies in alternative channel representations that provide sparse models. Since

Die approbierte gedruckte Originalversion dieser Dissertation ist an der TU Wien Bibliothek verfügbar.
The approved original version of this doctoral thesis is available in print at TU Wien Bibliothek.

sparsity refers to signals with a majority of 0-entries, it is worth looking at representations where many entries' magnitudes are already close to 0. For this indication of sparsity, the phases are not relevant in this thesis due to the 1-norm that I employ in the used algorithm. For example, Fig. 2.3 shows the transfer function as well as the impulse response. There one sees that the impulse response is naturally more sparse than the transfer function. In the following section, I consider multiple possible representations.

2.3.1 Channel Representations

Tapped Delay Line

The most frequently used representation besides the time-variant transfer function $h[f,t]$ is the time-variant impulse response $g[\tau,t]$, which depends on the time and the delays. Fig. 2.3 shows the impulse response and the transfer function of the same measurement snapshot. The impulse response compresses the energy in much less active taps than the transfer function. The channel can always be represented as a tapped delay line, but it is not always a sparse function.

The impulse response is **sparse** if one of the following two conditions holds.

1. Only a small number of distinctive MPCs exist.
2. If many MPCs exist, they are grouped in a small number of *clusters*. Within these clusters, all MPCs arrive within the same sampling period, resulting in only one resolvable tap.

If sparsity is assumed in the delay domain, the sparse expansion basis expansion can be identified as delay line, that is $\boldsymbol{b}[t] \stackrel{!}{=} \boldsymbol{g}[t]$. Then, channel impulse response is described as

$$b[t,\tau] = \sum_{m=1}^{M} b_m[t]\delta[\tau - \tau_m[t]] \,. \tag{2.12}$$

Here, $\delta[\cdot]$ is the time-discrete Dirac function, which is 1 at argument 0, and 0 otherwise. $b_m[t]$ and $\tau_m[t]$ are complex amplitude and delay of the mth tap respectively. Hence, this model is called the tapped delay line model [58]. This delay line can be written in vector notation as function of time $\boldsymbol{b}[t] \in \mathbb{C}^{N\times 1}$, and is related to $\boldsymbol{h}[t]$ via the DFT matrix $\boldsymbol{F}$

$$\boldsymbol{h}[t] = \boldsymbol{A}\boldsymbol{b}[t] = \boldsymbol{F}\boldsymbol{b}[t] \,. \tag{2.13}$$

In this case, I use the unitary, centered definition of the DFT matrix with elements defined as

$$A[n,k] = F[n,k] = \frac{1}{\sqrt{N}} \exp\left(-j\frac{2nk}{N}\left(n - \frac{N-1}{2}\right)\right) . \tag{2.14}$$

Die approbierte gedruckte Originalversion dieser Dissertation ist an der TU Wien Bibliothek verfügbar.
The approved original version of this doctoral thesis is available in print at TU Wien Bibliothek.
TU Bibliothek Your knowledge hub WIEN

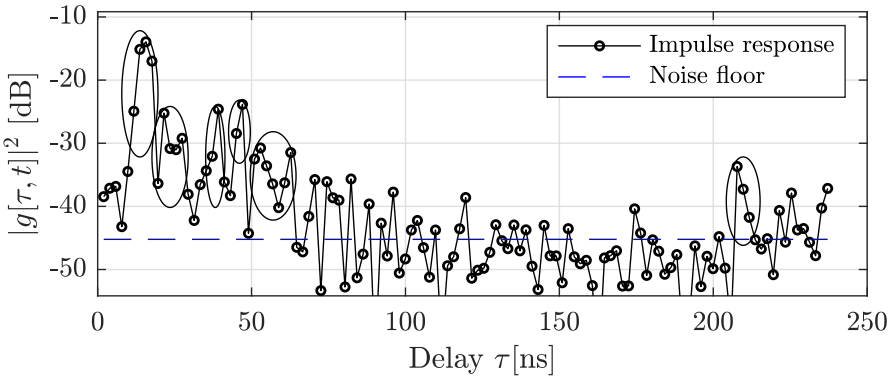

Figure 2.4: Example transfer function and impulse response snapshot from measurements. The strong components clearly arrive in clusters. Potential clusters are indicated with ellipses.

The reason for using the centered DFT is that channel sounders usually have the 0 subcarriers at the center in their measurements, which is directly captured by this matrix. I use the unitary description to ensure that Mean Squared Errors (MSEs) can be calculated in both time and frequency domain. For this basis, the input-output relation in Eq. (2.8) becomes

$$y[t] \approx \hat{\boldsymbol{b}}[t]^T \underbrace{\boldsymbol{F}^T \boldsymbol{F}^*}_{=\boldsymbol{I}_{N\times N}} \boldsymbol{x}[t] \tag{2.15}$$

In this case, the implementation complexity is exactly K multiplications and $K-1$ additions per timestep, where K is the sparseness of $\hat{\boldsymbol{b}}[t]$.

Clustered Delay Line

If MPCs arrive clustered, but the sampling period is too small, the tapped delay line representation is not sparse anymore. This happens in wide-band systems, such as typical mmWave systems. Then, an impulse response structure

$$g[\tau,t] = \sum_{k=1}^{K_0} \sum_{l=1}^{L_0} g_{k,l}[t]\delta[\tau - (T_k + \tau_{l,k})], \tag{2.16}$$

emerges. Here, K_0 is the number of clusters, T_k is the delay of the kth cluster, and $\tau_{l,k}$ is the excess delay of the lth tap within the kth cluster. The overall sparsity of the tapped delay line in this case equals $M = L_0 K_0$. Of course, the same basis expansion can be used as in Section 2.3.1. However, basis expansions may be found that exploit the cluster structure better. A realization of such a cluster response seen in measurements is shown in Fig. 2.4.

By projecting the transfer function on a smaller frequency subband, I reduce the delay resolution of the system. Then, the $\delta[\cdot]$ in Eq. (2.16) collapse onto one value again within one cluster.

Die approbierte gedruckte Originalversion dieser Dissertation ist an der TU Wien Bibliothek verfügbar.
The approved original version of this doctoral thesis is available in print at TU Wien Bibliothek.
TU Bibliothek Your knowledge hub WIEN

Thus, more MPCs will coincide on one tap, and the overall structure will be more sparse. I introduce the projection matrix $\boldsymbol{Q}_{\mathscr{S}}$, which is a diagonal matrix of the structure

$$Q_{i,i} = \begin{cases} 1, & i \in \mathscr{S} \\ 0, & \text{otherwise} \end{cases}, \tag{2.17}$$

with $\mathscr{S}$ being the block of considered subcarriers. Here, I impose the considered subcarriers to be adjacent, to achieve bandpass structure. Then, the delay line $\boldsymbol{b}_{\mathscr{S}}[t]$ which fulfills

$$\boldsymbol{Q}_{\mathscr{S}}\boldsymbol{h}[t] = \boldsymbol{Q}_{\mathscr{S}}\boldsymbol{F}\boldsymbol{b}_{\mathscr{S}}[t] \tag{2.18}$$

is more sparse for smaller sets of $\mathscr{S}$. Now the full bandwidth B is split into P orthogonal subbands of equal size

$$Q_{i,i} = \begin{cases} 1 & (p-1)\frac{D}{P} < i \leq p\frac{D}{P} \\ 0 & \text{otherwise} \end{cases}, \tag{2.19}$$

and introduce a separate basis expansion $\boldsymbol{b}_1[t], \boldsymbol{b}_2[t], \dots \boldsymbol{b}_P[t]$ for each subband $\sum_{p=1}^{P} \boldsymbol{Q}_p\boldsymbol{h}[t] = \sum_{p=1}^{P} \boldsymbol{Q}_p\boldsymbol{F}\boldsymbol{b}_p[t]$. From this, the concatenated vector $\boldsymbol{b}_{\text{subband}}$, as well as the concatenated projected DFT matrix $\boldsymbol{A}_{\text{subband}}$ is constructed. This results in a new basis expansion

$$\boldsymbol{b}_{\text{subband}} = [\boldsymbol{b}_1[t]^T, \boldsymbol{b}_2[t]^T, \dots \boldsymbol{b}_P[t]^T]^T, \tag{2.20}$$

$$\begin{aligned} \boldsymbol{A}_{\text{subband}} &= [\boldsymbol{Q}_1\boldsymbol{F}, \boldsymbol{Q}_2\boldsymbol{F}, \dots, \boldsymbol{Q}_P\boldsymbol{F}] \\ &= \left(\boldsymbol{I}^{P\times P} \otimes \boldsymbol{1}^{(D/P)\times D}\right) \odot \left(\boldsymbol{1}^{1\times P} \otimes \boldsymbol{F}\right), \end{aligned} \tag{2.21}$$

$$\boldsymbol{h}[t] = \boldsymbol{A}_{\text{subband}}\boldsymbol{b}_{\text{subband}}[t]\,. \tag{2.22}$$

For K_0 clusters, this has a total sparseness of $M = K_0 P$, however, as is shown later, this basis exploits the cluster structure well, and requires a smaller total model order M, than a straightforward tapped-delay line expansion. While K_0 remains the same, I demonstrate that P can be chosen significantly smaller than L_0 for the same estimation quality.

The resulting estimate is collapsed into a tapped delay line $\boldsymbol{b}_{\text{cluster}}$ via the Inverse DFT (IDFT)

$$\boldsymbol{b}_{\text{cluster}} = \left(\boldsymbol{F}^{D\times D}\right)^{-1} \boldsymbol{A}_{\text{subband}}^{D\times DP}\boldsymbol{b}_{\text{subband}}[t]\,. \tag{2.23}$$

In these circumstances, Eq. (2.8) becomes

$$y[t] \approx \hat{\boldsymbol{b}}[t]^T \underbrace{\boldsymbol{A}_{\text{subband}}^T\boldsymbol{F}^*}_{=\boldsymbol{W}}\boldsymbol{x}[t]. \tag{2.24}$$

Die approbierte gedruckte Originalversion dieser Dissertation ist an der TU Wien Bibliothek verfügbar.
The approved original version of this doctoral thesis is available in print at TU Wien Bibliothek.
TU Bibliothek Your knowledge hub WIEN

The structure of this weighting matrix for the inner product ins shown in Fig. 2.5. The figure was computed with 121 subcarriers. The leftmost column shows the magnitude of the entries for different values of P. $P = 1$ degenerates to the tapped delay line. The second column shows the magnitude squared of the entries of one row of $\boldsymbol{W}$. The third column shows the cumulative energy in the N strongest entries of that vector.

The results demonstrate the implications for hardware implementation. On $P = 1$,exactly 1 tap per are needed. When increasing the number of subbands, the number of nonzero elements in $\boldsymbol{W}$ increases. For $P = 2$, 5 multiplications and additions are needed per cluster to retain 95 % of the signal energy. By further increasing the number of subbands, $\boldsymbol{W}$ becomes densely populated. This means that online implementation of this convolution becomes gradually more and more complex. Thus, when implementing the clustered delay line in hardware, a trade-off is required between the number of subbands used, and the resulting computational complexity.

Die approbierte gedruckte Originalversion dieser Dissertation ist an der TU Wien Bibliothek verfügbar.
The approved original version of this doctoral thesis is available in print at TU Wien Bibliothek.

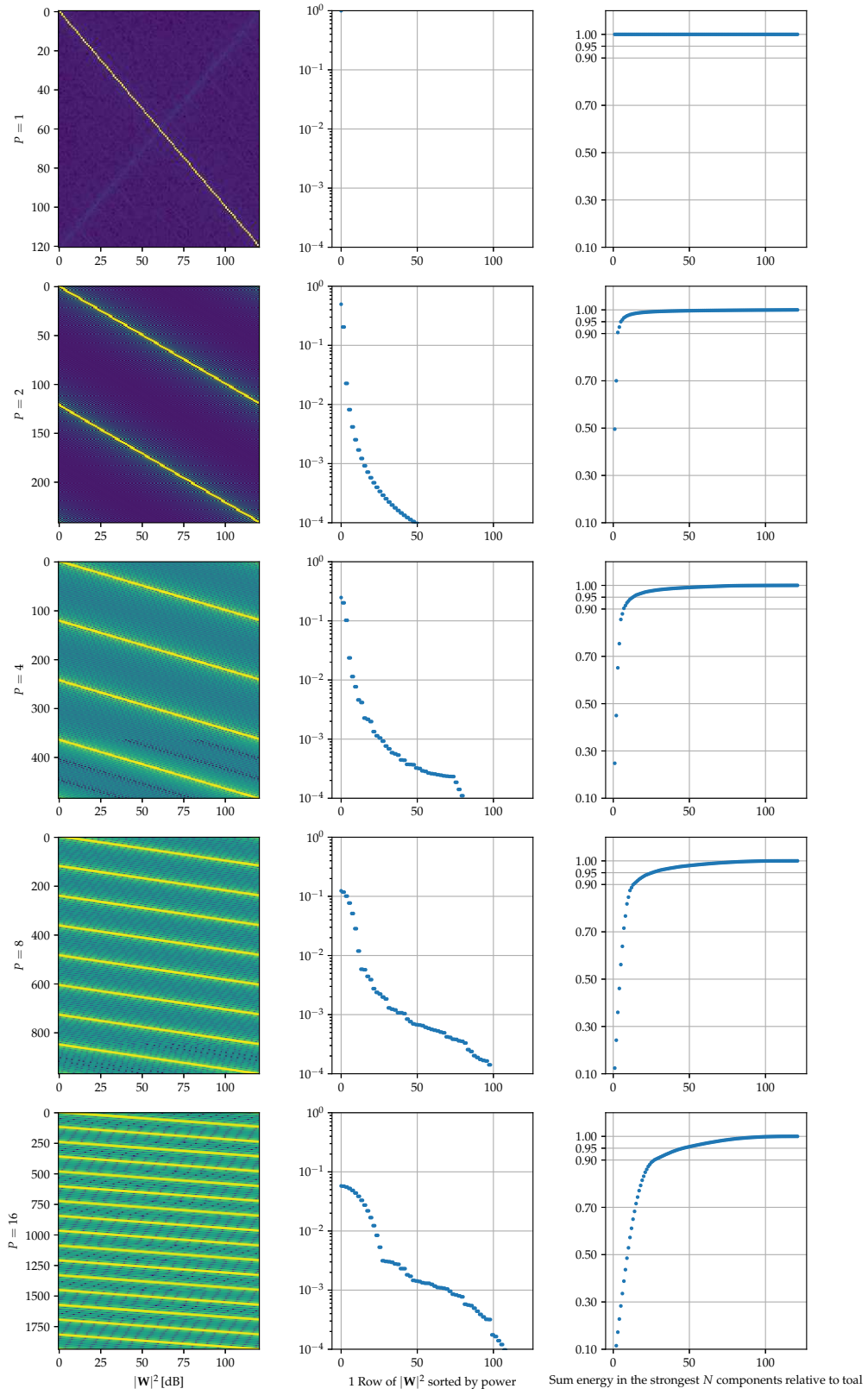

Figure 2.5: Analysis of the $\boldsymbol{W}$ weighting matrix that indicates the implementation complexity.

Die approbierte gedruckte Originalversion dieser Dissertation ist an der TU Wien Bibliothek verfügbar.
The approved original version of this doctoral thesis is available in print at TU Wien Bibliothek.
TU Bibliothek Your knowledge hub WIEN

Delay-Doppler Grid

This is a two-dimensional scheme. Instead of considering only frequency or time, I aggregate multiple timeslots in one time-frequency block. This block is then considered in the delay-Doppler domain. In general, the transformation from delay-Doppler domain to time-frequency domain is done by the Discrete Symplectic Fourier Transform (DSFT). The DSFT transforms the delay-Doppler dependent scattering function $S[\tau, \nu]$ to the time-frequency dependent transfer function $H[f, t]$ via [69]

$$H[f,t] = \frac{1}{\sqrt{DT}} \sum_{\tau=0}^{D-1} \sum_{\nu=0}^{T-1} S[\tau,\nu] e^{j2\pi(t\nu/T - f\tau/D)}. \tag{2.25}$$

Here, T is the number of elements in the Doppler grid. Conversely, D is the number of possible delay taps, and thus number of used subcarriers. I define the number of total elements in the grid as $N = DT$. This DSFT is rewritten in matrix notation via one left-sided and one right-sided Fourier transforms

$$\boldsymbol{H} = \boldsymbol{F}_D^H \boldsymbol{S} \boldsymbol{F}_T. \tag{2.26}$$

$\boldsymbol{F}_D$ is the unitary discrete Fourier transform of size D. The inverse transform in this case equals

$$\boldsymbol{S} = \boldsymbol{F}_D \boldsymbol{H} \boldsymbol{F}_T^H. \tag{2.27}$$

2.3.2 Sparse Estimation: The c-LASSO

The goal is to represent a time-variant complex-valued frequency response $\boldsymbol{h}[i] \in \mathbb{C}^D$ through a sparse time-varying basis expansion $\boldsymbol{b}_{l_0}[i] \in \mathbb{C}^N$. The two vectors are linked by the basis $\boldsymbol{A} \in \mathbb{C}^{D \times N}$, and by defining the sparsity order K_0, I introduce the optimization problem

$$\boldsymbol{b}_{l_0}[i] = \arg\min_{\boldsymbol{b}} \| \boldsymbol{S}(\boldsymbol{h}[i] - \boldsymbol{A}\boldsymbol{b}) \|^2 \quad \text{s.t.} \quad \|\boldsymbol{b}\|_0 \leq K_0. \tag{2.28}$$

I call the set of indices $\mathcal{K}_0[i] \subset \mathcal{D}$ where $\boldsymbol{b}_{l_0}$ is nonzero at time i the *support* of $\boldsymbol{b}_{l_0}$, with $|\mathcal{K}_0[i]| = K_0$ for all i. As cost function $f_{0,\boldsymbol{S}}(\cdot)$ to be minimized I use a weighted version of the least squares,

$$f_{0,\boldsymbol{S}}(\boldsymbol{y}) = \boldsymbol{y}^H \boldsymbol{S}^H \boldsymbol{S} \boldsymbol{y}, \tag{2.29}$$

which allows assigning importance to frequency ranges, improve the estimate for those ranges while reducing the overall complexity. This objective function is a positive semidefinite program and thus convex [70]. However, the side-constraint is non-convex, which makes solving the optimization a difficult combinatorial problem. However, it was demonstrated, that the l_0-norm can be replaced with the l_1-norm, which leads to convex side constraints.

Die approbierte gedruckte Originalversion dieser Dissertation ist an der TU Wien Bibliothek verfügbar.
The approved original version of this doctoral thesis is available in print at TU Wien Bibliothek.
TU Bibliothek Your knowledge hub WIEN

This approach is called the c-LASSO [48]

$$\boldsymbol{b}_{l_1}[i] = \arg\min_{\boldsymbol{b}} \|\boldsymbol{S}(\boldsymbol{h}[i] - \boldsymbol{A}\boldsymbol{b})\|_2^2 \quad \text{s.t.} \quad \|\boldsymbol{D}\boldsymbol{b}\|_1 \leq \epsilon, \tag{2.30}$$

or, in its Lagrangian form

$$\boldsymbol{b}_{l_1}[i] = \arg\min_{\boldsymbol{b}} \left(\|\boldsymbol{S}(\boldsymbol{h}[i] - \boldsymbol{A}\boldsymbol{b})\|_2^2 + \mu\|\boldsymbol{D}\boldsymbol{b}\|_1\right). \tag{2.31}$$

The matrix $\boldsymbol{D}$ allows to adapt the penalties for different entries in $\boldsymbol{b}$ being nonzero, while μ is a regularization parameter that allows to tune the sparsity order of the resulting estimate [48]. By introducing $\boldsymbol{y} = \boldsymbol{S}\boldsymbol{h}$ and $\boldsymbol{A}' = \boldsymbol{S}\boldsymbol{A}$, the original formulation in [48] is reconstructed, allowing me to use the given results directly. These were shown to be optimal in the MSE sense. Here μ is a Lagrangian multiplier. The c-LASSO aims to minimize the MSE (via the squared 2-norm), and enforces sparse solutions through a 1-norm constraint.The formulation as given is a convex problem, and is thus solvable efficiently. In this work, I use the cvx toolbox [71]. Depending on the basis $\boldsymbol{A}$, and the magnitude of μ, a different number of nonzero parameters in different positions is chosen for $\hat{\boldsymbol{b}}_{\text{LASSO}}[t]$. In [48], Algorithm 1 was demonstrated which finds a M-sparse solution given a target $\boldsymbol{h}$, a basis $\boldsymbol{A}$ by iterating over μ until the correct sparsity order is found. When the algorithm has found a solution with the correct sparsity, the choice of $\hat{\boldsymbol{b}}$ may not be optimal in the MSE sense, as the algorithm is biased by the 1-norm. To ensure that for the resulting active set, the least-squares solution is found, the following refinement step is executed in line 18

$$\hat{\boldsymbol{b}} = \boldsymbol{E}(\boldsymbol{b})\left(\boldsymbol{A}\boldsymbol{E}(\boldsymbol{b})\right)^{\dagger}\boldsymbol{h}. \tag{2.32}$$

Here $\boldsymbol{E}(\boldsymbol{b})$ is a matrix defined as

$$E(\boldsymbol{b})[i,j] = \begin{cases} 1 & \text{if } b[i] \text{ is the } j\text{th nonzero entry of } \boldsymbol{b}, \\ 0 & \text{otherwise.} \end{cases} \tag{2.33}$$

This computes a least squares estimate for $\hat{\boldsymbol{b}}$ that only uses the M active taps found by the algorithm, and leaves the rest 0.

For the bisection on line 15, [48] gives progressive approximations for efficient implementations in Eq. (36–38). When iterating over a sequence of correlated vectors, such as time snapshots of frequency responses, the output μ is used as initial value μ_0 in the subsequent estimation process. In the subsequent sections, several approaches at configuring the algorithm depending on the design goal are detailed.

Configuration for Delay Line Estimation

After observing the channel response $\boldsymbol{h}$, a M-sparse delay line estimate $\boldsymbol{b}$ is required. This is obtained directly by using $\boldsymbol{F}$ as basis $\boldsymbol{A}$.

Die approbierte gedruckte Originalversion dieser Dissertation ist an der TU Wien Bibliothek verfügbar.
The approved original version of this doctoral thesis is available in print at TU Wien Bibliothek.
TU Bibliothek Your knowledge hub WIEN

Algorithm 1 c-LASSO Algorithm

procedure C-LASSO($\boldsymbol{h}, \boldsymbol{A}, M$)
  $w \leftarrow]0,1[$ ▷ Trade-off between speed and convergence
  $\epsilon \leftarrow \epsilon_0$ ▷ Threshold for detecting nonzero magnitudes.
  $\mu \leftarrow \mu_0$
  $M_0 \leftarrow 0$
  while $M_i \neq M$ **do**
    $i = i + 1$
    $\hat{\boldsymbol{b}} = \arg\min_{\boldsymbol{b}} \left(\| (\boldsymbol{h} - \boldsymbol{A}\boldsymbol{b}) \|_2^2 + \mu \|\boldsymbol{b}\|_1 \right)$
    if $M_i < M$ **then** ▷ Activate additional taps
      $\boldsymbol{u}_i = 2\boldsymbol{A}^H \left(\boldsymbol{h} - \boldsymbol{A}\hat{\boldsymbol{b}} \right)$
      $\mathscr{U} = \{m \mid 1 - \frac{u_i[m]}{\mu} < \epsilon\}$ ▷ Set of local maxima above threshold.
      $K = |\mathscr{U}| + 1$
      $\mu = (1-w)\ \text{peak}(\boldsymbol{u}_i, K) + w\ \text{peak}(\boldsymbol{u}_i, M+1)$
    else if $M_i > M$ **then** ▷ Deactivate unnecessary taps
      bisecting between $\mu[i-1]$ and $\mu[i-2]$. ▷ For details see [48]
    end if
  end while
  Refine estimate using Eq. (2.32)
  return $\hat{\boldsymbol{b}}, \mu$
end procedure

Configuration for Subband Cluster Estimation

Here, the c-LASSO is extended to the subband cluster structure from Eq. (2.22). Due to the concatenation of the P subband impulse responses, I have to define in what sense sparseness has to be ensured. For this, I want to estimate the same level of sparseness L_0 across all subband impulse responses, resulting in an overall sparseness of $M = P \cdot L_0$. This is achieved by extending the Lagrangian multiplier μ to a vector $\boldsymbol{\mu}$ of size $P \times 1$, and extending the c-LASSO as follows

$$\hat{\boldsymbol{b}}_{\text{subband}}[t] = \underset{\boldsymbol{b}_{\text{subband}}}{\arg\min} \Big(\| \boldsymbol{h}[t] - \overbrace{\left(\boldsymbol{I}^{P\times P} \otimes \boldsymbol{1}^{(N/P)\times N} \right) \odot \left(\boldsymbol{1}^{1\times P} \otimes \boldsymbol{F} \right)}^{\boldsymbol{A}_{\text{subband}}} \boldsymbol{b}_{\text{subband}} \|_2^2 + \| \left(\text{Diag}\left(\boldsymbol{\mu}^{P\times 1} \right) \otimes \boldsymbol{I}^{N\times N} \right) \boldsymbol{b}_{\text{subband}} \|_1 \Big). \tag{2.34}$$

Due to the orthogonality of the projections, this formulation can be rewritten as a joint optimization of the subband impulse responses

Die approbierte gedruckte Originalversion dieser Dissertation ist an der TU Wien Bibliothek verfügbar.
The approved original version of this doctoral thesis is available in print at TU Wien Bibliothek.
TU Bibliothek Your knowledge hub WIEN

$$\hat{\boldsymbol{b}}_1[t], \hat{\boldsymbol{b}}_2[t], \ldots = \underset{\boldsymbol{b}_1, \boldsymbol{b}_2, \ldots}{\operatorname{argmin}} \sum_{p=1}^{P} \left(\|\boldsymbol{Q}_p \big(\boldsymbol{h}[t] - \boldsymbol{F}\boldsymbol{b}_p\big)\|_2^2 + \mu_p \|\boldsymbol{b}_p\|_1 \right). \tag{2.35}$$

In this formulation, the sum terms do not depend on each other, hence the optimization is computed by optimizing every sum term individually. These, however, have the same structure as the c-LASSO and thus be optimized according to Algorithm 1.

Configuration for Joint Delay-Doppler Estimation

As a small reminder, the delay-Doppler channel $\boldsymbol{S}$ is related to the time-frequency channel $\boldsymbol{H}$ via the symplectic Fourier ([69]) transform given by

$$\boldsymbol{S} = \boldsymbol{F}_D \boldsymbol{H} \boldsymbol{F}_T^H. \tag{2.36}$$

The given transformation is vectorized and subjected to the identity $\text{vec}(\boldsymbol{ABC}) = (\boldsymbol{C}^T \otimes \boldsymbol{A})\text{vec}(\boldsymbol{B})$

$$\underbrace{\text{vec}(\boldsymbol{S})}_{=\boldsymbol{s}} = \underbrace{(\boldsymbol{F}_T^H \otimes \boldsymbol{F}_D)}_{=\boldsymbol{A}_{DT\times DT}} \underbrace{\text{vec}(\boldsymbol{H})}_{=\boldsymbol{h}}, \tag{2.37}$$

$$\boldsymbol{h} = \underbrace{(\boldsymbol{F}_T \otimes \boldsymbol{F}_D^H)}_{=\boldsymbol{A}_{DT\times DT}^{-1}} \boldsymbol{s}. \tag{2.38}$$

Here, the 2D-representation is calculated by applying the unvec$(\cdot)$ operation to the vectorizations. This representation now is again inserted directly into the c-LASSO algorithm.

Configuration for Sequential Estimation

In the previous sections, the estimation of $\boldsymbol{h}[t]$ was considered as an optimization problem completely independent of all other times t'. This is referred to as *memoryless estimation*. Now, I account for the fact that the delays in the delay lines relate to geometrical positions of scatterers. These are limited in their ability to move between two snapshots, hence the tap positions of adjacent snapshots have to reflect this. However, due to noisy observations, the tap positions end up fluctuating strongly in a memoryless estimation. Therefore, a sequential approach is introduced that tracks prior tap positions and encourages tap consistency in the estimation of the next snapshot. This is done by substituting $\boldsymbol{b} = \boldsymbol{D}^{-1}\boldsymbol{b}'$, and optimizing for $\boldsymbol{b}'$. As long as $\boldsymbol{D}$ is invertible, it acts as weighting matrix for the nonzero entries in $\boldsymbol{b}$, encouraging certain taps and discouraging other [72]. This is used to encourage consistency of tap positions, similar to [73]. The weight matrix $\boldsymbol{D}$ at time 0 is initialized as identity matrix like in the memoryless case. Then, iteratively, the weights are updated for new snapshots according to the following rules. A scatterer can physically move at most d delay samples

Die approbierte gedruckte Originalversion dieser Dissertation ist an der TU Wien Bibliothek verfügbar.
The approved original version of this doctoral thesis is available in print at TU Wien Bibliothek.
TU Bibliothek Your knowledge hub WIEN

between two snapshots. Thus, after calculating an estimate $\boldsymbol{b}[t]$,

$$D_{j,j}[t+1] = \Big(\sum_{k=j-d}^{j+d} D_{k,k}[t]^{-1} \Big)^{-1}, \tag{2.39}$$

is updated for all j that are within d taps of at least 1 nonzero entry of $\boldsymbol{b}[t]$. This always reduces the diagonal entry, making it less penalized in the optimization, and thus more likely to be picked again. For all entries that were not modified in the previous step, a penalty is added

$$D_{j,j}[t+1] = D_{j,j}[t] + 0.05. \tag{2.40}$$

This ensures that scarcely activated taps get progressively penalized, ensuring that random noise is less likely to activate such a tap. In this case, $d = 1$ is used since 2 ns delay resolution and 100 μs snapshot resolution are used. Due to these numbers, a scatterer can physically only move 1 tap between snapshots. Finally, stability of the algorithm has to be ensured. This is done by setting the minimum value of a diagonal element to $D_{j,j}^{\min} = 0.01$. Furthermore, $D_{j,j}^{\max} = 2$, as new taps may actually spawn. The values of these parameters are manipulated to achieve a trade-off between algorithm convergence and geometric consistency.

2.4 Propagation Channel Data

To demonstrate the performance of this approach, two sets of channel data are presented. First, synthetic data is used to test the algorithm under lab conditions. The Saleh-Valenzuela channel model [74] generates synthetic clustered data that is analyzed. Furthermore, vehicular mmWave channel measurements are presented to test this algorithm with actual measurements. The next two sections give a short overview over these data sets.

2.4.1 Saleh-Valenzuela Channels

Saleh and Valenzuela published their channel model for clustered indoor channels in 1987 [74]. This model targets wideband indoor channels, and is based on the observation that the power arrived in clusters of multipaths. While the model was initially proposed for indoor settings, its wide bandwidth characteristic makes it attractive for mmWave channel modeling [75, 76], and has also been applied to outdoor channels [77]. The channel is modeled as

$$h[\tau, t] = \sum_{l=0}^{L} \sum_{k=0}^{K} \beta_{l,k}[t] \exp(j\phi_{k,l}[t]) \delta[\tau - T_k - \tau_{k,l}]. \tag{2.41}$$

Here, T_k is the arrival time of the kth cluster, and $\tau_{k,l}$ is the delay of the kth multipath component within the lth cluster. The phases of all multipath components $\phi_{k,l}$ are i.i.d.

Die approbierte gedruckte Originalversion dieser Dissertation ist an der TU Wien Bibliothek verfügbar.
The approved original version of this doctoral thesis is available in print at TU Wien Bibliothek.
TU Bibliothek Your knowledge hub WIEN

Table 2.1: Saleh-Valenzuela parameter combinations.

Paramter unit	Unit	Symbol	Conf. (a) [78]	Conf. (b)	Conf. (c)	Conf. (d)
Cluster energy decay	ns	Γ	60	60	120	120
Cluster arrival rate	ns^{-1}	Λ	1/300	1/90	1/90	1/30
MPC energy decay	ns	γ	20	20	20	20
MPC arrival rate	ns^{-1}	λ	1/5	1/5	5	5

uniform distributed, while all path amplitudes $\beta_{l,k}$ are Rayleigh distributed with second non-central moment defined as

$$\mathrm{E}\left(\beta_{l,k}^2\right) = \beta_{0,0}^2 \exp\left(-T_k/\Gamma\right) \exp\left(\tau_{k,l}/\gamma\right) , \tag{2.42}$$

with Γ being the power decay parameter of the individual clusters, and γ the power decay parameter of the MPCs within one cluster. The delay between the $(k-1)$th and the kth cluster, as well as the delay between the $(l-1)$th and lth MPC within a cluster are exponentially distributed

$$f(T_k|T_{k-1}) = \Lambda \exp\left(-\Lambda(T_k - T_{k-1})\right), \tag{2.43}$$

$$f(\tau_{k,l}|\tau_{k,l-1}) = \lambda \exp\left(-\lambda(\tau_{k,l} - \tau_{k,l-1})\right). \tag{2.44}$$

Four configurations are considered for the channel model, that are outlined in Table 2.1. Configuration (a), is directly adapted from [78]. Configuration (b) increases the cluster arrival rate, configuration (c) uses the same cluster arrival rate as (b), but uses denser MPCs within the clusters, and finally (d) uses the dense clusters from (c), but increases the number of clusters even more. Sample traces for the 4 configurations are shown in Fig. 2.6. The dashed line indicates the cluster power decay, while dotted lines indicate the intra-cluster power decays for the individual clusters.

Die approbierte gedruckte Originalversion dieser Dissertation ist an der TU Wien Bibliothek verfügbar.
The approved original version of this doctoral thesis is available in print at TU Wien Bibliothek.
TU Bibliothek Your knowledge hub WIEN

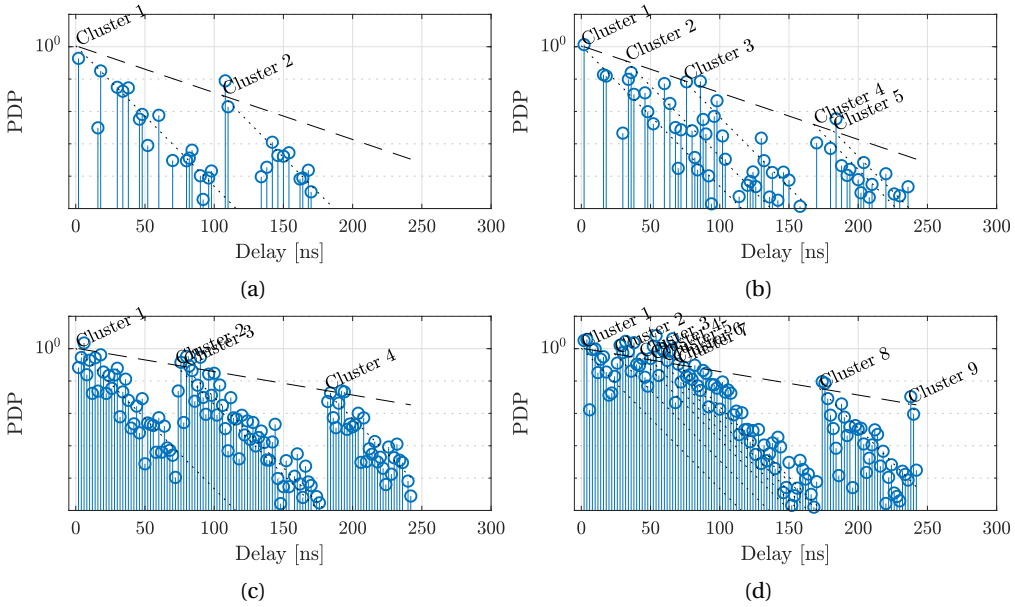

Figure 2.6: Sample Saleh-Valenzuela Power Delay Profiles (PDPs). The plots show a realization for Conf. **(a)**,**(b)**,**(c)** and **(d)**, each produced with the same random seed.

2.4.2 mmWave V2V Channel Sounding Campaign

A detailed description of the measurement campaign and the measurement setup is found in [32]. The key parameters are shown in Table 2.2. In order to achieve accurate frequency and time synchronization, TX (a tripod) and RX (the silver Mazda) are kept static and connected both with a 10 MHz frequency reference and a trigger cable, see Fig. 2.7. To obtain time-variant vehicular channels, the urban street traffic passed by. This effectively emulates a platooning scenario, where the car platoon is being overtaken. A measurement is triggered once an overtaking vehicle of the urban street traffic drives through a light barrier. The sample rate at the receiver is 600 Msamples/s. A multi-tone sequence is used with $N = 121$ carriers to approximately achieve a tone spacing of 5 MHz. Due to the anti-aliasing filter, the cut-off region is avoided and the sounding sequence is only transmitted at the $N_s = 101$ center tones. Thereby, an effective sounding bandwidth of 510 MHz is achieved. The output of the channel sounder is the calibrated time-variant transfer function $h[f,t]$.

The campaign measured different overtaking vehicle types (passenger cars, Sports Utility Vehicle (SUV)s, trucks) with different transmit and receive antennas. A detailed picture of the transmitter tripod and the receive antenna mounting is shown in Fig. 2.8.

Die approbierte gedruckte Originalversion dieser Dissertation ist an der TU Wien Bibliothek verfügbar.
The approved original version of this doctoral thesis is available in print at TU Wien Bibliothek.
TU Bibliothek Your knowledge hub WIEN

Table 2.2: Channel sounding measurement parameters

Parameter	Value
Center frequency	60 GHz
Subcarrier spacing	4.96 MHz
Number of subcarriers	102
Snapshot rate	129.1 μs
Delay resolution	1.96 ns
Recording time	720 ms

Figure 2.7: Photograph of the measurement site. The transmitter and receiver are static and urban street traffic is driving by.

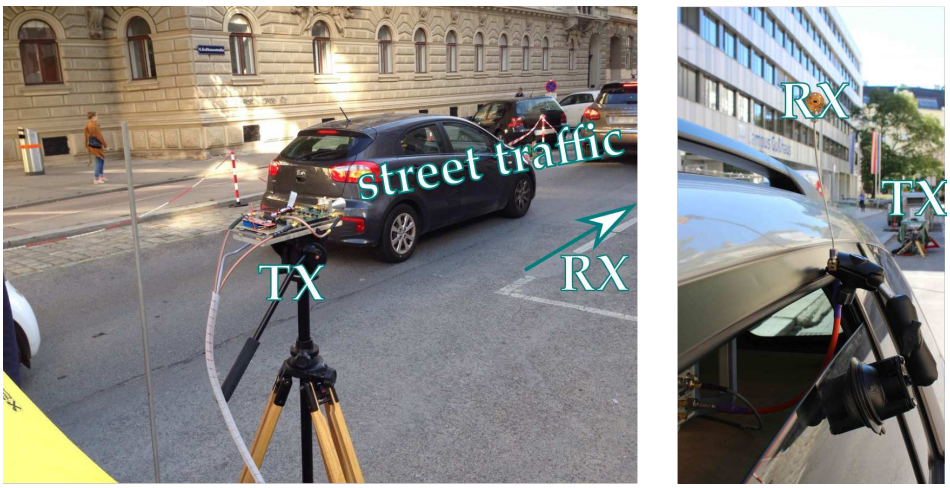

Figure 2.8: Zoomed photographs of the measurement site. On the left-hand side the photo shows the transmit horn antenna mounted on a tripod. As multiple reflection with the transmitter car are below the receiver sensitivity, the TX car is replaced with a tripod. On the right-hand side the photo shows the open-ended waveguide receive antenna mounted at roof height at the left, rear car side window.

Die approbierte gedruckte Originalversion dieser Dissertation ist an der TU Wien Bibliothek verfügbar.
The approved original version of this doctoral thesis is available in print at TU Wien Bibliothek.
TU Bibliothek Your knowledge hub WIEN

2.5 Results

2.5.1 Performance Evaluation

As mentioned above, in the measurements, out of $N = 121$ total subcarriers, only the $N_s = 101$ center subcarriers carry meaningful data. Hence, $\boldsymbol{A} = \boldsymbol{SF}$, with

$$\boldsymbol{S} = \mathrm{Diag}\left(\left[\mathbf{0}^{1\times(N-N_S)/2} \quad \mathbf{1}^{1\times N_S} \quad \mathbf{0}^{1\times(N-N_S)/2}\right]\right). \tag{2.45}$$

This ensures that the unused subcarriers do not factor into the estimation.

Evaluation of Estimation quality: MSE

I define the MSE as dependent on the bandwidth of interest, defined through $\boldsymbol{S}$

$$\mathrm{MSE}(\boldsymbol{h}, \boldsymbol{A}\hat{\boldsymbol{b}}) = \frac{\|\boldsymbol{S}(\boldsymbol{h} - \boldsymbol{A}\hat{\boldsymbol{b}})\|_2^2}{N_s}. \tag{2.46}$$

Including the matrix $\boldsymbol{S}$ in the MSE is essential to assess fits that are only fit to the targeted subcarriers in $\boldsymbol{S}$.

Evaluating the Model Order: AIC

In general, the AIC is a measure that weighs estimation accuracy in the form of the likelihood function against the number of parameters needed to describe the model. It is defined as [79]

$$\mathrm{AIC}(\boldsymbol{h}, \boldsymbol{s}) = 2k \underbrace{\frac{N}{N-k-1}}_{\text{bias correction}} - 2\ln(\max_{\boldsymbol{s}} \mathscr{L}(\boldsymbol{s}; \boldsymbol{h})), \tag{2.47}$$

where $\mathscr{L}(\boldsymbol{s}; \boldsymbol{h}))$ is the likelihood function of $\boldsymbol{h}$ given the parametrization of $\boldsymbol{s}$. The logarithm of the likelihood function is penalized by a function that depends on the model order k. Therefore, it is only worth to increase the model order by 1, if the natural logarithm of the maximum likelihood value is also increased by that number. Otherwise, investing the parameter does not adequately improve the estimation quality.

The fraction that is denoted as bias correction is not part of the original AIC formulation [80], but has been introduced after it was found that, given $\frac{N}{k} < 40$, the AIC provides biased results . This correction term provides improved unbiased results also under these conditions.

I assume that the estimates approximate the maximum likelihood estimate utilized in Eq. (2.47), that is $\hat{\boldsymbol{s}} \approx \arg\max_{\boldsymbol{s}} \mathscr{L}(\boldsymbol{s}; \boldsymbol{h}))$. This behavior was for example observed and documented in [52].

Die approbierte gedruckte Originalversion dieser Dissertation ist an der TU Wien Bibliothek verfügbar.
The approved original version of this doctoral thesis is available in print at TU Wien Bibliothek.
TU Bibliothek Your knowledge hub WIEN

If this condition holds, the estimation error is unbiased and converges towards an i.i.d. complex normal distribution $e \sim \mathcal{CN}(0,\sigma^2)$ [81]. Then, the maximum likelihood and the accompanying log-likelihood is given by

$$\begin{aligned}\mathcal{L}(\hat{\boldsymbol{s}};\boldsymbol{h}) &= \frac{1}{\sqrt{(\pi)^N \det(\boldsymbol{C})}} \exp\Big(-(\boldsymbol{h}-\boldsymbol{A}\hat{\boldsymbol{s}})^H \boldsymbol{C}^{-1}(\boldsymbol{h}-\boldsymbol{A}\hat{\boldsymbol{s}})\Big),\\ \ln\mathcal{L}(\hat{\boldsymbol{s}};\boldsymbol{h}) &= -\frac{N}{2}\ln(2\pi) - \frac{1}{\sigma^2}\underbrace{\|\boldsymbol{h}-\boldsymbol{A}\hat{\boldsymbol{s}}\|_2^2}_{\text{RSS}} - N\ln(\sigma^2),\end{aligned} \tag{2.48}$$

where RSS denotes the residual sum of squares. From this, I compute an estimated noise variance $\hat{\sigma}^2 = \frac{\text{RSS}}{N}$. Then, the AIC is written as

$$\text{AIC} = 2k\frac{N}{N-k-1} + N\ln(\pi) + \frac{N\hat{\sigma}^2}{\sigma^2} + N\ln(\sigma^2). \tag{2.49}$$

I now assume that enough samples are used for the noise variance estimate $\hat{\sigma}^2$ to converge towards the actual noise variance σ^2. Equation (2.49) simplifies to

$$\begin{aligned}\text{AIC}(\boldsymbol{h},\hat{\boldsymbol{s}}) &= 2k\frac{N}{N-k-1} + N\ln(\pi) + N + N\ln(\sigma^2)\,,\\ &= 2k\frac{N}{N-k-1} + N(\ln(\pi)+1) + N\ln\left(\frac{RSS}{N}\right).\end{aligned} \tag{2.50}$$

Frequently, the term $N\ln(\pi+1)$ is dropped, as it is not dependent on k or the estimation quality, hence is not contributing to the evaluation of the optimal k. However, for parts of the evaluation, I want to make evaluations also with respect to N, hence the terms are kept. When the dimensionality of the data is increased, so is the number of realizations, and hence it is more probable to find a good sparse representation. This is seen in the last two terms of Eq. (2.50). There, as long as $\ln(\text{RSS}/N) < -(\ln(2\pi)+1)$, the AIC is decreased progressively by increasing N.

I now introduce a second measure, the normalized $\text{AIC}^{(n)}(\boldsymbol{h},\hat{\boldsymbol{s}})$. This is achieved by dividing the $\text{AIC}(\boldsymbol{h},\hat{\boldsymbol{s}})$ by N,

$$\text{AIC}^{(n)}(\boldsymbol{h},\hat{\boldsymbol{s}}) = \underbrace{\frac{2k}{N}\left(\frac{N}{N-k-1}\right)}_{\text{normalized bias}} + \underbrace{\ln(2\pi)+1+\ln\left(\frac{RSS}{N}\right)}_{\text{normalized likelihood}}. \tag{2.51}$$

I introduce this measure to specifically test for dimensionality dependence. This behavior is eliminated in the normalized AIC.

Die approbierte gedruckte Originalversion dieser Dissertation ist an der TU Wien Bibliothek verfügbar.
The approved original version of this doctoral thesis is available in print at TU Wien Bibliothek.
TU Bibliothek Your knowledge hub WIEN

Akaike Weights

Based on the given formulations, I introduce the regular and normalized Akaike weights similar to [82]

$$\Phi_j = \mathrm{AIC}_j - \min_i(\mathrm{AIC}_i), \tag{2.52}$$

$$\Phi_j^{(n)} = \mathrm{AIC}_j^{(n)} - \min_i\left(\mathrm{AIC}_i^{(n)}\right), \tag{2.53}$$

$$w_j = \frac{\exp(-\Phi_j/2)}{\sum_{i=1}^{J}\exp(-\Phi_i/2)}, \tag{2.54}$$

$$w_j^{(n)} = \frac{\exp(-\Phi_j^{(n)}/2)}{\sum_{i=1}^{J}\exp(-\Phi_i^{(n)}/2)}. \tag{2.55}$$

Comparison: Peak Search

To assess the algorithm, I compare it to the performance of *peak search*. The estimate is done by calculating the dense impulse response $\boldsymbol{b} = \boldsymbol{F}^{-1}\boldsymbol{h}$. Then, all entries except the ones with the largest M magnitudes are set to 0, resulting in $\hat{\boldsymbol{b}}_M$. Afterwards, the estimate is refined again according to Eq. (2.32), resulting in the M sparse estimate

$$\hat{\boldsymbol{b}}_{\text{peak}} = \boldsymbol{E}(\boldsymbol{b})\left(\boldsymbol{A}\boldsymbol{E}(\boldsymbol{b})\right)^{\dagger}\boldsymbol{h}. \tag{2.56}$$

If $P = 1$ and $\boldsymbol{D} = \boldsymbol{S} = \boldsymbol{I}^{N\times N}$, the matrix $\boldsymbol{A}$ becomes a square orthonormal basis matrix. Under this assumption, the c-LASSO optimization simplifies to peak search.

2.5.2 Performance Analysis for Synthetic Data

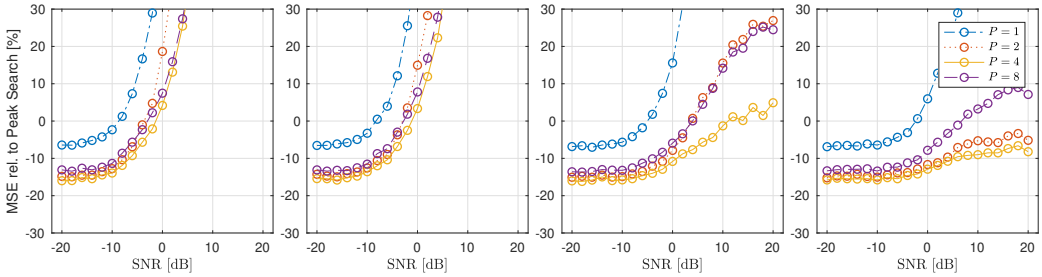

Figure 2.9: Relative change of MSE for the 4 configurations **(a)–(d)** of the Saleh-Valenzuela models.

Here, I analyze the performance of the c-LASSO algorithm on synthetic data given by the four configurations of the Saleh-Valenzuela model in Section 2.4.1. The main focus here is

Die approbierte gedruckte Originalversion dieser Dissertation ist an der TU Wien Bibliothek verfügbar.
The approved original version of this doctoral thesis is available in print at TU Wien Bibliothek.
TU Bibliothek Your knowledge hub WIEN

how well the c-LASSO performs, depending on the *MPC density* of the clusters. Since the density of the channel is a design parameter here, the AICs optimum is itself a function of the model parameter choices, and is of little interest. Instead, analysis is presented on how much improvement over peak search is achieved, depending on the chosen basis, as well as the channel model configuration. Hence, the relative change of MSE from $\hat{\boldsymbol{b}}_{\text{peak}}$ to $\hat{\boldsymbol{b}}$ is calculated as

$$\text{MSE}_{\text{rel.}}(\hat{\boldsymbol{b}}_{\text{peak}}, \hat{\boldsymbol{b}}) = \frac{\text{MSE}(\boldsymbol{h}, \boldsymbol{A}\hat{\boldsymbol{b}}) - \text{MSE}(\boldsymbol{h}, \boldsymbol{A}\hat{\boldsymbol{b}}_{\text{peak}})}{\text{MSE}(\boldsymbol{h}, \boldsymbol{A}\hat{\boldsymbol{b}}_{\text{peak}})} \,. \tag{2.57}$$

This is also referred to as the Normalized Mean Squared Error (NMSE). In Fig. 2.9, this relative MSE is plotted in percent (%) from peak search to c-LASSO with $P \in \{1,2,4,8\}$ for all four parameter sets over per-subcarrier SNR. All fits, both peak and c-LASSO have been done with a total of $M = 16$ degrees of freedom. The results show that the c-LASSO always outperforms peak search in the low SNR-regime, indicating that the c-LASSO works as a more robust estimator than peak search. However, of even more interest is that if the channel model shows *dense* MPC clusters (scenarios (c) and (d)), then, the performance of the c-LASSO improves in the high-SNR regime. For the subband cases of $P = 2,4$, the algorithm uniformly outperforms that the given assumption holds, that subband-fitting is able to exploit the signal structure resulting from few MPC clusters that are densely populated to achieve better performance with equal number of degrees of freedom. Finally, the best performance is achieved at $P = 4$, for $P = 8$, the performance decreases again.

2.5.3 Performance Analysis for Tapped and Clustered Delay Line Estimates

Figure 2.10 shows an example result for the c-LASSO output. In black, the impulse response calculated from the original channel sounder data is shown. Furthermore, three different configurations for estimations with $M = 16$ are displayed. For each plot, the positions of the P partial impulse responses are shown below the main plot. Additionally, the cluster impulse response Eq. (2.16) is overlaid, as well as an estimate for the noise floor. The median is used to estimate this noise floor [83]. The plot illustrates that the impulse response shows clustered shapes, and the subband cluster approach is able to better estimate this cluster structure without expending additional degrees of freedom. The tap positions within the subband responses are highly correlated, relating to the positions of the overall clusters.

A time evolution of the tap positions of one measurement is shown in Fig. 2.11. Here, the delays are color coded by arrival time, e.g. the latest estimated tap is always red. To facilitate comparison, one partial subband impulse response for every configuration is shown, always with $K_0 = 4$. The results are shown both for memoryless estimation as well as sequential estimation. The results show that the memoryless estimation shows strong fluctuations of the tap positions within small time spans. Furthermore, for larger P, the taps tend to be spread

Die approbierte gedruckte Originalversion dieser Dissertation ist an der TU Wien Bibliothek verfügbar.
The approved original version of this doctoral thesis is available in print at TU Wien Bibliothek.
TU Bibliothek Your knowledge hub WIEN

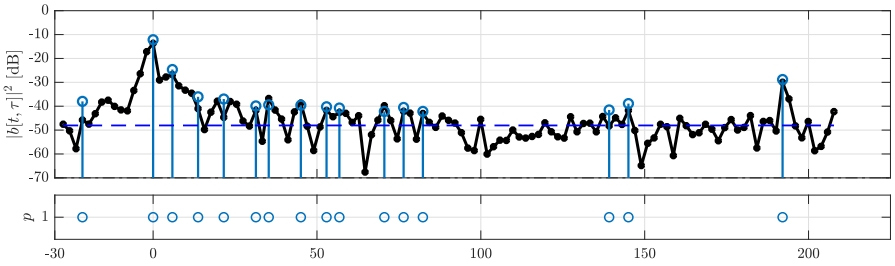

(a) $P = 1$, $K_0 = 16$

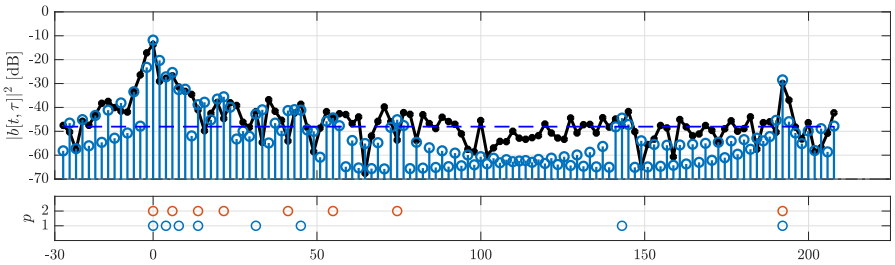

(b) $P = 2$, $K_0 = 8$

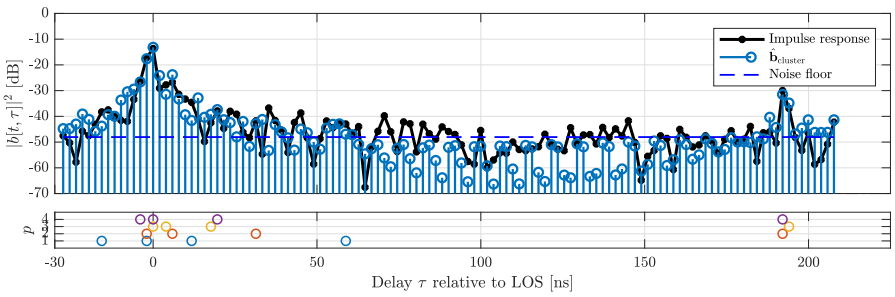

(c) $P = 4$, $K_0 = 4$

Figure 2.10: Sample impulse responses, estimated cluster impulse responses and cluster locations for $M = 16$ and $P \in \{1,2,4\}$ (**(a)**, **(b)** and **(c)**).

out more. This is because of the reduced spatial resolution, which means that close taps are not distinguishable and are represented by one tap. This allows a later tap to be active more likely, as the cluster close to the LOS path collapses and does not use additional taps. In comparison, the sequential estimation effectively reduces the position fluctuations. The taps can still fluctuate in short time spans. This occurs for example in the measurement when late in the time sequence, a strong late multipath occurs. At that moment, the fixed amount of taps is redistributed, and hence the positioning appears to "jump". However, the overall spatial consistency is drastically improved.

Finally, Fig. 2.12 shows the MSE and AIC for four different measurement runs. The graphs are all shown once with respect to M. As is shown, $P = 4$ memoryless is uniformly the best estimator for all M. In the case of the Horn-to-Open-Ended Waveguide (OEW) measurements, the gain over peak search is sizable. Here the spatial filtering leads to a low number of total clusters, meaning that large gains are achieved by applying the c-LASSO. On the other hand,

Die approbierte gedruckte Originalversion dieser Dissertation ist an der TU Wien Bibliothek verfügbar.
The approved original version of this doctoral thesis is available in print at TU Wien Bibliothek.
TU Bibliothek Your knowledge hub WIEN

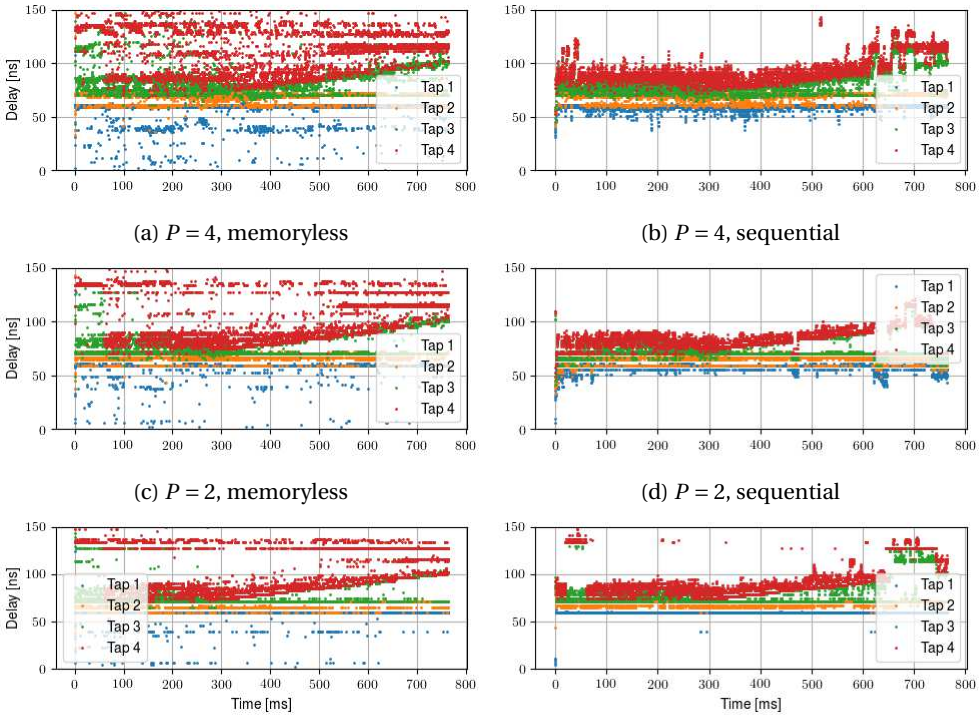

(a) $P = 4$, memoryless

(b) $P = 4$, sequential

(c) $P = 2$, memoryless

(d) $P = 2$, sequential

(e) $P = 1$, memoryless

(f) $P = 1$, sequential

Figure 2.11: 4-tap delay evolution for an overtaking SUV. Memoryless estimations on the left (**(a), (c), (e)**), sequential estimations on the right (**(b), (d), (f)**).

for the Omni-to-Omni measurements, the least amount of spatial filtering is applied, and conversely the c-LASSO estimation suffers. However, even for this worst case, the c-LASSO performs at least as well as peak search. In terms of modeling trade-off, the non-normalized AIC shows a clear minimum (denoted by dots) for all models. The optimal trade-off in terms of AIC is always achieved by the $P = 4$ memoryless c-LASSO at M between 8 and 16.

Die approbierte gedruckte Originalversion dieser Dissertation ist an der TU Wien Bibliothek verfügbar.
The approved original version of this doctoral thesis is available in print at TU Wien Bibliothek.

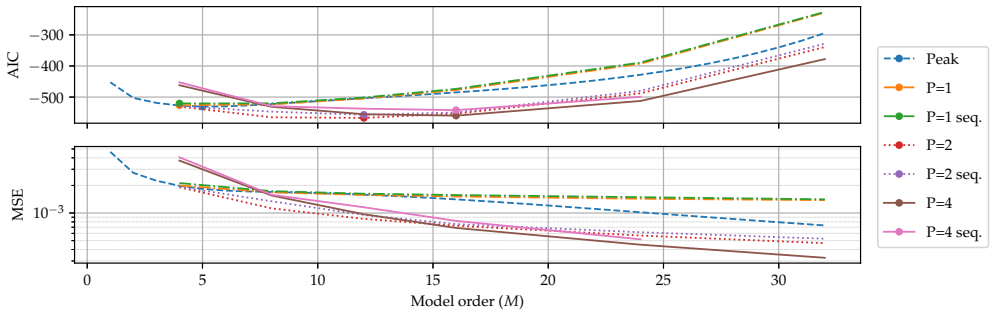

(a) Horn-OEW co-polarized, Truck.

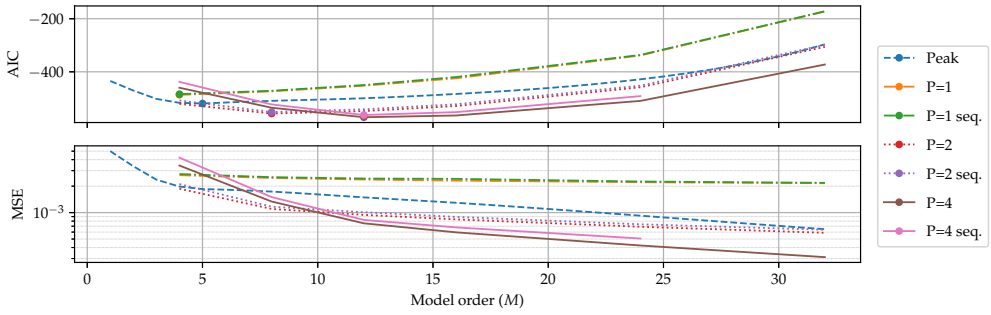

(b) Horn-OEW co-polarized, SUV.

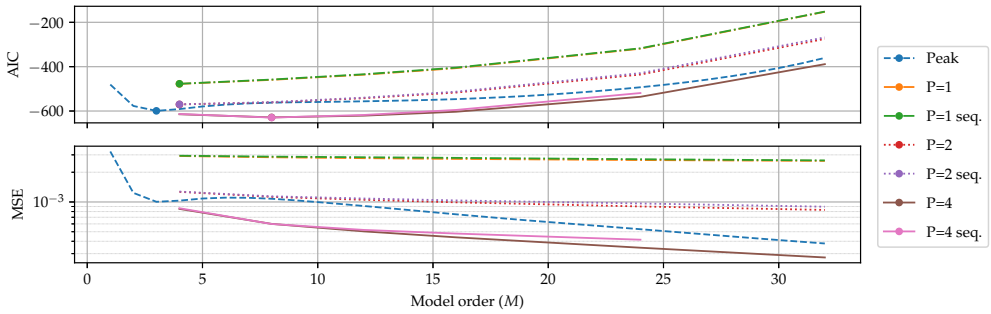

(c) Horn-OEW cross-polarized, passenger car.

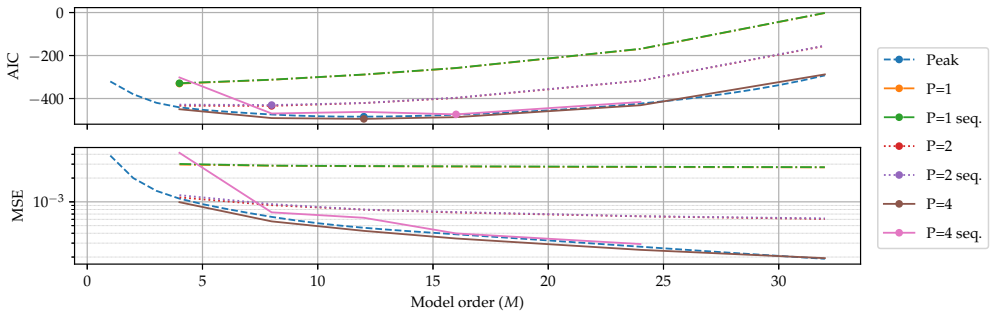

(d) Omni-Omni co-polarized, small truck.

Figure 2.12: MSE and AIC of the analyzed measurements (**(a)–(d)**).

Die approbierte gedruckte Originalversion dieser Dissertation ist an der TU Wien Bibliothek verfügbar.
The approved original version of this doctoral thesis is available in print at TU Wien Bibliothek.
TU Bibliothek Your knowledge hub WIEN

Sequential estimation introduces a small MSE-penalty, which is due to the additional side-constraint that was introduced. This penalty is generally very small, and the $P = 4$ sequential c-LASSO is the second best c-LASSO estimator by a large margin, and only for the Omni-to-Omni setup, peak search slightly outperforms the c-LASSO estimator. However, this comparison is not entirely fair, as peak search never considers spatial consistency.

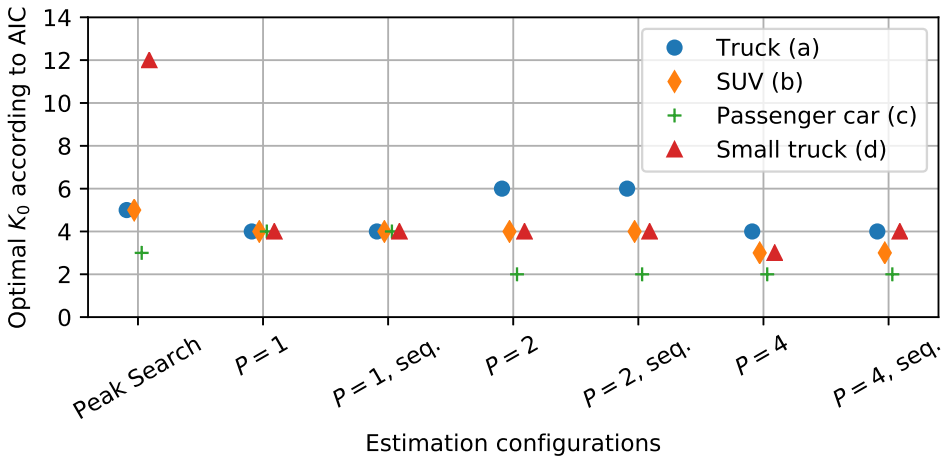

Figure 2.13: Optimal number of clusters K_0 for all presented estimation basis and measurements. The numbering is consistent with Fig. 2.12.

Now, the AIC is used to estimate the number of relevant scattering clusters. To analyze this, I take the optimal M from Fig. 2.12, and calculate the number of clusters K_0 from it. The results of this for all measurements and estimation configurations are shown in Fig. 2.13 for overtaking scenario. Using the normalization with respect to K_0, one clearly sees that all estimation configurations see a consistently small amount of relevant multipath clusters. All c-LASSO configurations have the optimal trade-off between $K_0 = 2-6$ clusters, with the large truck contributing the most clusters. Using the normalization with respect to K_0, the results show that for the given measurement setup, the algorithm never require more than at most $6-8$ multipath clusters K_0.

2.5.4 Delay-Doppler Grid

I now consider the same analysis based on a two-dimensional delay-Doppler grid. This analysis has been done with a different set of measurements. Unfortunately, due to the high-dimensional signal space, it was not trivial to replicate the results with the V2V overtaking measurements. Hence, I now give a brief overview over the used dataset, which resulted from investigating a Vehicle-to-Infrastructure (V2I) scenario. Afterwards, the results of the estimation are presented.

Die approbierte gedruckte Originalversion dieser Dissertation ist an der TU Wien Bibliothek verfügbar.
The approved original version of this doctoral thesis is available in print at TU Wien Bibliothek.
TU Bibliothek Your knowledge hub WIEN

Figure 2.14: Image of measurement setup.

Table 2.3: Channel sounding measurement parameters

Parameter	Value	
Center frequency	60.15	GHz
Subcarrier spacing	4.76	MHz
Number of subcarriers	21	
Snapshot rate	178.07	μs
Delay resolution	10	ns
Recording time	3600	ms

V2I Measurements 2018

The measurements took place at an urban street crossroads as shown in Fig. 2.14. The TX antenna is a 20 dBi conical horn antenna mounted on a vehicle roof. The horn antenna is directed in driving direction; towards the crossroads. The RX antenna is a $\lambda/4$ monopole antenna mounted on a crane arm, directly above the crossroads. The thereby elevated RX antenna is at a common infrastructure height of 5 m. Each measurement recording is limited to 3600 ms and starts approximately 30 m before the crossroads, with the car approaching and crossing the crossroads. The channel sounding parameters are provided in Table 2.3. For more details regarding the measurement campaign, refer to [33].

Die approbierte gedruckte Originalversion dieser Dissertation ist an der TU Wien Bibliothek verfügbar.
The approved original version of this doctoral thesis is available in print at TU Wien Bibliothek.

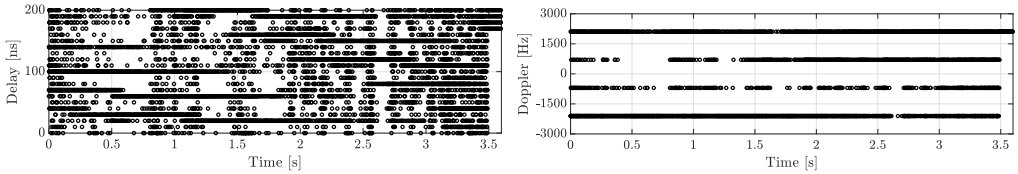

(a) Delay over time. Aggregation 4 (= 0.71 ms)

(b) Doppler over time. Aggregation 4 (= 0.71 ms)

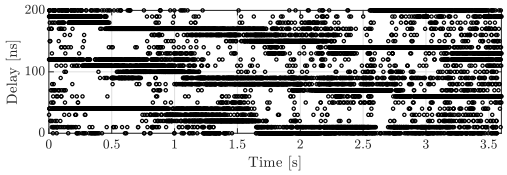

(c) Delay over time. Aggregation 8 (= 1.42 ms)

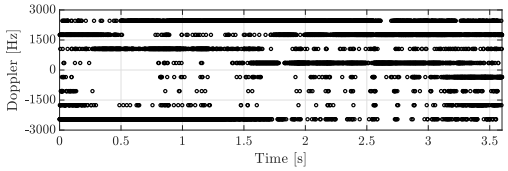

(d) Doppler over time. Aggregation 8 (= 1.42 ms)

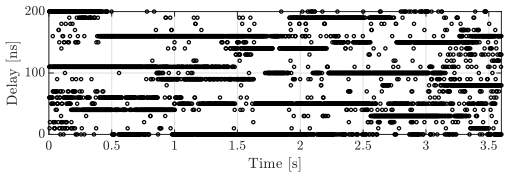

(e) Delay over time. Aggregation 16 (= 2.85 ms)

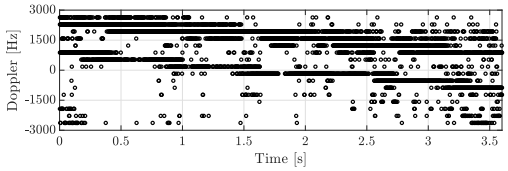

(f) Doppler over time. Aggregation 16 (= 2.85 ms)

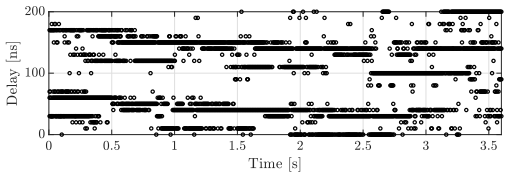

(g) Delay over time. Aggregation 32 (= 5.7 ms)

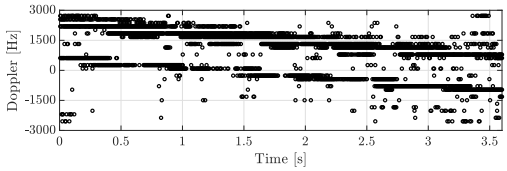

(h) Doppler over time. Aggregation 32 (= 5.7 ms)

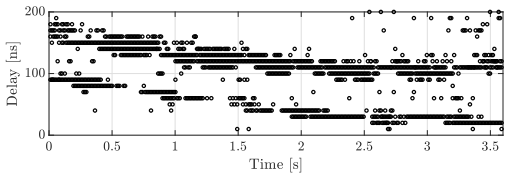

(i) Delay over time. Aggregation 64 (= 11.4 ms)

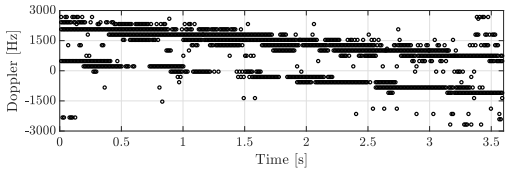

(j) Doppler over time. Aggregation 64 (= 11.4 ms)

Figure 2.15: Channel estimations with Sparseness $M = 4$ and time aggregations of $T \in \{4, 8, 16, 32, 64\}$. The left plots show the positions of the delay estimates, the right plots the positions in Doppler domain. The grid is circularly shifted to avoid wraparounds in delay domain.

Die approbierte gedruckte Originalversion dieser Dissertation ist an der TU Wien Bibliothek verfügbar.
The approved original version of this doctoral thesis is available in print at TU Wien Bibliothek.

Results

The c-LASSO optimizations are calculated for sparseness choices of $\{4,6,8,12,16,24\}$, and time aggregations of $T \in \{4,8,16,32,64\}$. Example results are shown in Fig. 2.15, which demonstrates example results for one measurement run. It shows the estimated positions in delay and Doppler for all analyzed time aggregations and a sparsity of $K_0 = 4$. Since the channel properties do not change with respect to a constant circular shift in delay domain, I shifted the delay domain such that the minimal tap delay over a measurement run equals 0. The presented traces show that a considerable amount of measurement noise for small time aggregations. Hence, the delay estimates fluctuate strongly from estimate to estimate for $T = 4$. As the time aggregation is extended, both delay and Doppler estimates become noticeably less noisy. This is caused by the effect of collecting more energy introduced by extending the estimation over a longer time block. Figure 2.16a shows the AIC evaluations for the presented time aggregations and chosen sparsities. The figure furthermore shows the Akaike weights calculated for each sparsity within a time aggregation. The AIC curves in the non-normalized plot appear to be straight lines, because the AIC value is dominated by the dimensionality N. Within one aggregation, only small changes are caused due to choosing different sparsities. The Akaike weights on the other hand show that for each aggregation, there is a clearly optimal sparsity choice, which are indicated by the weight w_j being close to 1. These results show that the estimation quality is strongly dependent on the aggregation period, and that for every aggregation, a clear optimal choice of sparsity is found.

However, I also investigate whether the delay-Doppler domain is inherently sparse, or if estimation only improves due to dimensionality. Therefore, the normalized AIC is considered (Fig. 2.16b). The normalization allows to see the dependence on the sparsity more clearly. It shows that for small aggregations, the $K_0 = 4$ is optimal. This is a strong indicator that the measurement noise is dominating. As the time aggregation is extended, the optimal choice for K_0 increases, however the choice stays sparse compared to the dimensionality N (given by 21 times the time aggregation). The figure also shows that when normalizing with respect to the dimensionality, all the estimators produce highly similar scores. This indicates that the main gain from time aggregation comes from increased energy and dimensionality. In Fig. 2.17, a histogram is plotted of Akaike weights computed for four different measurements and all listed time aggregations. The plot shows the same trend, that the non-normalized AIC tends to have clear best choices (spike at 1) and clearly worse choices (large spike at 0), whereas normalization leads to a spread around 0.2. This does indicate that the larger time-frequency grid leads to strongly improved estimation qualities. However, the normalized Akaike weights are all clustered at low values with no estimate being close to 1. This shows again that the optimal choice is mainly due to the large dimension, and not due to finding an inherently better matching basis.

Die approbierte gedruckte Originalversion dieser Dissertation ist an der TU Wien Bibliothek verfügbar.
The approved original version of this doctoral thesis is available in print at TU Wien Bibliothek.
TU Bibliothek Your knowledge hub WIEN

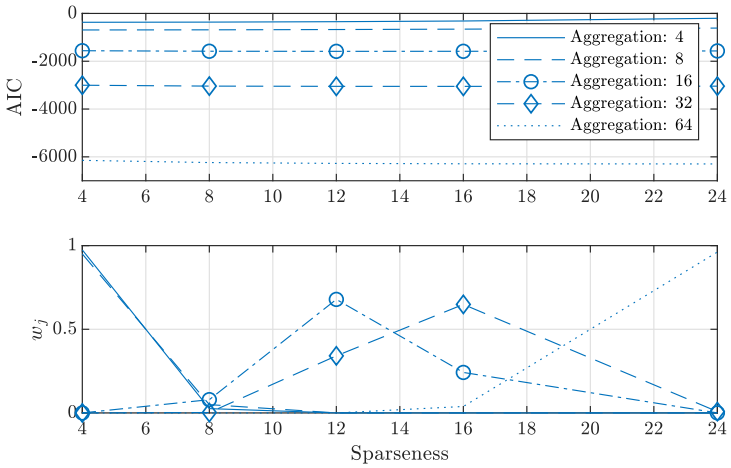

(a) Non-normalized AIC of the presented analysis.

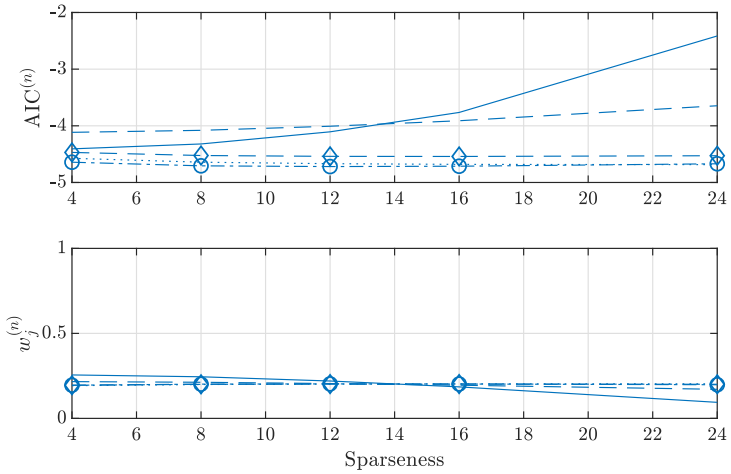

(b) $\mathrm{AIC}^{(n)}$ of the presented analysis.

Figure 2.16: Comparison of AIC and $\mathrm{AIC}^{(n)}$.

Die approbierte gedruckte Originalversion dieser Dissertation ist an der TU Wien Bibliothek verfügbar.
The approved original version of this doctoral thesis is available in print at TU Wien Bibliothek.

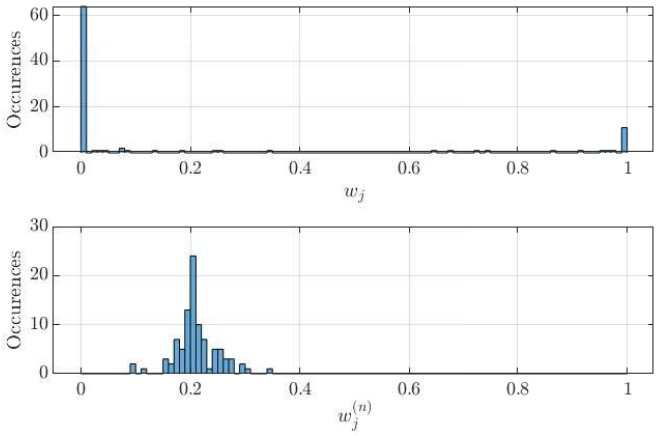

Figure 2.17: Histogram of the computed Akaike weights, for non-normalized AIC (above) and normalized AIC (below).

2.6 Discussion

The approach provided in this chapter acts to solve two interlinked problems. The first one is an identification problem. By combining sparse techniques such as the c-LASSO with the AIC, I identify the optimal model order given a specific basis. Optimal in this sense refers to capturing the signal of interest, and avoid fitting measurement noise. If I don't choose the AIC-optimal working point, I instead parameterize the resulting model based on the allowed complexity. In that scenario, AIC and MSE work as quality measures for the chosen model order. By applying this technique to mmWave vehicular channel data, I was able to show that the vehicular channel is inherently sparse if a smart basis is chosen. The sparsity appears when using the tapped delay line basis. However, after introducing a cluster-based basis, this sparsity is much more pronounced. These results are linked to the fact that the cluster basis reduces the spatial resolution to the size of vehicles. Hence, one vehicle customarily only appears as one tap. As the cluster basis operates by fitting of parallel subbands, the approach is especially tailored to implementation on emulators. If one is not interested in emulating the full measurement bandwidth, one only takes the solution for the subband of interest. Appendix A provides additional analysis from a 5.6 GHz measurement campaign, where similar sparsities to the mmWave channels are observed. Based on the observations in this thesis, the vehicular channel for the considered ad-hoc operation modes appears to be naturally sparse, as long as a sound basis is chosen. Furthermore, subband fitting proves to be a low complexity solution that readily improves the estimation quality. When analyzing the channel in the delay-Doppler domain, I was able to show that increasing the signal dimension enforces further relative sparsity. That is, the model order increases slower than the signal dimension. From a practical standpoint, delay-Doppler estimation increased the estimation SNR at the cost of time resolution. Hence, it is a viable option to estimate especially noisy estimates.

Die approbierte gedruckte Originalversion dieser Dissertation ist an der TU Wien Bibliothek verfügbar.
The approved original version of this doctoral thesis is available in print at TU Wien Bibliothek.
TU Bibliothek Your knowledge hub WIEN

3 Reduced Complexity Network Performance Modeling

The previous chapter analyzed vehicular channel representations. Now I use the results to evaluate vehicular communication performance. I do this for both the single link, as well a network of vehicles. First, in Section 3.1, I introduce my performance measures, which are based on error probabilities, as well as how to estimate them. Then, in Section 3.2 I use the channel emulator in combination with delay line channel models to measure performance benchmarks for single link communications. In Section 3.3, this is extended to a network. I use mobility simulations to obtain vehicle distributions in a traffic jam. These simulations provide more than 100 vehicles that are interconnected. In order to avoid connecting a full network of more than a hundred nodes, I present an algorithm that allows to simplify the network graph. The simplified network description can then be replicated on a small number of communication nodes, to obtain a performance estimate for the full network of nodes.

The single link analysis is chiefly based on [55], as well as [58]. The network analysis on the other hand is based on [56], which is based on [59].

3.1 Performance Modeling

In order to capture the essential aspects of reliable communications, The following question needs to be answered as reliably as possible. If a certain message is transmitted at a given time instance i, called $X[i]$, how likely is it that the transmission will be successful, an event I denote as $\mathscr{C}$, or that the transmission will be erroneous, which I denote as $\mathscr{E}$. Furthermore, what are the influences that shape the outcome, and how much do they influence the result. There are two aspects that generally influence the achievable performance. A single link is purely defined by the physical layer of the protocol and the wireless communication channel. This includes signal attenuation, Doppler spreading and time dispersion. If more than one node tries to communicate at a given time, MAC layer comes into play. This layer governs how channel access is handled, how the back-offs and delays work, and how much interference is to be expected. To provide a comprehensive performance model, both aspects have to be considered together. Conversely, not all effects of the channel or the network directly translate

Die approbierte gedruckte Originalversion dieser Dissertation ist an der TU Wien Bibliothek verfügbar.
The approved original version of this doctoral thesis is available in print at TU Wien Bibliothek.
TU Bibliothek Your knowledge hub WIEN

to a change in observed performance. Therefore, the aim is to identify the essential aspects that do impact the models and resulting performance.

I consider one transmission to be one packet of data, which is sent in one MAC frame as defined by the IEEE 802.11p standard. This has the following consequences. A transmission is needs to include payload size and MCS to fully define one transmission. Furthermore, transmission errors are *erasures*. A packet that does not pass the Cyclic Redundancy Check (CRC) is discarded at MAC layer. Thus, no part of the transmission is usable at higher layers. The performance of the communication that is expected at time instance i is defined the instantaneous probability of error process $\Pr(\mathscr{E}[i])$. The momentary probability of an error occurring is defined by two influences.

I denote the sequence of physical channel aspects as $\mathscr{H}[i]$. This encompasses all aspects that define the layer one characteristics, such as MPCs, Line-of-Sight (LOS)-Non Line-of-Sight (NLOS) distinction, and Doppler speeds. I impose that this process is random, but follows the Markov property. That is, the future of the sequence is only dependent on the current state. Similarly, I define $\mathscr{N}[i]$ the sequence that captures all, layer two influences. For this too, I assume the Markov property. In this thesis, I assume that the error probability is fully defined if those two quantities are known in it's entirety

$$\Pr(\mathscr{E}[i]) = \Pr\big(X[i] = \mathscr{E}|\mathscr{H}[i], \mathscr{N}[i]\big). \tag{3.1}$$

Note that $\mathscr{E}$ on the right-hand side is not dependent on the time instance anymore, as it is fully defined by the conditioning. This system level interpretation also means that effectively, there is no difference between different channel configurations, as long as they lead to the same error probability. Hence, two channels $\mathscr{H}[i]$ and $\mathscr{H}'[i]$ are considered to be *equivalent* if they lead to the same $\Pr(\mathscr{E}[i])$, that is if

$$\Pr\big(\mathscr{E}|\mathscr{H}[i], \mathscr{N}[i]\big) = \Pr\big(\mathscr{E}\big|\mathscr{H}'[i], \mathscr{N}[i]\big). \tag{3.2}$$

Similarly, I also consider two network topologies *equivalent* if both lead to the same performance process. Therefore, potentially complex channel or network descriptions is replaced with simpler channels leading to the same error probabilities.

3.1.1 Decomposition of the Packet Error Probability

A packet error can happen either due to the channel, or the network influences. If at least one of those provide unfavorable conditions, the packet is lost. Thus, I introduce an equivalent description of the channel, that separates the two influences into distinct probability descriptions. Then, the probability in Eq. (3.1) is decomposed into

$$\Pr(\mathscr{E}[i]) = 1 - \big(1 - \Pr(\mathscr{E}|\mathscr{H}[i])\big)\big(1 - \Pr(\mathscr{E}|\mathscr{N}[i])\big). \tag{3.3}$$

Die approbierte gedruckte Originalversion dieser Dissertation ist an der TU Wien Bibliothek verfügbar.
The approved original version of this doctoral thesis is available in print at TU Wien Bibliothek.
TU Bibliothek Your knowledge hub WIEN

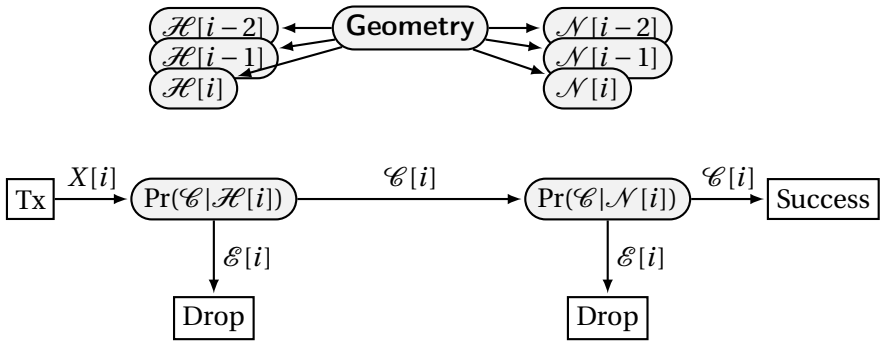

Figure 3.1: Final description of the communication decomposition.

This does not mean that $\mathscr{H}[i,i-1,\ldots]$ and $\mathscr{N}[i,i-1,\ldots]$ aren't statistically dependent of each other. Instead, this reflects the fact that one of the two influences being in a bad state is sufficient to lose the packet.

Equation (3.3) is more elegantly written in terms of success probabilities, given as

$$\Pr(\mathscr{C}[i]) = \Pr\left(\mathscr{C}|\mathscr{H}[i]\right)\Pr\left(\mathscr{C}|\mathscr{N}[i]\right). \tag{3.4}$$

The process is also demonstrated in Fig. 3.1. Finally, I want to characterize the burstiness of the system. Specifically, the interest lies in the probability of the same type of event occurring again right after it occurred. Thus, I introduce the conditional probabilities $\Pr(\mathscr{E}_i|\mathscr{E}_{i-1})[i]$ and $\Pr(\mathscr{C}_i|\mathscr{C}_{i-1})[i]$[1]. These two parameters are not providing full probabilistic description of the burst properties, but they provide interesting insights. $\Pr(\mathscr{E})$ does not convey how strongly grouped the errors occur. $\Pr(\mathscr{E}_i|\mathscr{E}_{i-1})$ on the other hand, achieves this. If a transmission is full of long error bursts ($N > 100$), $\Pr(\mathscr{E}_i|\mathscr{E}_{i-1})$ is close to 1 as almost all errors is followed by another error. This is even true if $\Pr(\mathscr{E})$ is very low. Conversely, if there is no burst behavior, the channel is memoryless and $\Pr(\mathscr{E}_i|\mathscr{E}_{i-1})$ is close to $\Pr(\mathscr{E})$. Conditioning on prior events won't change anything. The same holds true for $\Pr(\mathscr{C})$ and $\Pr(\mathscr{C}_i|\mathscr{C}_{i-1})$.

3.1.2 Estimating the Packet Error

I now introduce a formal description of how to estimate the packet error probability, and what assumptions are required. Generally speaking, if multiple realizations of the same processes $\mathscr{H}[i]$ and $\mathscr{N}[i]$ are available, then the estimate for the packet error at instant i becomes

$$\widehat{\Pr}(\mathscr{E})[i] = \frac{\text{Occurences of } \mathscr{E} \text{ given } \mathscr{H}[i],\mathscr{N}[i]}{\text{Number of realizations}}. \tag{3.5}$$

[1] Due to the notation complexity, I use the subscript style here

Die approbierte gedruckte Originalversion dieser Dissertation ist an der TU Wien Bibliothek verfügbar.
The approved original version of this doctoral thesis is available in print at TU Wien Bibliothek.

Since it is impossible to obtain multiple realizations of the same random process, unless ergodicity can be assumed, I also introduce the Packet Error Rate (PER) estimate as

$$\widehat{\mathrm{PER}}_w[i] = \frac{\text{Occurences of } \mathscr{E} \text{ in window of size } w}{\text{Number of events in window of size } w}. \tag{3.6}$$

Here, w is a window duration over which the estimate is calculated. Long window times tend to smooth out quick trends, while short window times provide inferior estimates due to the low number of events. The second estimate converges towards the first estimate for larger window durations if and only if the underlying stochastic processes are stationary. If stationarity can be assumed in the analysis, I drop the w subscript and simply write $\widehat{\mathrm{PER}}$. I now extend the previous estimates by introducing estimates for the burst qualities of the channel. Analogous to Eq. (3.1), the estimates become

$$\widehat{\Pr}(\mathscr{E}_i|\mathscr{E}_{i-1})[i] = \frac{\text{Occurences of } \mathscr{E} \text{ given } \mathscr{H}[i], \mathscr{N}[i], \mathscr{E}[i-1]}{\text{Number of realizations with an error occurring prior}}, \tag{3.7}$$

$$\widehat{\Pr}(\mathscr{C}_i|\mathscr{C}_{i-1})[i] = \frac{\text{Occurences of } \mathscr{C} \text{ given } \mathscr{H}[i], \mathscr{N}[i], \mathscr{C}[i-1]}{\text{Number of realizations with an success occurring prior}}. \tag{3.8}$$

If both channel properties and network topology can be shown to be stationary, these estimates becomes independent of time.

3.2 Single Link Performance Evaluations

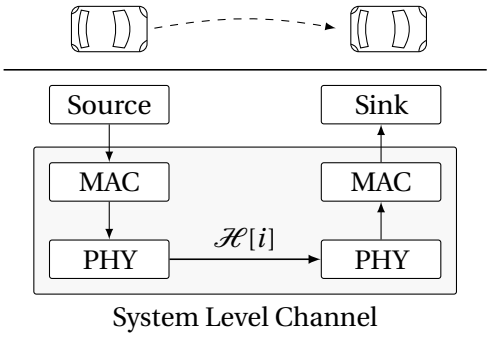

Figure 3.2: System Level Model for the Single Link Channel.

The single link evaluation focuses on the scenario given in Fig. 3.2. One IEEE 802.11p compliant source transmits data over an emulated channel to a receiver. I first present an insight into the hardware setup used for this evaluation. Then, I explain the channels that are tested. These comprise the 5.6 GHz channel data that is presented in Appendix A. Additionally, five stationary channel models are considered that are proposed by ETSI for the ITS-G5 standard [58].

Die approbierte gedruckte Originalversion dieser Dissertation ist an der TU Wien Bibliothek verfügbar.
The approved original version of this doctoral thesis is available in print at TU Wien Bibliothek.
TU Bibliothek Your knowledge hub WIEN

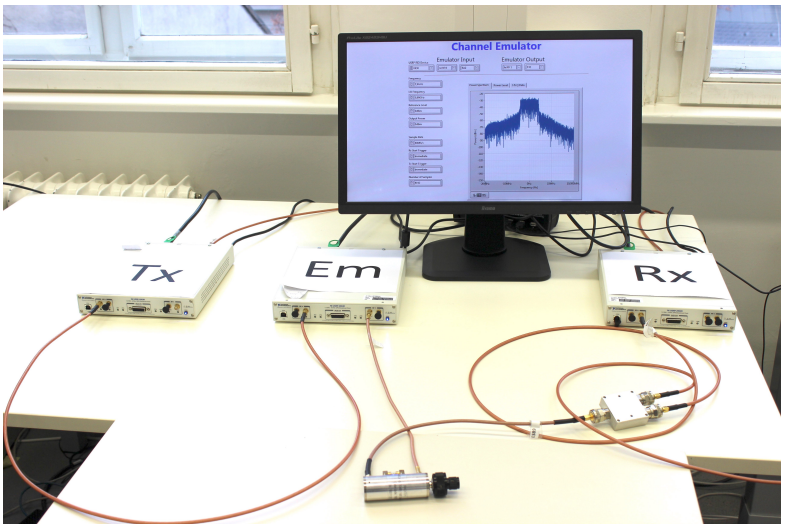

Figure 3.3: Testbed setup: Transmitter (Tx), vehicular channel emulator (Em), stepped attenuator, and receiver (Rx) wired by RF coaxial cables.

3.2.1 Emulator Testbed

Two Software Defined Radio (SDR) based 802.11p modems configured as the TX and the RX are connected as described in Fig. 3.3 to the SDR emulator (Em), which is a National Instruments (NI) Universal Software Radio Peripheral (USRP)-2953R. Between the Em and the Rx, a RADITEK RVATTN-DC-6 (0-70 dB) step attenuator is inserted. When the channel emulator is ready, the TX modem starts sending the specified number of packets with specified payload. At the RX, the number of successfully received packets are logged. The 10 s measurement is converted to a suitable trace beforehand, and forwarded to the emulator via the host PC. The trace is looped, and the measurement is run for a total of 10 minutes. A transmission is attempted every 1 ms, and the payload contains a identification number and random data to fill the packet length to the desired length. Based on these identification numbers, I estimate the packet error estimates defined previously.

3.2.2 Channel Models and Parameter Settings

Nonstationary Measurement Playback

In this section, I present the test carried out to benchmark the performance of two SDR-based IEEE 802.11p modems connected to an emulator which is emulating the non-stationary fading model presented in [51]. The chosen model relates to the vehicular scenario: *Road crossing: urban single lane* with measured data collected in DRIVEWAY'09 V2V measurement campaign in Lund, Sweden [84]. The duration of the measured scenario is 10 s. As depicted in the general schematics of the scenario in Fig. 3.4, the TX and the RX drive towards one another in two perpendicular streets, they reach one another at the intersection, and then they drive away.

Die approbierte gedruckte Originalversion dieser Dissertation ist an der TU Wien Bibliothek verfügbar.
The approved original version of this doctoral thesis is available in print at TU Wien Bibliothek.
TU Bibliothek Your knowledge hub WIEN

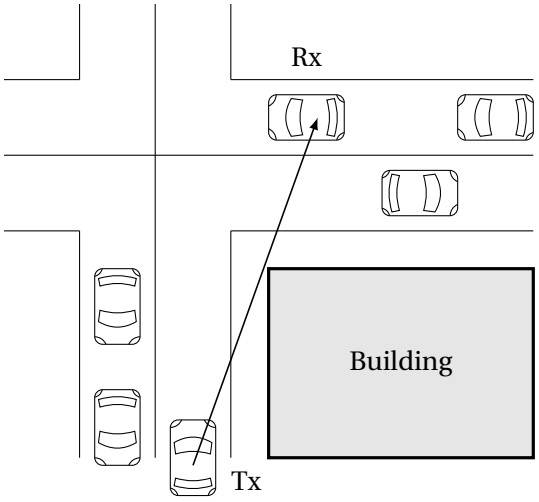

Figure 3.4: Urban crossing channel scenario.

The PDP recorded by the measurement campaign is shown in Fig. 3.5a plotted over measurement time. In the beginning of the scenario the only MPC the NLOS components reflected from the buildings at two sides of the roads. As the cars approach the road crossing, the LOS component appears [51]. The specific scenario is of particular interest, since not only, similar to other vehicular scenarios, large Doppler and delay spreads are observed. Furthermore, the abrupt change from NLOS components as the dominant paths to the LOS component along with the change in the direction of Doppler frequency prove interesting. I use a special application of the subband cluster estimation from Section 2.3.2 to estimate a sparse fit for this measurement. The subbands are set to be 20 MHz bands, and only use the subband delay line from one of them. Since the communication system of interest only uses 10 MHz of bandwidth, I am covering the frequency of interest, but still increase the fitting quality when compared to a pure tapped delay line fit. the result is shown in Fig. 3.5b. Further sparsity analysis of this measurement run is shown in Appendix A. The trace samples including delays, pathloss and phase shifts are updated every 302.7 μs.

Stationary Channel Models

The second goal is to step from playback of measured scenarios to the implementation of standardized scenarios. This is done based on stationary vehicular channel models that were defined in a draft by ETSI specifically with the application in benchmarking in mind. The given models from [58] are summarized in Table 3.1, and encompass 5 typical vehicular scenarios. The models are also based on the tapped delay line, and follow the general structure of

$$g(\tau,t)=\sum_{p=1}^{4}10^{\frac{\eta_p}{20}}\delta(t-\tau_p)g_p(t). \tag{3.9}$$

Die approbierte gedruckte Originalversion dieser Dissertation ist an der TU Wien Bibliothek verfügbar.
The approved original version of this doctoral thesis is available in print at TU Wien Bibliothek.

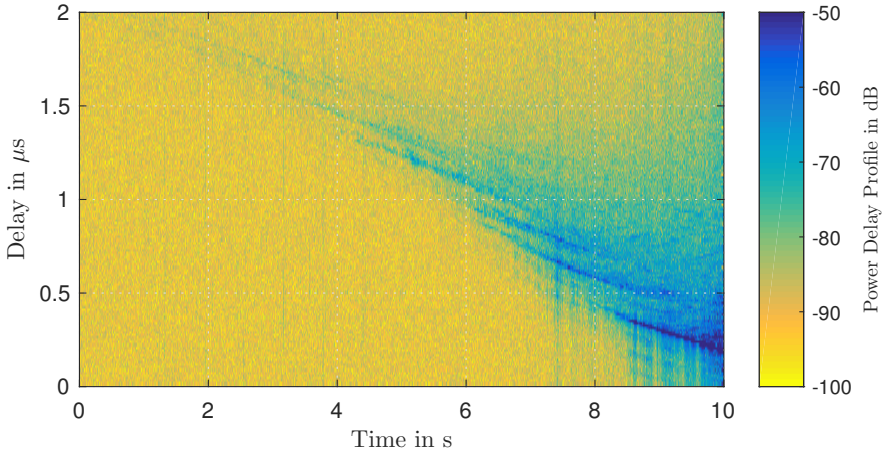

(a) Time-variant PDP of measured channel in urban crossing scenario.

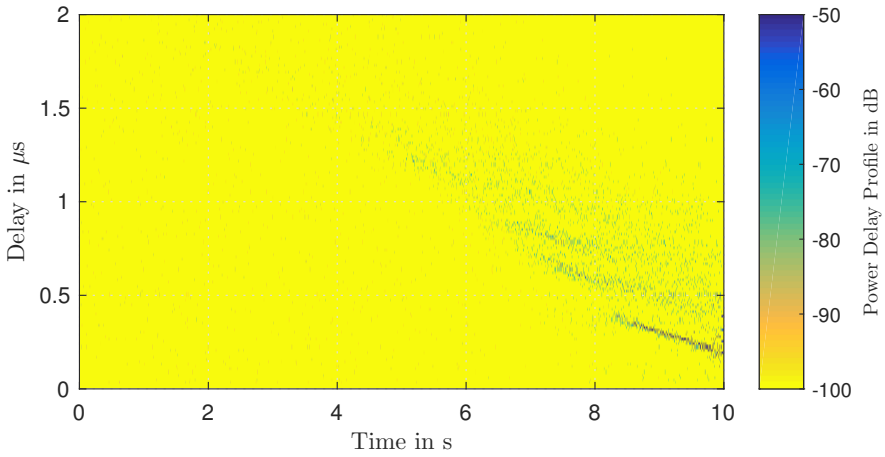

(b) 10-tap fit of the given PDP.

Figure 3.5: Measured PDP and 10-tap LASSO fit (c.f. [51]).

Die approbierte gedruckte Originalversion dieser Dissertation ist an der TU Wien Bibliothek verfügbar.
The approved original version of this doctoral thesis is available in print at TU Wien Bibliothek.

The tap parameters $g_p(t)$ follow *Half-Bathtub* Jakes' Spectra. This means that only one half of the typical Jakes' spectrum is nonzero [58]. This is shown in Fig. 3.6, where the half-bathtub variants are raised by 3 dB to conserve the total signal energy. Thus, the maximum Doppler shift ν_p has a sign that denotes whether the left or the right side of the spectrum is nonzero. Details on the generation of these small-scale fading traces is given in Appendix C.1.

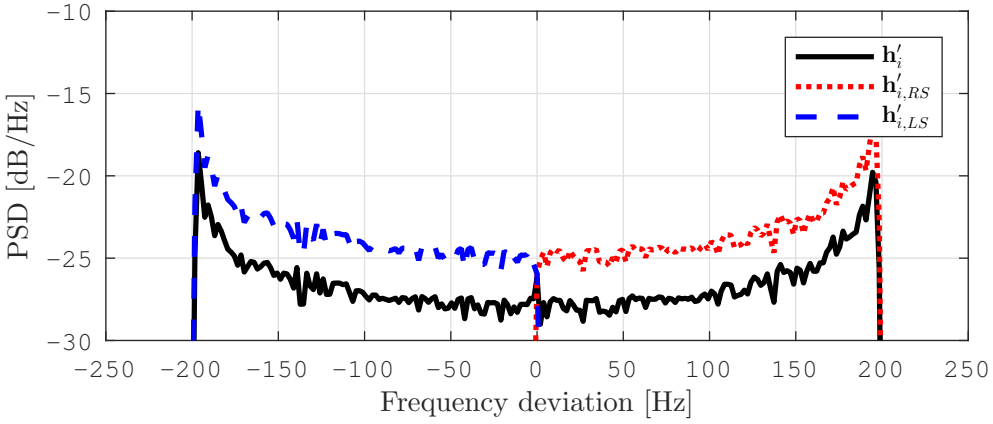

Figure 3.6: Power Spectral Density (PSD) of an original Jakes' trace, and the right and left sided versions. The simulation is done at 5.9 GHz, and the maximum relative velocity is 10 m/s.

Rural traffic is designed as similar to Additive White Gaussian Noise (AWGN),in so far as only weak stochastic MPCs are added. Furthermore, there are the 2 critical areas for vehicular traffic, urban and highways. The urban models show strong multipath components, while the highway models generally have large Doppler spreads. Each model is presented by means of a tapped-delay line with 3 or 4 active taps. The first tap is defined as static with delay zero and zero Doppler frequency to serve as normalization reference; the remaining taps are considered to be Rayleigh distributed: each is represented with its delay τ_p, with η_p and ν_p as deterministic pathloss and maximal Doppler shift of the Doppler spectrum respectively along with a spectral shape of the PSD. To prepare the channel trace, the delay values are quantized to the sampling time of the USRP and determined the active taps. The stochastic trace for the Rayleigh fading is generated form a Half Jakes' PSD with sampling period of 100 μs [58]. The Half-Bathtub sequence was formed by generating a typical Jake's Bath tub sequence with maximum Doppler frequency and then setting one half of Doppler spectrum to zero according to the sign of the Doppler frequency.

3.2.3 Results

Figure 3.7 shows the results of the measurements conducted on the nonstationary model. PER evaluations are shown in Figs. 3.7a, 3.7c and 3.7e and depict PER curves for 6 realizations of the 10 second trace. I calculated them by setting the window length to 200 ms, and generating a sliding average. Since the channel repeats 60 times in 10 minutes, I show this sliding average for 6 channel realizations spread out over the measurement time. I want to point out that

Die approbierte gedruckte Originalversion dieser Dissertation ist an der TU Wien Bibliothek verfügbar.
The approved original version of this doctoral thesis is available in print at TU Wien Bibliothek.
TU Bibliothek Your knowledge hub WIEN

Table 3.1: ETSI draft channel model parameters.

Draft Scenarios	Tap	η_p[dB]	τ_p[ns]	$\nu_p[Hz]$	Spectral shape
Rural LOS	$p=1$	0	0	0	Static
	$p=2$	−14	83	492	HalfBT
	$p=3$	−17	183	−295	HalfBT
Urban LOS	$p=1$	0	0	0	Static
	$p=2$	−3	267	295	HalfBT
	$p=3$	−4	400	−98	HalfBT
	$p=4$	−10	533	591	HalfBT
Urban NLOS	$p=1$	0	0	0	Static
	$p=2$	−8	117	236	HalfBT
	$p=3$	−10	183	−157	HalfBT
	$p=4$	−15	333	492	HalfBT
Highway LOS	$p=1$	0	0	0	Static
	$p=2$	−10	100	689	HalfBT
	$p=3$	−15	167	−492	HalfBT
	$p=4$	−20	500	886	HalfBT
Highway NLOS	$p=1$	0	0	0	Static
	$p=2$	−2	200	689	HalfBT
	$p=3$	−5	433	−492	HalfBT
	$p=4$	−7	700	886	HalfBT

this is not generated by triggering the channel, I only used the timestamp at transmitter and receiver for aligning the measurement traces. This demonstrates that the emulation timing corresponds to real-world timing and remains stable over 10 minutes of measurement time. Furthermore, the generated PER curves show very small deviations between realizations. This is expected, as the measurements are conducted at high received powers and consequently additive noise added after the emulator is not expected to contribute. Overall, the PER curves show that the emulator allows perfect repeatability of tests due to the stability of behavior between channel realizations. With this result, I concentrate on Figs. 3.7b, 3.7d and 3.7f. There, I calculate Pr($\mathscr{E}$) through *ensemble means*. Since the PER analysis shows that the emulator repeats the channel trace at exactly 10 s, I calculate Pr($\mathscr{E}$) by averaging over all events that are separated exactly 10 s, and do this for all offsets. The graph shows that the ensemble mean follows the trend of the PER, but shows more details. For example, at 8.5 s, a short dip in Pr($\mathscr{E}$) is shown that is so short that it is averaged out in the PER graph. Thus, a PER estimate is calculated, and also demonstrate that the PER is a good first estimate, however, when treating nonstationary scenarios, it misses fast changes and Pr($\mathscr{E}$) has to be used.

Overall, the performance in the nonstationary case is divided into 3 regions. For the first 6 – 7 s, the small channel values dominate, and no packet passes successfully. Then, the results show an almost binary in dependence on the LOS path. At the instant in Fig. 3.5a where the LOS

Die approbierte gedruckte Originalversion dieser Dissertation ist an der TU Wien Bibliothek verfügbar.
The approved original version of this doctoral thesis is available in print at TU Wien Bibliothek.
TU Bibliothek Your knowledge hub WIEN

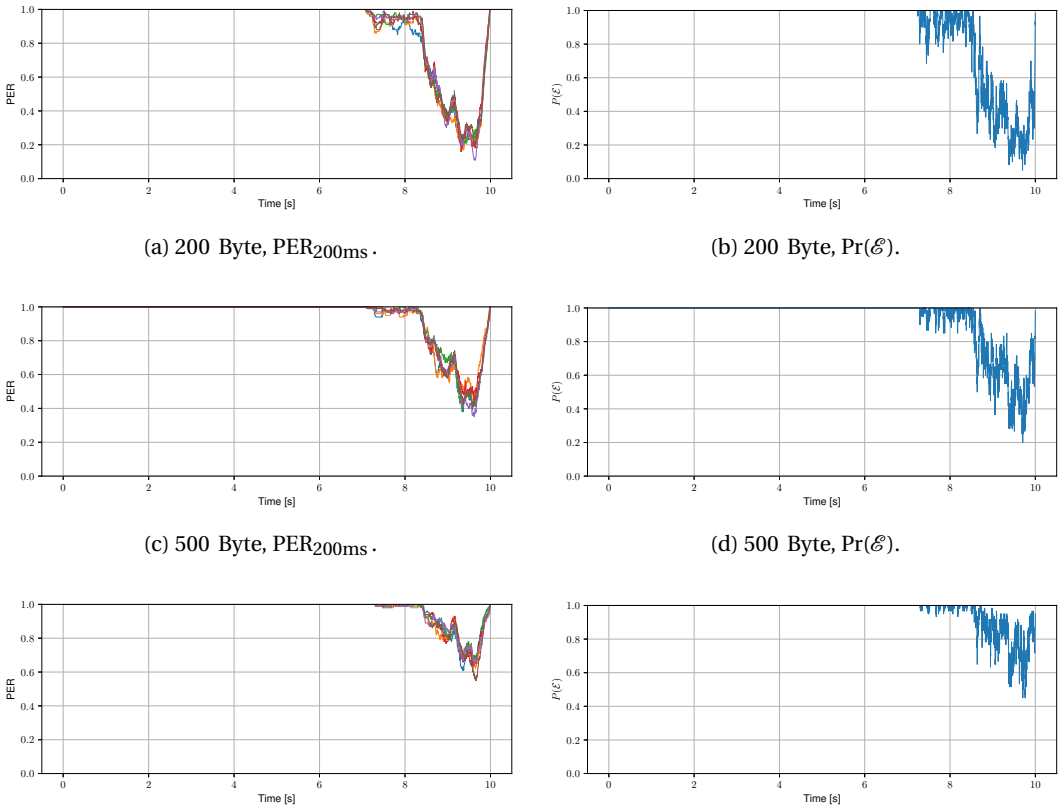

(a) 200 Byte, $\mathrm{PER}_{200\mathrm{ms}}$.

(b) 200 Byte, $\Pr(\mathscr{E})$.

(c) 500 Byte, $\mathrm{PER}_{200\mathrm{ms}}$.

(d) 500 Byte, $\Pr(\mathscr{E})$.

(e) 1000 Byte, $\mathrm{PER}_{200\mathrm{ms}}$.

(f) 1000 Byte, $\Pr(\mathscr{E})$.

Figure 3.7: Packet error ratio (left) and packet error probability (right) estimates from emulated nonstationary vehicular channel.

path appears, the packet error probability drops from close to 1 strongly, depending on the packet length. In general, for all packet lengths the same qualitative behavior is observed, even if the exact values differ. Therefore, for further measurements, I consider 500 Byte as packet size.

Die approbierte gedruckte Originalversion dieser Dissertation ist an der TU Wien Bibliothek verfügbar.
The approved original version of this doctoral thesis is available in print at TU Wien Bibliothek.
TU Bibliothek Your knowledge hub WIEN

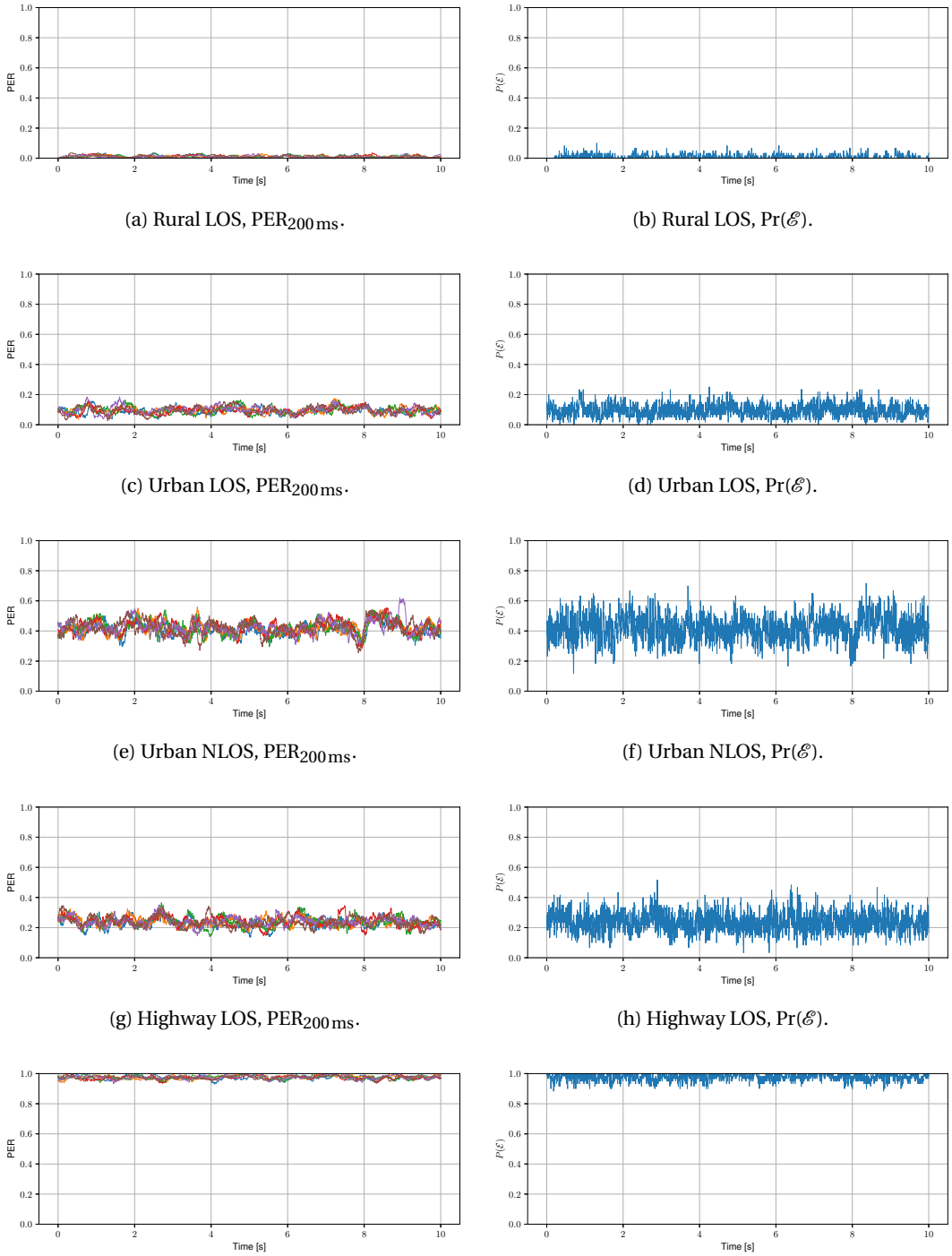

(a) Rural LOS, $\text{PER}_{200\,\text{ms}}$.

(b) Rural LOS, $\Pr(\mathcal{E})$.

(c) Urban LOS, $\text{PER}_{200\,\text{ms}}$.

(d) Urban LOS, $\Pr(\mathcal{E})$.

(e) Urban NLOS, $\text{PER}_{200\,\text{ms}}$.

(f) Urban NLOS, $\Pr(\mathcal{E})$.

(g) Highway LOS, $\text{PER}_{200\,\text{ms}}$.

(h) Highway LOS, $\Pr(\mathcal{E})$.

(i) Highway NLOS, $\text{PER}_{200\,\text{ms}}$.

(j) Highway NLOS, $\Pr(\mathcal{E})$.

Figure 3.8: PER (left) and packet error probability (right) estimates from emulated stationary vehicular channel.

Die approbierte gedruckte Originalversion dieser Dissertation ist an der TU Wien Bibliothek verfügbar.
The approved original version of this doctoral thesis is available in print at TU Wien Bibliothek.

The results of the stationary measurements are shown in Fig. 3.8. Figures 3.8a, 3.8c, 3.8e, 3.8g and 3.8i show the 200 ms-PER averages. In the stationary case, these vary around a constant value. The observed variation is due to the fact that the averaging window is short enough to still let the small-scale fading variations be visible. They are seen strongest in the Urban NLOS case, which has strong multipath components, and long correlation times due to low Doppler speeds. Again, the overlaid traces show that it is possible to provide a repeatable channel with repeatable characteristics. As shown in [58], Rural LOS corresponds to almost perfect transmission, and Highway NLOS to a $\Pr(\mathscr{E})$ of almost 1. Switching to Figs. 3.8b, 3.8d, 3.8f, 3.8h and 3.8j, I calculate the $\Pr(\mathscr{E})$ estimates again. The stationary results confirm the nonstationary results, as the actual $\Pr(\mathscr{E})$ shows more pronounced short-term variations that are averaged out in the PER calculation. The results show that the fading impact is shown in the variation of the packet error probability, and mustn't be neglected a priori. However, disregarding this aspect, the measurements demonstrate an important property. In the stationary case, the averaging window for the PER may be arbitrarily large since the statistics don't change. If w goes to infinity however, PER_w and $\Pr(\mathscr{E})$ averaged over w will converge to the same value, since even for 10 s traces, their shapes are very similar. Thus, if one is only interested in a global error probability in a single value, the PER is calculated directly using a single, sufficiently long realization, without resorting to analysis of the ensemble means. While this result is trivial for stationary channels in theory, it is important that the hardware implementation on the emulator actually follows this and behaves as expected. Therefore, modems can be benchmarked via calculating the PER, which means one only needs access to the total number of transmissions and receptions.

Measurement parameter	Value
Frequency channel	180 (5.9 GHz)
Packet length	200, 500, 1000 Bytes
Measurement Duration	10 min
Average RX power	−65 dBm
Power level at channel emulator input	−30 dBm
Data rate	6 Mbps
Baseband modulation	QPSK
Coding rate	1/2

Table 3.2: Measurement setup parameters for nonstationary model test.

3.2.4 Mean and Burst Small-Scale Fading Behavior

Here, I consider the stationary models, which are purely small-scale fading models, in dependence of the SNR. The results, measured for 100 and 500 byte packets, are shown in Fig. 3.9. In green, I show the measurement sensitivity, which is defined as the value at which the throughput reaches at least 90 % in the AWGN scenario. Furthermore, The plots do not only depict $\Pr(\mathscr{E})$, but also $\Pr(\mathscr{E}_i|\mathscr{C}_{i-1})$. This was chosen instead of $\Pr(\mathscr{E}_i|\mathscr{E}_{i-1})$, as it provides more

Die approbierte gedruckte Originalversion dieser Dissertation ist an der TU Wien Bibliothek verfügbar.
The approved original version of this doctoral thesis is available in print at TU Wien Bibliothek.
TU Bibliothek Your knowledge hub WIEN

obvious results, and the two quantities relate directly via the total probability theorem. The results show that channels with dominant multipaths (the NLOS scenarios such as *urban crossing*) see some bursty behavior. The highway models on the other hand see negligible burst behavior. Capturing this burst behavior is especially relevant when the dominant non-static contribution has a low maximum Doppler frequency. This is true even more so if the dominant non-static component is strong, i.e. a NLOS like scenario is active.

Die approbierte gedruckte Originalversion dieser Dissertation ist an der TU Wien Bibliothek verfügbar.
The approved original version of this doctoral thesis is available in print at TU Wien Bibliothek.
TU Bibliothek Your knowledge hub WIEN

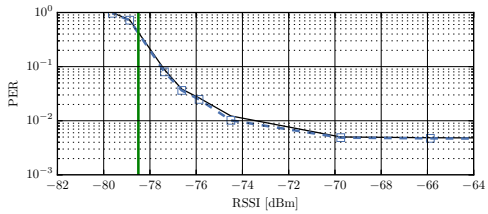

(a) Rural LOS, 500 Bytes.

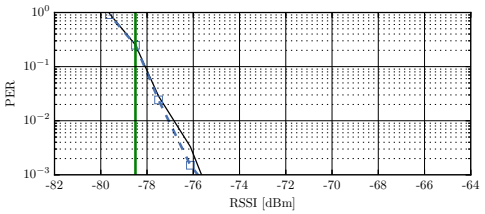

(b) Rural LOS, 100 Bytes.

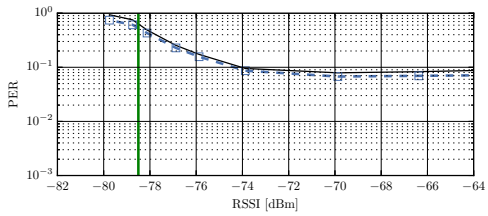

(c) Urban Approaching, 500 Bytes.

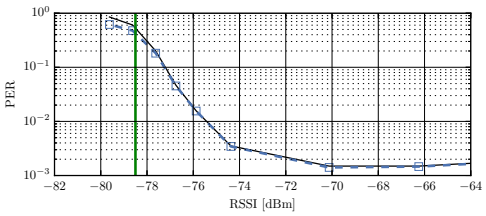

(d) Urban Approaching, 100 Bytes.

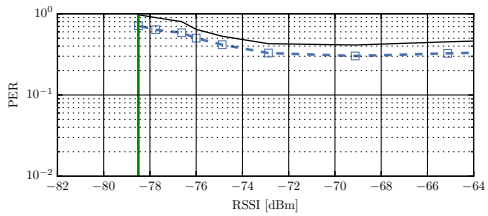

(e) Urban Crossing, 500 Bytes.

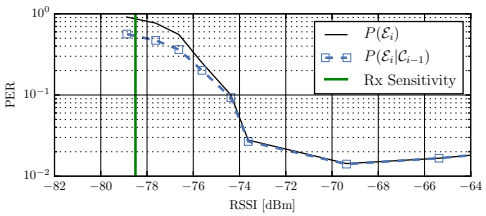

(f) Urban Crossing, 100 Bytes.

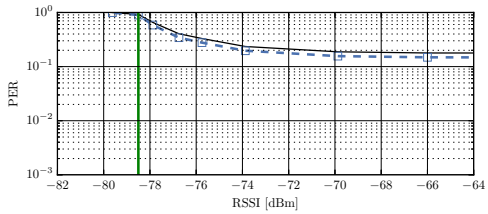

(g) Highway LOS, 500 Bytes.

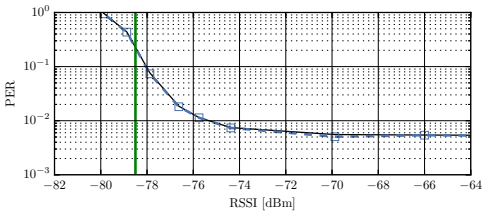

(h) Highway LOS, 100 Bytes.

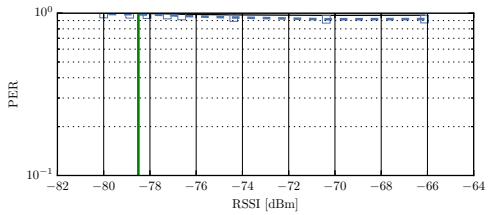

(i) Highway NLOS, 500 Bytes.

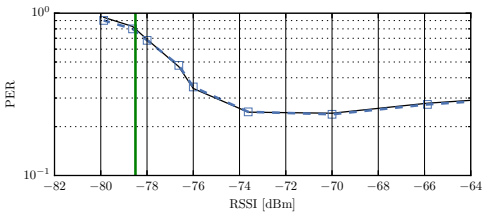

(j) Highway NLOS, 100 Bytes.

Figure 3.9: Mean and burst behavior for 500 and 100 Bytes packet size.

Die approbierte gedruckte Originalversion dieser Dissertation ist an der TU Wien Bibliothek verfügbar.
The approved original version of this doctoral thesis is available in print at TU Wien Bibliothek.
TU Bibliothek Your knowledge hub WIEN

3.3 Network Performance Analysis

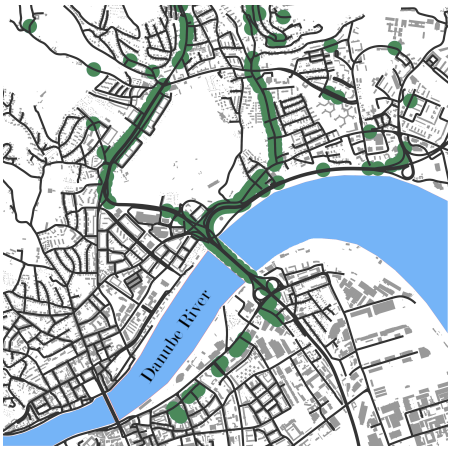

Figure 3.10: Traffic congestion. in Linz, Austria. Green dots are vehicles traveling from north to south, simulation results from [85].

In this section, I describe how I extend the single link evaluation to a network of nodes. Then, in Section 3.4, I present performance analyses based on this modeling. The goal is to include the influence of the network into the evaluation. To achieve this, a model for vehicle movements is required, as well as for the interfering transmission events. This model is allowed simplifications, as long as the resulting model is representative of the original scenario. Figure 3.10 shows an exemplary simulation result for vehicle movement in the city of Linz, Austria. In a scenario like this, vehicles are distributed very unevenly across main streets and side streets, and thus simple homogeneous stochastic assumptions fail to model the resulting geometric distributions. Here, I use the mobility simulator TraffSim [86] to generate representative vehicular traces. In Section 3.3.1, I briefly outline the simulation setup for this mobility simulator.

3.3.1 Mobility Simulations: TraffSim

Mobility simulations are generally split into two categories. Macroscopic simulations consider whole flows of vehicles at a time with models from fluid dynamics. These models work well when analyzing very large networks, and average speeds and distributions, but they do not provide geometric data for the single vehicles. Microscopic simulators on the other hand use models for the movements and interactions of the individual vehicles [87], which is what is of interest in this thesis. I use the microscopic traffic simulator TraffSim [86] in order to carry out the simulations which provide the trajectories for the results that are analyzed. The investigated scenario and simulation configuration is equal to the setup in [85], which represents an extract of the city of Linz in Austria. I apply the well-known Intelligent Driver Model (IDM) as longitudinal model and use unregulated intersections [88] to avoid any influence of dynamic intersection regulation algorithms. The vehicles starts and destinations are defined to be uniformly distributed within a certain area. Specifically, the simulation

Die approbierte gedruckte Originalversion dieser Dissertation ist an der TU Wien Bibliothek verfügbar.
The approved original version of this doctoral thesis is available in print at TU Wien Bibliothek.
TU Bibliothek Your knowledge hub WIEN

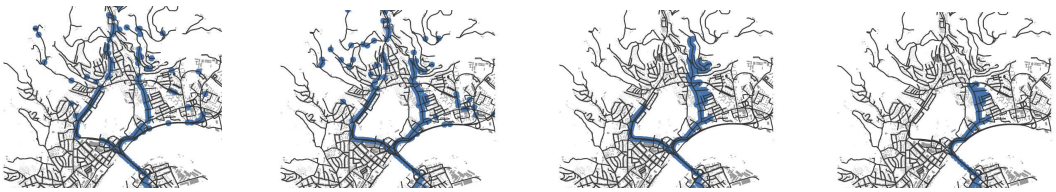

(a) 2000 s (b) 5000 s (c) 8000 s (d) 11000 s

Figure 3.11: Four snapshots at different simulation times of the traffic flow simulation. The blue dots show vehicle positions at the given snapshots.

defines the commuter traffic from the north of the river Danube coming to the south. The vehicle density, which is influenced by the inter-arrival interval between two vehicles is parameterized identically as well. It is chosen to be 2500 ms for both configurations, and a total of 3000 vehicles are placed. The provided configuration represents an *unrouted* situation, where each vehicle chooses its potentially fastest route individually and does not consider any other drivers. In this configuration, no single driver can change its route during simulation. This egoistic behavior leads to congestion, as is shown in the snapshot in Fig. 3.11.

3.3.2 Connectivity Modeling Approach

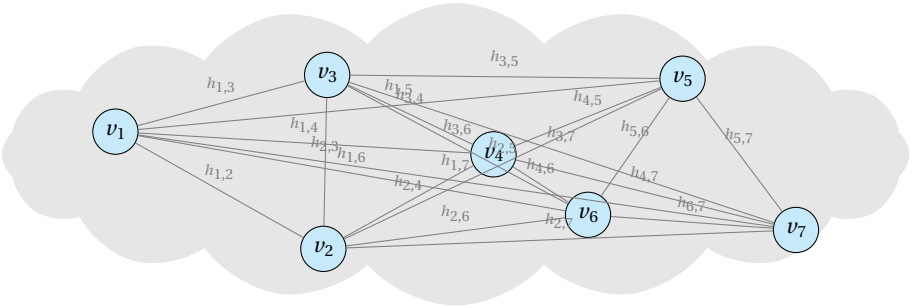

(a) Physical Network

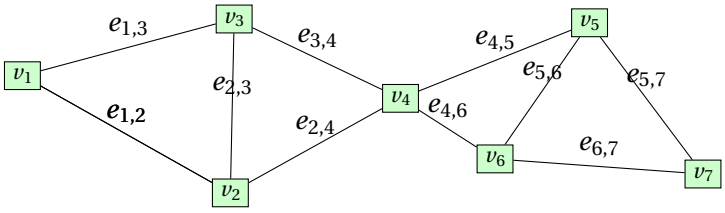

(b) MAC Layer Abstraction

Figure 3.12: Representation of a physical scenario with seven nodes (a), as well as a MAC layer abstraction of the same scenario (b).

The aim is to model a large network of vehicles, for example, the scenario shown in Fig. 3.11. I assume these vehicles to be equipped with means for ad-hoc communications. Such a scenario, in general, has to be modeled like the network shown in Fig. 3.12. Here, there are N nodes, and a total of $\frac{N(N-1)}{2}$ possible communication channels $h_{i,j}$. These channels are, due

Die approbierte gedruckte Originalversion dieser Dissertation ist an der TU Wien Bibliothek verfügbar.
The approved original version of this doctoral thesis is available in print at TU Wien Bibliothek.
TU Bibliothek Your knowledge hub WIEN

to multipath propagation and mobility of the nodes doubly selective $h_{i,j}(t,\tau)$. I do however assume reciprocity, hence $h_{i,j} = h_{j,i}$.

For large networks, this model becomes unwieldy and computationally prohibitively expensive. Even when using only a 4-tap delay line as channel model, 40000 multiplications and additions have to be computed for a single link for 1 packet of 500 byte length [60]. This number grows quadratically with the number of nodes in the network. Therefore, abstractions are introduced to keep computational complexity low.

The first step to introducing these abstractions is to formulate the communication as a general communication graph, as seen in the MAC layer abstraction Fig. 3.12. Here, I represent the vehicles as nodes v_i, and model connections between the nodes as edges $e_{i,j}$. While these edges are linked to communication channels, they incorporate abstractions that is detailed in the subsequent sections. By taking the set of all vehicles $V = \{v_1, v_2, \ldots, v_N\}$ and the set of all edges $E = \{e_{1,2}, e_{1,3} \ldots e_{N-1,N}\}$ I construct the general communication graph [57]

$$G = (V, E). \tag{3.10}$$

When modeling the physical network (Fig. 3.12 (a)), V is the set of all vehicles $V = \{v_1, \ldots, v_N\}$. In this case, the graph is a complete graph, thus the edge set is given as $E = \{h_{i,j} | \forall i, j \in (1, \ldots, N) \times (1, \ldots, N), i \neq j\}$. I call this the physical graph G_P. Based on this, I look for graph abstractions for the considered communication system. The vertices and edges of this graph depend strongly on the underlying protocol.

3.3.3 Physical Parameters and Medium Access Control

802.11p *senses* whether someone else is transmitting through the Clear Channel Assessment (CCA). Here, the sensed received power is compared to a threshold, and if the CCA remains below this threshold, the channel is deemed empty. Then, I define that an edge is added to the edge set according to

$$e_{i,j} \in E' \equiv PL(v_i, v_j) < P_{\mathrm{Tx}} - \mathrm{CCA}. \tag{3.11}$$

Given this new edge set E' I build the new communication graph G as edge-induced subgraph of the physical graph

$$G = G_P[E']. \tag{3.12}$$

For the parameters, the edge is in the set if and only if the pathloss from v_i to v_j is less than 90 dB. This edge does not imply that a transmitted packet is received correctly. Instead, the edge is an important indicator for the MAC scheme. Following [56], I assume a pathloss model according to [30], which result in an effective sensing range of 324 m.

Die approbierte gedruckte Originalversion dieser Dissertation ist an der TU Wien Bibliothek verfügbar.
The approved original version of this doctoral thesis is available in print at TU Wien Bibliothek.
TU Bibliothek Your knowledge hub WIEN

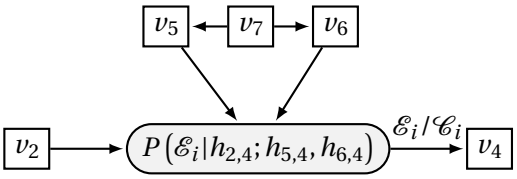

(a) Channel performance model of the original setup.

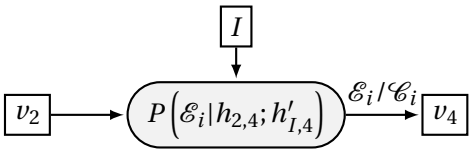

(b) Alternative, representative setup.

Figure 3.13: Two possible channel performance models representing the scenario in Fig. 3.12.

For the MAC, IEEE 802.11p uses CSMA/CA. Therefore, a node only transmits when it perceives the channel to be empty. Whenever two vehicles are within this sensing range of each other, they do not transmit simultaneously. Hence, two nodes will not interfere if and only if they are connected by an edge.

Finally, if, for a given subset of nodes V_{sub}, the condition is fulfilled that there is an edge between all nodes, i.e.,

$$v_i, v_j \in V_{\text{sub}} \Rightarrow e_{i,j} \in E \quad \forall (i,j), \tag{3.13}$$

then I call V_{sub} a *clique* C. In a clique, no hidden nodes exist, and only one node will transmit at any given time, discounting timing offsets.

3.3.4 Representative Channel Performance Model

On the MAC layer, the observed communication channel is defined by the observed packet error probability $\Pr(\mathscr{E})$. This packet error probability depends mainly on the physical channel of the link, the used standard, as well as the presence of interference. However, different scenarios, may lead to the same packet error performance, and are thus indistinguishable at MAC layer. For instance, the scenario in Fig. 3.12 is shown in Fig. 3.13a. Node v_2 transmits a packet to node v_4. Additionally, nodes v_5 and v_6 may choose to transmit and act as hidden nodes. Packet loss may occur due to the physical channel $h_{2,4}$ or the hidden node interference, which again depends on their communication channels. Therefore, the probability depends on 3 different channels, and sees packets incoming from 3 nodes. Finally, due to the MAC, the transmit timing of v_5 and v_6 depends also on v_7.

However, this channel can also be drawn as Fig. 3.13b. Here, only one interfering node I exists, with only one channel $h_{I,4}$. This node now represents the clique $I = \{v_5, v_6, v_7\}$. From this given clique, v_5 and v_6 are directly able to act as hidden nodes. Since only one of the nodes in

Die approbierte gedruckte Originalversion dieser Dissertation ist an der TU Wien Bibliothek verfügbar.
The approved original version of this doctoral thesis is available in print at TU Wien Bibliothek.
TU Bibliothek Your knowledge hub WIEN

the clique will transmit at any given time, a single node I can model the interference instead. In this example, node v_7 is also important to be included in a model. If this node transmits, the others won't, and thus, no hidden node transmission will occur from this clique. Crucially, if I model the transmission of v_7, but present it with a pathloss so large that the receiver does not sense the signal, I model it as part of the interfering clique without changing the received statistics.Hence, all members of cliques have to be considered if even one node of a clique may act as hidden node. Then, the channel $h'_{I,4}$ has to adapt to the conditions of the currently transmitting node. I achieve this by setting a dynamic pathloss for every packet that ensures hidden transmissions from very distant nodes are below noise level. As long as models **(a)** and **(b)** lead to the same $\Pr(\mathscr{E})$, they are interchangeable. Thus, **(b)** is *representative* for **(a)**. The goal in the following sections is to find a representative channel model for densely interfering channels that requires as little nodes as possible.

3.3.5 Graph Based Complexity Reduction

The goal now is to find a low complexity representative channel for the scenario described in the previous section. Considering an approach analogous to Fig. 3.13, I want to find a channel representation with as few nodes as possible, and a manageable complexity with regards to the involved communication channels. I approach this at two levels. First, I define an algorithm that approximates the communication graph by a graph of simpler structure. Then, I analyze the chosen channel model with respect to implementation properties.

3.3.6 MAC Level Approximation

On MAC level, the difficulty is that the communication graph in general is *connected*, that is, there is a path of edges from every node v_i to every node v_j. Thus, for every packet transmission, the full network has to be considered and modeled. On the other hand, as discussed, a clique C is flexible to model, because no matter how many nodes are in a clique C, only one will transmit at any given time. Therefore, a clique can always be modeled by 1 representative node. To achieve a simplified graph structure, I present an algorithm that iteratively constructs cliques, and removes unimportant edges, with the end result of having a strongly simplified structure while remaining representative for the original channel. I use 2 parameters as performance indicator for the algorithm:

1. The probability mass function (pmf) of simultaneously incoming packets.
2. The median channel access delay.

Criterion 1. Informs about how often hidden node interference happens, and how many hidden node packets arrive simultaneously across the whole simulation. Thus, I evaluate whether the overall number of interferers has been maintained through the approximation process. Criterion 2. on the other hand provides information on how busy the channel in the

Die approbierte gedruckte Originalversion dieser Dissertation ist an der TU Wien Bibliothek verfügbar.
The approved original version of this doctoral thesis is available in print at TU Wien Bibliothek.
TU Bibliothek Your knowledge hub WIEN

sensing range is. This is a measure for the number of communication neighbors has been maintained. The devised algorithm is presented in Algorithm 2. As input, it takes the original communication graph G_O constructed according to the listed conditions.

Algorithm 2 Clique Graph Approximation

```
1:  procedure APPROXIMATED GRAPH(Graph G_O)
2:      C ← maxcliques(G_O)
3:      while Overlap between cliques exists do
4:          for all {(i, j) | OL(c(i), c(j)) < t} do
5:              o ← c(i) ∩ c(j)              ▷ Calculate overlap between c(i), c(j)
6:              c(j) ← c(j) \ o              ▷ Remove overlap from smaller clique
7:          end for
8:          for all {(i, j) | OL(c(i), c(j)) ≥ t} do
9:              c(i) ← c(i) ∪ c(j)           ▷ Merge smaller into larger clique
10:             C ← C \ c(j)                 ▷ Remove smaller clique
11:         end for
12:     end while
13:     return constructgraph(C)
14: end procedure
```

The algorithm begins by finding all cliques of maximal size (a clique is of maximal size if no node $v_i \in V \setminus C$ can be added such that C remains a clique) [89]. These cliques generally overlap. For example, in the graph in Figure 3.12, both $c_1 = \{v_1, v_2, v_3\}$ and $c_2 = \{v_4, v_2, v_3\}$ are overlapping maximal cliques. The result is a *set* of maximal cliques C. Next, I calculate the Szymkiewicz-Simpson coefficient, also called overlap index [90]

$$OL(A,B) = \frac{|A \cap B|}{\min(|A|,|B|)}, \tag{3.14}$$

which measures how much of the smaller of two sets is also contained in the larger one. If two cliques are strongly overlapping, I merge them into one superclique without changing much about the overall statistics. Conversely, if they are very loosely overlapping, I separate them entirely to remove crosstalk, and still not change much about the transmission statistics. Therefore, starting from the largest clique that has an overlap with at least one other clique, this overlap index is evaluated. If this index is below a given threshold t, the overlap is removed to make the cliques disjoint (Algorithm 2, line 5 and 6). On the other hand, if the overlap is larger than t, the two cliques are merged into one superclique (Algorithm 2, line 9 and 10). This is done iteratively, until no overlap remains between any 2 cliques. At the end, I construct a new, approximated graph from the cliques. In this approximated graph, the nodes are the same as in the original, but edges are drawn if and only if two nodes are in the same clique. In this state, the graph consists purely of cliques, that are disjoint since no overlap exists. Hence, no node of one clique senses any node of any other clique. Since any crosstalk is eliminated, I now represent each clique by a single representative node.

Die approbierte gedruckte Originalversion dieser Dissertation ist an der TU Wien Bibliothek verfügbar.
The approved original version of this doctoral thesis is available in print at TU Wien Bibliothek.
TU Bibliothek Your knowledge hub WIEN

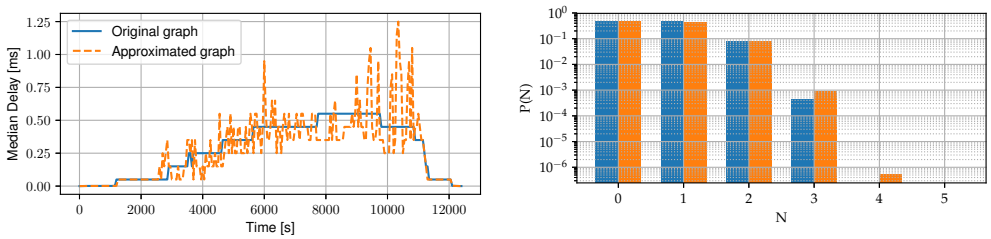

(a) Median channel access delay.

(b) Probability of N incoming packets.

Figure 3.14: Graph approximation evaluation.

To assess the performance of this algorithm, I now consider the performance metrics. I simulate the median channel access delay (Fig. 3.14a), as well as the probability of a node seeing N parallel incoming transmissions (Fig. 3.14b). The results show 2 noteworthy properties. The median statistics replicate the original well apart from noise introduced due to this quantization. Therefore, the approximated clique graph is used as a graph with similar behavior. Furthermore, both pose strongly similar collision probabilities. Finally, almost the full probability in both cases is concentrated in $N \in [0,2]$, meaning that a node rarely sees more than 2 simultaneous incoming packets. Therefore, I assume that 2 transmitters can be used to effectively emulate the behavior of a larger number of vehicles.

3.3.7 Channel Approximation

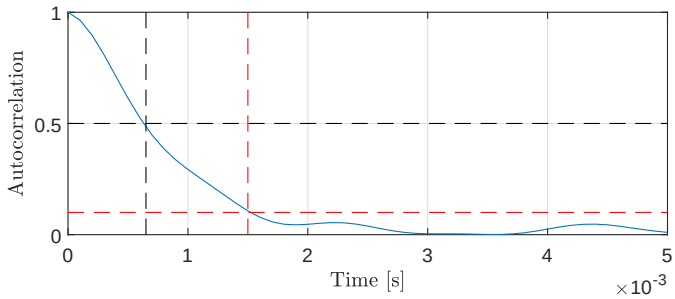

Figure 3.15: Magnitude of the autocorrelation function of the frequency domain channels.

As the system model in Fig. 3.12 shows, for N potentially incoming transmissions, I need to replicate N uncorrelated vehicular channels. With respect to small-scale fading, I assume all communications to follow the *urban approaching* channel model presented in Table C.1. Thus, the N different channels $h_1(t,\tau), h_2(t,\tau), h_3(t,\tau), \ldots, h_N(t,\tau)$ are all realizations of one single channel model. I now assume $h'(t,\tau)$ to be a random realization generated according to the modified sum-of-sinusoids approach given in [91] with a given seed. Then, due to the ergodic properties, the N channels is taken as $h'(t+\delta_1,\tau), h'(t+\delta_2,\tau), \ldots, h'(t+\delta_N,\tau)$. Thus, the same trace is used, with different random offsets δ_N. This approach works, as long as the δ_N are large enough for the channels to be decorrelated. Figure 3.15 shows the magnitude of

Die approbierte gedruckte Originalversion dieser Dissertation ist an der TU Wien Bibliothek verfügbar.
The approved original version of this doctoral thesis is available in print at TU Wien Bibliothek.
TU Bibliothek Your knowledge hub WIEN

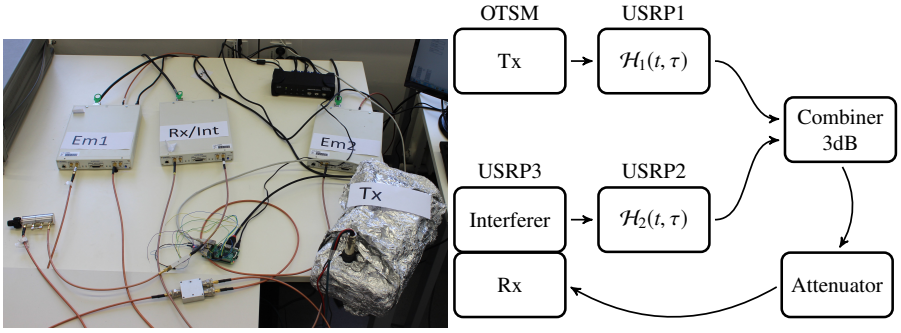

(a) Lab setup. (b) Schematic of setup.

Figure 3.16: Measurement setup.

the sample autocorrelation function of the channel trace, calculated as

$$\text{Autocorrelation}(\tau) = \left| \frac{1}{\|\boldsymbol{h}\|_2^2} \sum_{t=1}^{T} h[t]h[t+\tau]^* \right|. \tag{3.15}$$

Thus, the correlation is below 50 % at 0.5 ms, and below 10 % at 1.5 ms. Given that the packet transmissions considered are 0.4 to 0.8 ms long, subsequent transmissions, even at highest possible rate, see completely decorrelated channels within $2-4$ transmissions. Hence, I argue, when analyzing over suitably long durations, I use a single small-scale fading channel emulator and transmit packets from a whole clique over the emulator. Due to the fast decorrelation of the channel, this results in a performance that is equivalent to having a separate channel for each transmitting node individually.

3.4 Network Performance Evaluation

I now evaluate the performance for two scenarios. The first scenario is a simplified scenario where a communication link sees a clique of hidden nodes. Thus, only one of the interferers is active at any given time, and the total interference load depends on the clique size. In this scenario, I consider constant interference power. This result yields a baseline sensitivity to interference depending on the density of the surrounding network. In the second scenario, I consider a link in the presented traffic simulation, and evaluate the expected packet error rate as a function of simulation duration. For this evaluation approach, I take advantage of the results, that show that representative channels are achieved with a small amount of nodes and channel emulators. Thus, I use physical nodes for transmitter, receiver and interferer, as well as physical hardware channel emulators. The presented scenarios are evaluated through conducted measurements.

As previously established, I only require a small number of nodes to evaluate the given scenarios. The lab setup that is used is depicted in Fig. 3.16. The figure shows a photo and schematic of the employed measurement setup. As transmitter for the signal of interest, I

Die approbierte gedruckte Originalversion dieser Dissertation ist an der TU Wien Bibliothek verfügbar.
The approved original version of this doctoral thesis is available in print at TU Wien Bibliothek.
TU Bibliothek Your knowledge hub WIEN

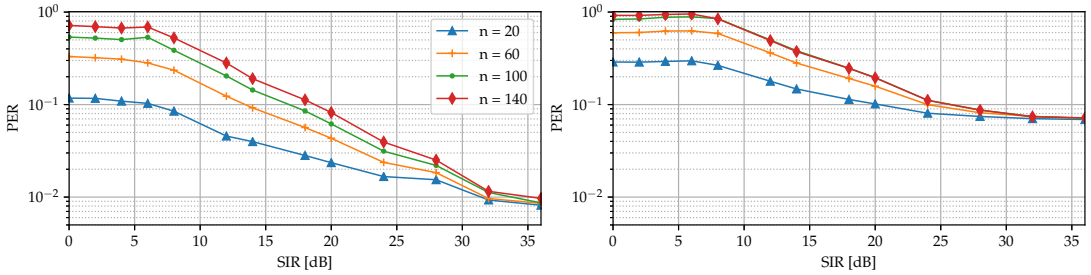

(a) 258 Bytes (b) 500 Bytes

Figure 3.17: PER versus SIR for interfering cliques of different sizes. For 500 bytes, no difference exists for 100 and 140 interferers.

use a Off-the-Shelf Modem (OTSM). For the interferer and receiver, I exploit the fact that NI USRP-2953R SDR have two separate radio frequency daughter boards, which is why one device is used for both functionalities. This USRP is running the 802.11 application framework, modified for 802.11p. I also use two further USRPs that run the custom channel emulator code. Both transmitter paths are combined in a power combiner, and passed through a final RADITEK RVATTN-DC-6 (0-70 dB) switched attenuator back to the receiver path of the USRP. For a measurement run, the OTSM transmits a set number of 500000 packets in a continuous stream. The interferer on the other hand, has to transmit a pattern according to the full interfering clique. I achieve this by forwarding arbitrarily scheduled packets from a simulation trace via a Universal Datagram Protocol (UDP) socket to the transmitting node. This trace is generated by running the packet transmission simulations for a clique of the given size. The two emulators are running the same small-scale fading trace, but with suitably decorrelated offsets. Since the interferer represents multiple nodes that may see different pathlosses, the channel emulator in the interferer path additionally can switch path gain on a per millisecond basis to emulate this behavior.

3.4.1 Performance under Clique of Hidden Nodes

I first analyze the packet performance in the presence of a single clique with constant pathloss and size. I neglect the influence of additive noise, and therefore configure the transmitter to see Received Signal Strength Indicator (RSSI) at −50 dBm. This leaves the influence of the small-scale fading, as well as the interference. I consider cliques of 40, 60, 100 and 140 vehicles that are using the same channel as the transmitting node. I evaluate the performance in terms of PER over the SIRs, which I define as the difference in decibels of the RSSIs, from 0 to 36 dB.Furthermore, I emulated two different sizes for the packet transmissions (258 and 500 bytes).

Figure 3.17 shows the results of the measurements. All results show 3 distinct regions. Below ≈ 6 dB, the PER is a constant. At these SIRs, the PER is effectively a product of the error probability without interference and the probability of an interferer transmission overlapping

Die approbierte gedruckte Originalversion dieser Dissertation ist an der TU Wien Bibliothek verfügbar.
The approved original version of this doctoral thesis is available in print at TU Wien Bibliothek.
TU Bibliothek Your knowledge hub WIEN

with the transmission of interest. Due to the low SIR, any overlap is sufficient to lose the packet in the CRC. Above 30 dB, a saturation of the performance is observed for all clique sizes. This is where the interference becomes unnoticeable and the PER is caused completely by the small-scale fading channel. This saturation happens at very high SIRs because I am plotting over median values for both transmitter and interferer. Since fading is observed on both sides, even at high SIRs momentary dips are frequently observed that lead to packet loss. These two regions are connected by a linear transition.

3.4.2 Performance in Traffic Simulations

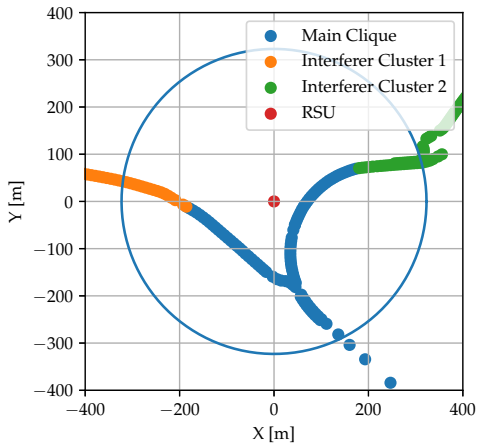

Figure 3.18: Snapshot of clique distribution [85].

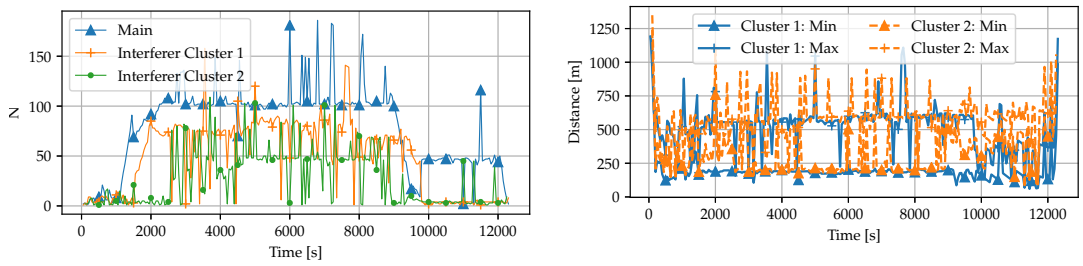

(a) Clique sizes.

(b) Clique distances.

Figure 3.19: Change of clique parameters over simulation time.

I now investigate the dynamic performance in the presented simulation traces. I do this by assuming a virtual Roadside Unit (RSU) at the interference hotspot, which is at the merging point of the two highways right before the bridge. The location of this virtual RSU is shown in Fig. 3.18. The figure also shows for a given time snapshot the clique assignments from the graph approximation. The blue clique is the clique of potential communication partners, while the orange and green clique are interfering cliques. Finally, the circle denotes the communica-

Die approbierte gedruckte Originalversion dieser Dissertation ist an der TU Wien Bibliothek verfügbar.
The approved original version of this doctoral thesis is available in print at TU Wien Bibliothek.
TU Bibliothek Your knowledge hub WIEN

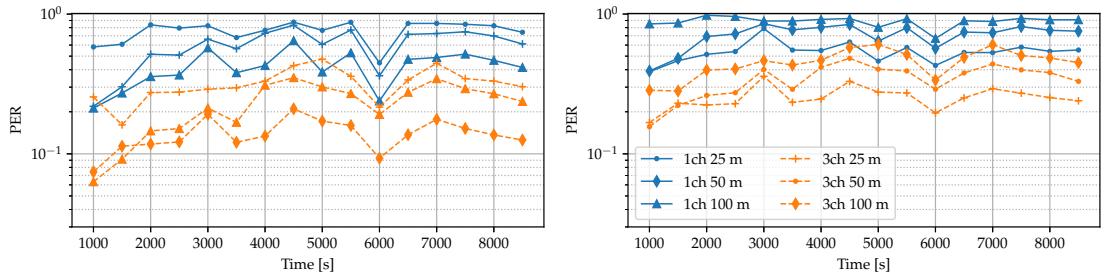

(a) 258 Bytes (b) 500 Bytes

Figure 3.20: PER simulation time for 1 and 3 used channels, and distances of 25, 50 and 100 m to the receiver.

tion range. To achieve the performance analysis, I analyze the achievable performance for different transmitter positions in 25, 50, and 100 m distance from the RSU. Figure 3.19 shows the essential parameters for the interfering cliques calculated through this approximation algorithm. Figure 3.19a shows the sizes of the 3 cliques of interest, while Fig. 3.19b shows the minimum and maximum distances from clique nodes to the virtual RSU. The resulting parameters show that the simulation enters a relatively steady state at around 2500 s, and remains in this steady state for 6500 s. In this stationary regime, the first interfering clique sees $N \approx 80$ nodes, and the second interfering clique sees $N \approx 50$ nodes. Both cliques have distances distributed between 150 and 600 m from the RSU receiver. As all the considered roads are more or less straight, and the clusters are aligned along these roads, I assume that the nodes are uniformly distributed between those minimum and maximum values. Hence, I concentrate on this stationarity region for further measurements. To set the RSSI for the signal of interest, the pathloss is evaluated according to [30] for distances of 25, 50 and 100 m. I use these distances, as well as the interferer distances, to draw a new random SIR value every 1 ms. This value is then realized by setting the attenuation in the interfering channel emulator. This approach does not guarantee the interferer strength to change only *between* transmissions. Since I only apply this to the interfering nodes, the resulting PER is representative for the scenario. Using this approach, I now evaluate the scenario for both chosen packet sizes, and for the configurations with one usable channel and three usable channels [92]. The resulting PER as function of time is shown in Fig. 3.20. The results show that excluding the ramp-up and ramp-down of the simulation,n the resulting PERs assume an almost constant value, with small fluctuations caused by the fluctuations of the clique sizes. Furthermore, a persistently high packet loss is observed, with only short packets, close to the receiver seeing a small throughput. This is influenced by the large interfering clique sizes and the relative proximity of the interferers. According to Fig. 3.17, an SIR well above 10 dB is required to see increased performance. This is seldom achieved for the parameters of the simulation. The throughput is improved by using short packets and 3 channels, however even then packet loss reaches more than 20 % for a distance of 100 m to the receiver.

Die approbierte gedruckte Originalversion dieser Dissertation ist an der TU Wien Bibliothek verfügbar.
The approved original version of this doctoral thesis is available in print at TU Wien Bibliothek.
TU Bibliothek Your knowledge hub WIEN

3.5 Discussion

The single link evaluation confirms the approach of using a channel emulator for performance estimation. The playback of measurement estimates allows to test the scenario in a lab. However, incorporating the large-scale fading proves challenging due to the large dynamic range required that causes quantization noise for low received powers. The presented stationary channel models do not suffer from this problem, as they are defined purely as small scale models. To model both small scale and large scale behavior, the pathloss has to be emulated separately or incorporated in simulation. This avoids quantization noise. However, the presented stationary channel models allow to cover a variety of scenarios, from almost AWGN to near total packet loss. While they only use four taps, the results in the previous chapter show that cluster-sparse channels are a good match for vehicular communications, and using four taps fits very well for this. This is true when considering that the IEEE 802.11p transceivers have a 10 MHz wide RF input bandpass, which means that the temporal and spatial resolution for multipath is very low. The single-link results show that IEEE 802.11p especially struggles with strongly time-varying channels, and strong multipath further deteriorate the signal. This is in line with the fact that IEEE 802.11p does full channel estimation on all subcarriers only at the start of a frame, which progressively outdates. Strong multipath further means that linear interpolation between the pilots is less helpful.

The network analysis then demonstrates how strongly the packet performance is influenced by the hidden node problem. For the chosen scenario, a urban traffic jam, the communication network is strongly connected and therefore prone to hidden node transmissions. However, by using an approximation algorithm, it is possible to find a vastly simpler description, that leads to comparable transmission statistics. Using this simpler description, I am able to show that a strongly loaded channel completely dominates the packet error probability. Thus, congestion control algorithms such as the Distributed Congestion Control (DCC) [93] are vital, as only in low- to medium-load scenarios, the protocol is expected to operate in its expected capacity.

In order to fully model the communication channel, the results show that both aspects have to be considered. Transmission performance on all considered channels saturates for high enough received powers. Hence, depending on the observed vehicular channel, very little throughput is possible. On the other hand, in a dense network, capturing the hidden nodes is essential to modeling the performance. Hence, I proposed the solution of using an approach that captures both in a representative fashion.

Die approbierte gedruckte Originalversion dieser Dissertation ist an der TU Wien Bibliothek verfügbar.
The approved original version of this doctoral thesis is available in print at TU Wien Bibliothek.
TU Bibliothek Your knowledge hub WIEN

4 Network Abstraction

The previous chapters have proposed and analyzed approaches of how to break down the numeric evaluation of $\Pr(\mathscr{E})$ into components that are of manageable complexity. Now, I proceed one step further. The goal is now to establish a probabilistic description that abstracts the channel and the network descriptions. The goal is to find a stochastic abstraction for $\Pr(\mathscr{C}[i]|\mathscr{H}[i],)$, which can then be combined with a model for $\Pr(\mathscr{C}[i]|\mathscr{N}[i])$. The results of the previous chapter show that the burstiness of the channel is not always negligible. As latency is crucial in the vehicular safety setting, waiting for the burst of bad channel conditions to end may not be possible. Therefore, it is important to integrate burstiness in a stochastic model for the performance. I want the model to capture the error burst characteristics introduced by variations of the channel, and not only average behavior. Therefore, I use the Gilbert-Elliott model [94, 95]. I show a systematic way of estimating a Gilbert-Elliott model description from measurement traces.

To demonstrate the capabilities of this approach, I use nonstationary packet transmission measurement traces conducted by two cars on a highway. This measurement exhibited strong bursty properties, and is therefore a good demonstration measurement.

After modeling the burstiness of a single link, I apply the Information Bottleneck to reduce the model space to an optimal trade-off of granularity and simplicity. Finally, I model a highway traffic jam using TraffSim and compute a stochastic description for the packet loss due to interference. The result shows that for different parameter combinations, different aspects of $\mathscr{H}$ and $\mathscr{N}$ dominate $\Pr(\mathscr{E})$, which demonstrates that it is essential to have an adequate approach at modeling all aspects.

The model fits discussed in the following section are based on measurements that were taken as part of the ROADSAFE campaign [96] in 2011 over the span of 5 days on a highway east of Vienna, Austria. Two cars with roof-mounted antennas were driving in the same direction for 10771 s with roof-mounted antennas. The transmitting car generated packet traffic using a Cooperative Vehicle-Infrastructure Systems (CVIS) box [97]. The transmission parameters are shown in Table 4.1. The recorded data for every packet transmission includes RSSI estimates

Die approbierte gedruckte Originalversion dieser Dissertation ist an der TU Wien Bibliothek verfügbar.
The approved original version of this doctoral thesis is available in print at TU Wien Bibliothek.
TU Bibliothek Your knowledge hub WIEN

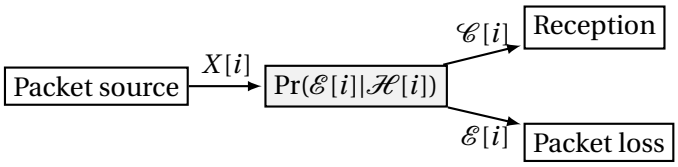

Figure 4.1: System Model.

and noise power estimates in integer decibel values, allowing to calculate an SNR estimate. Furthermore, Global Positioning System (GPS) data was recorded for both cars, and video recordings for visual documentation and detailed analysis. A truck was used to produce repeatable NLOS conditions on two of the measurement days. Alongside of LOS and NLOS scenarios, overtaking maneuvers were also recorded.

Table 4.1: Measurement parameters

Bitrate	6Mbit/s
Modulation/Coding	QPSK, Rate 1/2
Packet length	500 Bytes
Mean packet rate	$970\,\mathrm{s}^{-1}$
Transmit power	10 dBm

I first present the assumptions of the Gilbert-Elliot model, and an extension to nonstationary situations. Then, the maximum-likelihood estimation of the model parameters from measurement traces is considered. In Section 4.6, I use the information bottleneck ([98]) and AIC ([49]) to find the Gilbert-Elliott model of least complexity. Finally, mobility simulations are included as well as packet loss due to interference. The results show that considering accurate models for both is vital, as different operating regimes are limited by different influences.

This chapter is based on [60], with additional results from [61].

4.1 The Gilbert-Elliott Model

I assume the single link communication between two vehicles to be a nonstationary packet error channel (Fig. 4.1). A source generates a data packet $X[i]$ at instant i, and this packet is either received correctly ($\mathscr{C}[i]$), or it is dropped ($\mathscr{E}[i]$).The packet loss probability is $\Pr(\mathscr{E}[i]|\mathscr{H}[i])$. I now want a simple stochastic description for this probability. The goal is to model first- and second order statistics ($\Pr(\mathscr{E})$, $\Pr(\mathscr{E}_i|\mathscr{E}_{i-1})$ and $\Pr(\mathscr{C}_i|\mathscr{C}_{i-1})$). Furthermore, the model needs to cover nonstationarity, and not be more complicated than necessary.

To model the higher order statistics of the channel, I base the packet-error process on Hidden Markov Models (HMMs). These have been used to model both the channel [35, 99], and the packet errors [40]. A *indecomposable* Markov chain is a stationary model [100], as long as all transition probabilities are constant. Thus, underlying model parameters are allowed to

Die approbierte gedruckte Originalversion dieser Dissertation ist an der TU Wien Bibliothek verfügbar.
The approved original version of this doctoral thesis is available in print at TU Wien Bibliothek.
TU Bibliothek Your knowledge hub WIEN

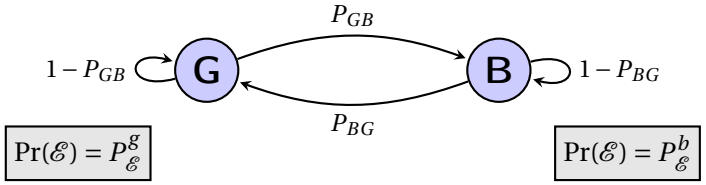

Figure 4.2: The Gilbert-Elliott model has two states, good and bad, and assigns packet error probabilities ($P^g_{\mathscr{E}}$ and $P^b_{\mathscr{E}}$) and transition probabilities (P_{GB} and P_{BG}) to both.

change after defined intervals. This replicates the long-term evolution of the channel, making the model nonstationary in the process. Since the small-scale fading is provided through the Markov model, the update time of the model parameters does not have to replicate the phase shifts of the scatterers, but instead changes in LOS-NLOS conditions, distance changes between receiver and transmitter, and changes in the road geometry. I call this the *channel scenario*, and consider all channel scenarios $\mathscr{H}$ equivalent that are modeled by the same Markov parameter set.

To capture the small-scale changes, the HMM design is based on the Gilbert-Elliott model [94], which allows modeling alternating bursts of high and low error probabilities using four parameters. The Gilbert-Elliott Model is a HMM [101] with two states, *good* (G) and *bad* (B). The model is controlled by four parameters, P_{GB}, P_{BG}, $P^g_{\mathscr{E}}$ and $P^b_{\mathscr{E}}$, which are collectively denoted as parameter quadruple $\boldsymbol{\theta}$. Without loss of generality, I assume $P^g_{\mathscr{E}} \leq P^b_{\mathscr{E}}$. As shown in Fig. 4.2, a random state transition may occur at every time step, governed by the transition probabilities P_{GB} and P_{BG}. Depending on which state the model is in, the channel sees either the packet error probability $P^g_{\mathscr{E}}$ or $P^b_{\mathscr{E}}$. Through this approach, the model is able to model alternating bursts of few and many errors. To allow adaption to a nonstationary scenario, these parameters are allowed to change, and this may occur at every time step, whenever the underlying channel changes. In Section 4.2, I set conditions for the parameter change. The average burst length depends on the transition probabilities. The duration of good (or bad) state bursts is geometrically distributed, i.e.,

$$\begin{aligned}\Pr(N_g = n) &= (1-P_{GB})^{n-1} P_{GB},\\ \Pr(N_b = n) &= (1-P_{BG})^{n-1} P_{BG}.\end{aligned} \tag{4.1}$$

The expected duration of good and bad state is calculated

$$\mu_g = \mathrm{E}\{N_g\} = \tfrac{1}{P_{GB}}, \quad \mu_b = \mathrm{E}\{N_b\} = \tfrac{1}{P_{BG}}. \tag{4.2}$$

If the system is *indecomposable*, that is as long as $(P_{GB} + P_{BG}) \in (0,2)$ holds, a unique closed form expression for $\Pr(\mathscr{E})$ is

$$\Pr(\mathscr{E})_{GE} = \underbrace{\tfrac{P_{GB}}{P_{GB}+P_{BG}}}_{P_B} P^b_{\mathscr{E}} + \underbrace{\tfrac{P_{BG}}{P_{GB}+P_{BG}}}_{P_G} P^g_{\mathscr{E}}, \tag{4.3}$$

Die approbierte gedruckte Originalversion dieser Dissertation ist an der TU Wien Bibliothek verfügbar.
The approved original version of this doctoral thesis is available in print at TU Wien Bibliothek.
TU Bibliothek Your knowledge hub WIEN

where P_G and P_B are the steady-state probabilities of being in good or bad state respectively. I now characterize the burst behavior in closed form by looking into the probability of a correct transmission at time instance i given the previous at $i-1$ was correct, $\Pr(\mathscr{C}_i|\mathscr{C}_{i-1})$, and the probability of a transmission error following a previous error $\Pr(\mathscr{E}_i|\mathscr{E}_{i-1})$. I calculate $\Pr(\mathscr{E}_i|\mathscr{E}_{i-1})$ by starting out with the law of total probabilities,

$$\Pr(\mathscr{E}_i) = \Pr(\mathscr{E}_i|\mathscr{E}_{i-1})\Pr(\mathscr{E}_{i-1}) + \Pr(\mathscr{E}_i|\mathscr{C}_{i-1})\Pr(\mathscr{C}_{i-1}), \tag{4.4}$$

and exploit the stationarity of the Gilbert-Elliott model for constant parameters resulting in $\Pr(\mathscr{E}_i) = \Pr(\mathscr{E}_{i-1}) = 1 - \Pr(\mathscr{C}_{i-1}) = \mathrm{PER}_{GE}$. Furthermore, the joint probability of first a correct transmission, then an error occurring is given as

$$\begin{aligned}\Pr(\mathscr{E}_i, \mathscr{C}_{i-1}) =& P_G(1-P^g_{\mathscr{E}})(P_{GB}P^b_{\mathscr{E}} + (1-P_{GB})P^g_{\mathscr{E}}) + \\ & P_B(1-P^b_{\mathscr{E}})(P_{BG}P^g_{\mathscr{E}} + (1-P_{BG})P^b_{\mathscr{E}}).\end{aligned} \tag{4.5}$$

Here, I use the total probability theorem to assume the initial state is either good or bad at the first transmission, given by the steady state probabilities P_G or P_B. Then, I know no error occurs, and afterwards consider all possible state transitions with the respective error probabilities. Equation (4.4) and Eq. (4.5) together with the fact that $\Pr(\mathscr{E}_i, \mathscr{C}_{i-1}) = \Pr(\mathscr{E}_i|\mathscr{C}_{i-1})\Pr(\mathscr{C}_i)$, lead to

$$\Pr(\mathscr{E}_i|\mathscr{E}_{i-1}) = \frac{P_{BG}(P^g_{\mathscr{E}})^2 + P_{GB}(P^b_{\mathscr{E}})^2 - P_{GB}P_{BG}(P^g_{\mathscr{E}} - P^b_{\mathscr{E}})^2}{P_{BG}P^g_{\mathscr{E}} + P_{GB}P^b_{\mathscr{E}}}, \tag{4.6}$$

$$\Pr(\mathscr{C}_i|\mathscr{C}_{i-1}) = \frac{P_{BG}(P^g_{\mathscr{C}})^2 + P_{GB}(P^b_{\mathscr{C}})^2 - P_{GB}P_{BG}(P^g_{\mathscr{C}} - P^b_{\mathscr{C}})^2}{P_{BG}P^g_{\mathscr{C}} + P_{GB}P^b_{\mathscr{C}}}, \tag{4.7}$$

where $P^g_{\mathscr{C}}$ and $P^b_{\mathscr{C}}$ are the complements of $P^g_{\mathscr{E}}$ and $P^b_{\mathscr{E}}$, and hence the derivation for Eq. (4.7) is completely analogous to Eq. (4.6). The model works on an event-based time-scale, indexed by brackets $x[i]$. Thus, two consecutive events at indices i and $i+1$ do not have a fixed measurement time gap between them. They are, however, ordered strictly chronologically, that is j happened after i in terms of measurement time if and only if $j > i$.

4.2 Maximum Likelihood Estimation

The goal is to estimate the time varying Gilbert-Elliott parameter quadruple $\boldsymbol{\theta}[i]$. As indicated in the previous section, I assume that every channel scenario $\mathscr{H}$ is assigned exactly one such quadruple. To find the optimum choice, I formulate the likelihood function for the estimation problem, and introduce assumptions with respect to the channel scenarios. Based on the set of assumptions in force, different solutions to the maximum likelihood problem appears, with different characteristics.

Die approbierte gedruckte Originalversion dieser Dissertation ist an der TU Wien Bibliothek verfügbar.
The approved original version of this doctoral thesis is available in print at TU Wien Bibliothek.
TU Bibliothek Your knowledge hub WIEN

The likelihood for the time varying Gilbert-Elliott parameters $\boldsymbol{\theta}[i]$ base on the observed events $\boldsymbol{x} \in \Omega_H = \{\mathscr{E}, \mathscr{C}\}^N$ and sequence of channel scenarios $\boldsymbol{h} \in \Omega_H = \{\mathscr{H}_1, \mathscr{H}_2, \ldots\}^N$ is given as

$$\mathscr{L}(\boldsymbol{\theta}[i]|\boldsymbol{x}, \boldsymbol{h}) = \Pr(\boldsymbol{x}|\boldsymbol{h}; \boldsymbol{\theta}[i]), \tag{4.8}$$

which is rewritten as

$$\mathscr{L}(\boldsymbol{\theta}[i]|\boldsymbol{x}, \boldsymbol{h}) = \prod_{i=1}^{N} \Pr(x[i]|x[1], \ldots, x[i-1], \boldsymbol{h}; \boldsymbol{\theta}[i]). \tag{4.9}$$

The set of Gilbert-Elliott parameters $\boldsymbol{\theta}[i]$ is thus conditionally dependent on the channel scenario that is in force at time instance i. I regroup this expression in terms of time instead of events, which is measured in seconds. To this end, I introduce $t[i]$ as the second in which event i occurs relative to the first event, and denote the final timestamp $T = t[N]$. In this way, all events having relative timestamps between 0 and 1 s are assigned to the first second $t[i] = 1$, and so forth. I then rewrite the product in Eq. (4.9) in groups of whole seconds τ

$$\mathscr{L}(\boldsymbol{\theta}[i]|\boldsymbol{x}, \boldsymbol{h}) = \prod_{\tau=1}^{T} \underbrace{\prod_{\substack{i=1,\\ t[i]=\tau}}^{N} \Pr(x[i]|x[1], ..., x[i-1], \boldsymbol{h}; \boldsymbol{\theta}[i])}_{\mathscr{L}_\tau(\boldsymbol{\theta}[i]|\boldsymbol{x}, \boldsymbol{h})}. \tag{4.10}$$

Here, the product with respect to i only evaluates factors within one second, while the product with respect to τ multiplies over the whole time span in 1 s increments. The i-indexed product again has the shape of a likelihood function, but only considers realizations within the τth second, hence is denoted as partial likelihood $\mathscr{L}_\tau(\boldsymbol{\theta}[i]|\boldsymbol{x}, \boldsymbol{h})$. In the following sections, I wish to find the $\boldsymbol{\theta}[i]$ that maximizes Eq. (4.10), yielding the maximum likelihood estimates. I gradually impose assumptions on the behavior of $\boldsymbol{h}$ with the aim of deriving reduced-complexity parameter estimates that still approximately replicate the behavior of the given traces. Section 2.5.4 analyzes the performance of the subsequently derived estimators, demonstrating the validity of the introduced assumptions.

4.2.1 Block Constant Channel

As previously mentioned, the channel scenario sequence $\boldsymbol{h}$ is only meant to capture large-scale changes, since the small-scale variations are captured using the Markov model. Considering the fact that even on the highway, vehicles do not move more than ~ 35 m per second, I impose the assumption that the channel scenario does not change for 1 s. Therefore, the block of events that occur within one second see time variation produced by the GE model with unchanging parameters. I furthermore impose that I am unable to benefit from mutual information between the channels of two separate time instances, which is equivalent to

Die approbierte gedruckte Originalversion dieser Dissertation ist an der TU Wien Bibliothek verfügbar.
The approved original version of this doctoral thesis is available in print at TU Wien Bibliothek.
TU Bibliothek Your knowledge hub WIEN

assuming the channel scenarios of two different seconds to be statistically independent,

$$h[i] \overset{!}{=} \mathscr{H}_\tau \qquad \forall i \text{ s.t. } t[i] = \tau, \tag{4.11}$$

$$\Pr(\mathscr{H}_\tau, \mathscr{H}_{\tau'}) = \Pr(\mathscr{H}_\tau)\Pr(\mathscr{H}_{\tau'}) \qquad \forall \tau \neq \tau'. \tag{4.12}$$

Note that the second assumption does not imply the actual channel behavior, but rather a simplifying assumption which precludes the agility to extract dependencies in time. After applying these conditions, the partial likelihood of the τth second simplifies to

$$\mathscr{L}_\tau(\boldsymbol{\theta}|\boldsymbol{x},\boldsymbol{h}) = \prod_{\substack{i=1,\\ t[i]=\tau}}^{N} \Pr(x[i]|x[1],\ldots,x[i-1],\mathscr{H}_\tau;\boldsymbol{\theta}). \tag{4.13}$$

Here, I take advantage of the fact that I assume the channel scenario to be constant within the second, and that one scenario relates to a single unique parameter quadruple $\boldsymbol{\theta}$, eliminating the time dependence of the parameters within the second. Furthermore, since the channel scenario is a fixed constant within a given time τ, optimizing the likelihood function is conditionally independent of it. Additionally, the events x that didn't happen in second τ are assumed statistically independent of the events that did due to different channel scenarios being in force, further simplifying the expression to

$$\mathscr{L}_\tau(\boldsymbol{\theta}_\tau|\boldsymbol{x},\boldsymbol{h}) = \Pr(\boldsymbol{x}_\tau;\boldsymbol{\theta}), \tag{4.14}$$

with $\boldsymbol{x}_\tau$ being the sequence of all events x occurring within second τ. This formulation eliminates all dependence on events outside τ, meaning that instead of jointly maximizing Eq. (4.10), I optimize Eq. (4.14) for every second individually. Given a sufficiently long realization $\boldsymbol{x}$, the maximum likelihood estimation for $\boldsymbol{\theta}$ are then be evaluated on a per-second basis as the block-constant (denoted in equations as BC) estimate by taking the argument maximizing the partial likelihood

$$\hat{\boldsymbol{\theta}}_\tau^{(BC)} = \arg\max_{\boldsymbol{\theta}} \Pr(\boldsymbol{x}_\tau;\boldsymbol{\theta}). \tag{4.15}$$

Here, block-constant refers to the model parameters estimates remaining constant, not the channel itself. Sufficiently long in this context means long enough for the Markov Model to reach steady state, and is dependent on the parameter quadruple. Results from the measurements indicate that an event count approaching 1000 per second fulfills this assumption very well. The maximum of the likelihood expression for a given received sequence is found using the Baum-Welch algorithm [102].

4.2.2 Scenario Classification by Mean SNR

I now impose a second requirement on the channel. Additional to the block-constant channel, I classify the channel $\mathscr{H}_\tau$ based on the mean received SNR $\bar{\gamma}_\tau$ that is recorded during second τ. This is calculated by transforming the SNR into linear scale, averaging, and transforming back

TU Bibliothek Your knowledge hub WIEN
Die approbierte gedruckte Originalversion dieser Dissertation ist an der TU Wien Bibliothek verfügbar.
The approved original version of this doctoral thesis is available in print at TU Wien Bibliothek.

to decibels. I bin the SNR range in 1 dB steps, and assume that the same channel scenario was in force in two separate seconds if the recorded mean SNRs fall in the same dB bin

$$\lceil \bar{\gamma}_\tau[\mathrm{dB}] \rceil = \lceil \bar{\gamma}_{\tau'}[\mathrm{dB}] \rceil = \bar{\gamma} \implies \mathscr{H}_\tau = \mathscr{H}_{\tau'} = \mathscr{H}_{\bar{\gamma}}. \tag{4.16}$$

This allows to combine Eq. (4.10) and Eq. (4.15) and identify seconds where I expect the same parameter quadruple $\boldsymbol{\theta}$ to be in place. I group the products by seconds where the mean SNRs $\bar{\gamma}_\tau$ fall into the same bin, and then multiply partial likelihoods for all those bins

$$\mathscr{L}(\boldsymbol{\theta}[i]|\boldsymbol{x},\boldsymbol{h}) = \prod_{\bar{\gamma}=-\infty}^{\infty} \underbrace{\prod_{\substack{\tau=1,\\ \bar{\gamma}_\tau \in [\bar{\gamma},\bar{\gamma}+1)}}^{T} \Pr(\boldsymbol{x}_\tau|\mathscr{H}_\gamma;\boldsymbol{\theta}_{\bar{\gamma}})}_{\mathscr{L}_{\bar{\gamma}}(\boldsymbol{\theta}_{\bar{\gamma}}|\boldsymbol{x})}. \tag{4.17}$$

In this case, maximizing the whole expression is done by finding a quadruple $\boldsymbol{\theta}_{\bar{\gamma}}$ for every SNR bin separately that maximizes $\mathscr{L}_{\bar{\gamma}}(\boldsymbol{\theta}_{\bar{\gamma}}|\boldsymbol{x})$, which is again independent of $\mathscr{H}_\gamma$ since that parameter is already fixed as a constant. Optimizing this proves difficult, as it requires finding a parameter quadruple that finds a joint maximum over all contributing seconds. For purposes of model evaluation, I introduce the vector $\boldsymbol{x}_{\bar{\gamma}}$, which concatenates all event vectors $\boldsymbol{x}_\tau$ attributed to a given $\bar{\gamma}$ value:

$$\boldsymbol{x}_{\bar{\gamma}} = [\boldsymbol{x}_{\tau_1}^T, \boldsymbol{x}_{\tau_2}^T, \ldots, \boldsymbol{x}_{\tau_j}^T]^T \quad \forall \tau \text{ s.t. } \bar{\gamma}_\tau \in [\bar{\gamma}, \bar{\gamma}+1). \tag{4.18}$$

I now introduce the likelihood function for this concatenated vector

$$\mathscr{L}'_{\bar{\gamma}}(\boldsymbol{\theta}_{\bar{\gamma}}|\boldsymbol{x}_{\bar{\gamma}}) = \Pr(\boldsymbol{x}_{\bar{\gamma}};\boldsymbol{\theta}_{\bar{\gamma}}), \tag{4.19}$$

for which a maximum is found with respect to $\boldsymbol{\theta}_{\bar{\gamma}}$ as before. Maximizing $\mathscr{L}'_{\bar{\gamma}}$ will in general not yield the same result as maximizing $\mathscr{L}_{\bar{\gamma}}$, but the variation depends on the transition probabilities in relation to the lengths of the subvectors $\boldsymbol{x}_{\tau_j}$. If the event vectors are long enough such that the overall packet error of each vector converges towards PER_{GE} (Eq. (4.3)), the estimate approaches the maximum likelihood estimate. This condition is met in all further analysis. In that case $\mathscr{L}'_{\bar{\gamma}}$ is a good approximation of $\mathscr{L}_{\bar{\gamma}}$. I therefore introduce the mean SNR grouped (Γ) estimate as

$$\hat{\boldsymbol{\theta}}_{\bar{\gamma}}^{(\Gamma)} = \arg\max_{\boldsymbol{\theta}} \Pr(\boldsymbol{x}_{\bar{\gamma}};\boldsymbol{\theta}). \tag{4.20}$$

4.2.3 Fading Aware Parameter Estimation

In this section, I outline one way of estimating the model parameters on-line, based on the SNR process $\Gamma[i]$. I build on the assumption of block-constant channel scenarios and the classification by mean SNR, and now add the assumption that the instantaneous SNR $\Gamma[i]$

Die approbierte gedruckte Originalversion dieser Dissertation ist an der TU Wien Bibliothek verfügbar.
The approved original version of this doctoral thesis is available in print at TU Wien Bibliothek.
TU Bibliothek Your knowledge hub WIEN

carries information about which state the HMM is in at the moment. Specifically, I assume that the *good-bad* changes of the model are predominantly caused by small-scale fading variations. Furthermore, I suggest that for every mean SNR value, the range of the instantaneous SNR can be split into a higher and a lower region corresponding to *good* and *bad* channel conditions. Therefore, I introduce a threshold SNR $\gamma_{th}(\bar{\gamma}_\tau)$ as a function of the mean SNR, which allows to condense the fading behavior in a binary sequence $\boldsymbol{q}$

$$q[i] = \begin{cases} 1 & \gamma[i] \geq \gamma_{th}(\bar{\gamma}_{t[i]}) \\ 0 & \text{otherwise} \end{cases} . \tag{4.21}$$

Under the given assumptions, the likelihood function $\mathscr{L}$ becomes conditionally dependent on the fading sequence $\boldsymbol{q}$

$$\mathscr{L}(\boldsymbol{\theta}[i]|\boldsymbol{x},\boldsymbol{q},\boldsymbol{h}) = \prod_{\gamma'=-\infty}^{\infty} \underbrace{\prod_{\substack{\tau=1,\\ \bar{\gamma}_\tau \in [\gamma',\gamma'+1)}}^{T} \Pr(\boldsymbol{x}_\tau|\mathscr{H}_{\gamma'},\boldsymbol{q}_\tau;\theta_{\gamma'})}_{\mathscr{L}_{\gamma'}(\boldsymbol{\theta}_{\gamma'}|\boldsymbol{x},\boldsymbol{q})} . \tag{4.22}$$

I now assign a general belief value $w[i]$ that indicates how reliable it is that the Markov chain is in good state at time step i when knowing a given fading history $\boldsymbol{q}$, as well as the packet error sequence $\boldsymbol{x}$ in form of a probability

$$w[i] = \Pr(S[i] = \mathscr{G}|\boldsymbol{q},\boldsymbol{x}). \tag{4.23}$$

Again, I use the likelihood function $\mathscr{L}'$ of the concatenated vector $\boldsymbol{x}_\gamma$

$$\mathscr{L}'(\boldsymbol{\theta}_\gamma|\boldsymbol{x}_\gamma,\boldsymbol{q}) = \prod_{\substack{i=1,\\ x[i]=\mathscr{E}}}^{N} w[i]P_{\mathscr{E}}^{g} + (1-w[i])P_{\mathscr{E}}^{b} \tag{4.24}$$

$$\times \prod_{\substack{i=1,\\ x[i]=\mathscr{C}}}^{N} w[i](1-P_{\mathscr{E}}^{g}) + (1-w[i])(1-P_{\mathscr{E}}^{b}). \tag{4.25}$$

The influence of the state transition probabilities is implied in the dependence of the belief $w[i]$ on past error events. For the sake of simplicity, I use the current fading value $q[i]$ as an estimate of the model state, resulting in

$$w[i] = \Pr(S[i] = \mathscr{G}|\boldsymbol{q},\boldsymbol{x}) \stackrel{!}{=} q[i]. \tag{4.26}$$

In this case, the transition parameters are fully defined by the sequence $\boldsymbol{q}$, and the likelihood function that is to be maximized depends on the error probabilities $P_{\mathscr{E}}^{g}$ and $P_{\mathscr{E}}^{b}$ and the SNR threshold map $\gamma_{th}(\bar{\gamma})$

TU Bibliothek Your knowledge hub WIEN
Die approbierte gedruckte Originalversion dieser Dissertation ist an der TU Wien Bibliothek verfügbar.
The approved original version of this doctoral thesis is available in print at TU Wien Bibliothek.

$$\mathscr{L}'_{\bar{\gamma}}(P^g_{\mathscr{E}}, P^b_{\mathscr{E}} | \boldsymbol{x}_{\bar{\gamma}}, \boldsymbol{q}) = \prod_{x_{\bar{\gamma}}=\mathscr{E}, q=1} P^g_{\mathscr{E}} \prod_{x_{\bar{\gamma}}=\mathscr{C}, q=1} (1 - P^g_{\mathscr{E}}) \times \prod_{x_{\bar{\gamma}}=\mathscr{E}, q=0} P^b_{\mathscr{E}} \prod_{x_{\bar{\gamma}}=\mathscr{C}, q=0} (1 - P^b_{\mathscr{E}}). \tag{4.27}$$

The products are calculated with respect to all times that fulfill the conditions in the subscript. Due to the chosen likelihood function, all further analysis in this section depends implicitly on $\bar{\gamma}$. For maximization of this expression, the likelihood function is maximized for the two parameters separately, with

$$\hat{P}^g_{\mathscr{E}} = \arg\max_{P^b_{\mathscr{E}}} \left((P^g_{\mathscr{E}})^{N_{\mathscr{E},q=1}} (1 - P^g_{\mathscr{E}})^{N_{q=1} - N_{\mathscr{E},q=1}} \right), \tag{4.28}$$

where $N_{q=1}$ is the total number of instances at which $q[i]$ reported a good channel, and $N_{\mathscr{E},q=1}$ is the number of errors that occurred at those instances, both for all times when the mean SNR was recorded at $\bar{\gamma}$. Differentiation with respect to $P^g_{\mathscr{E}}$ shows that the sample mean of errors while $q[i] = 1$ is the maximum likelihood estimate and an analogous derivation yields the same result with $q = 0$, leading to Fading Aware (denoted in equations as FA) estimates $P^b_{\mathscr{E}}$

$$\hat{P}^{g,(FA)}_{\mathscr{E}} = \frac{N_{\mathscr{E},q=1}}{N_{q=1}}, \qquad \hat{P}^{b,(FA)}_{\mathscr{E}} = \frac{N_{\mathscr{E},q=0}}{N_{q=0}}. \tag{4.29}$$

The equations indicate that the model has two degenerated states, if the threshold is either so high or so low that all instances are assigned to one state, that is $\boldsymbol{q}$ is the all zeros or all ones sequence, the model simplifies to a PER estimation. I calculate the optimal threshold function $\gamma_{th}(\cdot)$ by computing the likelihood function Eq. (4.27) for all integer choices of γ_{th} within these bounds of degeneracy, and pick the threshold that maximizes the likelihood function. Using this threshold, one can express P_{GB} and P_{BG} for a given mean SNR, since they are fully defined given a SNR trace $\boldsymbol{\gamma}$ and the threshold map $\gamma_{th}(\bar{\gamma})$. The maximum likelihood estimates is expressed in terms of $q[i]$ as

$$P^{(FA)}_{GB} = \sum_{\substack{i=1, \\ q_{\bar{\gamma}}[i]=1}}^{N} (1 - q_{\bar{\gamma}}[i+1]) \Big(\sum_{j=1}^{N} q_{\bar{\gamma}}[j] \Big)^{-1}, \tag{4.30}$$

$$P^{(FA)}_{BG} = \sum_{\substack{i=1, \\ q_{\bar{\gamma}}[i]=0}}^{N} q_{\bar{\gamma}}[i+1] \Big(\sum_{j=1}^{N} (1 - q_{\bar{\gamma}}[j]) \Big)^{-1}. \tag{4.31}$$

Therefore, the transition probabilities also amount to the sample mean of observed transitions following the trust in the threshold indicator $q[i]$ through Eq. (4.26). I want to point out that, since the states are fully determined by the SNR, the transition probabilities allow a certain degree of freedom in interpretation. Equations (4.30) and (4.31) define the calculation per mean SNR over the whole measurement range, but this value can also be updated once per

Die approbierte gedruckte Originalversion dieser Dissertation ist an der TU Wien Bibliothek verfügbar.
The approved original version of this doctoral thesis is available in print at TU Wien Bibliothek.
TU Bibliothek Your knowledge hub WIEN

second, by reducing the range of the sample mean:

$$P_{GB,\tau}^{(FA)} = \sum_{\substack{i=1,\\ q_{\tilde{\gamma}}[i]=1\\ t[i]=\tau}}^{N} (1-q_{\tilde{\gamma}}[i+1])\Big(\sum_{\substack{j=1\\ t[j]=\tau}}^{N} q_{\tilde{\gamma}}[j]\Big)^{-1}, \tag{4.32}$$

$$P_{BG,\tau}^{(FA)} = \sum_{\substack{i=1,\\ q_{\tilde{\gamma}}[i]=0\\ t[i]=\tau}}^{N} q_{\tilde{\gamma}}[i+1]\Big(\sum_{\substack{j=1\\ t[j]=\tau}}^{N} (1-q_{\tilde{\gamma}}[j])\Big)^{-1}. \tag{4.33}$$

Allowing these parameters to change over time means that it is possible to incorporate the time variance of the channel that is dependent on the instantaneous SNR as direct influence on the transition probability updates. In the following section, I use the time varying representation, as it provides more insight into the momentary connection of fading durations and burst lengths.

4.3 Results

4.4 Model Fitting

4.4.1 Block-Constant Fit

The block-constant fit calculates a unique quadruple per second, leading to 10771 parameter sets. Scatter plots of the four parameters over the mean SNR of the respective second are shown in Fig. 4.3. P_{GB} and $P_{\mathscr{E}}^{g}$ both tend to low values quickly, resulting in the frequent occurrence of good bursts at above 10 dB. At that range, P_{BG} shows a split behavior. There is a cluster at high values, leading to immediate transition into good state, and a second cluster at low values. This second cluster is a strong indicator that error bursts do not vanish for high SNR values. While the overall PER goes towards 0, the bad state is often still *sticky*, resulting in error bursts. This notion is reinforced as $P_{\mathscr{E}}^{b}$ shows many occurrences of high values throughout the frequency range. Overall, the figure shows that the parameters are strongly SNR dependent. This supports the subsequent approach of classifying the channel by the mean SNR.

4.4.2 Mean SNR Grouped Fit

Figure 4.4 depicts the results for $\boldsymbol{\theta}^{(\Gamma)}$ as a function of the mean SNR. Compared to Fig. 4.3, the parameters follow the densest clusters across the SNR range. P_{GB} reaches low values at 10 dB. $P_{\mathscr{E}}^{g}$ does so too, which is remarkable insofar as the model is well approximated by a pure Gilbert model at values above 10 dB (a pure Gilbert model assumes $P_{\mathscr{E}}^{g} = 0$). P_{BG} stays at low values across the SNR range, indicating that the times when the channel was close to perfect ($P_{BG} \to 1$) are by far outnumbered by channels that experienced error bursts. This is

Die approbierte gedruckte Originalversion dieser Dissertation ist an der TU Wien Bibliothek verfügbar.
The approved original version of this doctoral thesis is available in print at TU Wien Bibliothek.
TU Bibliothek Your knowledge hub WIEN

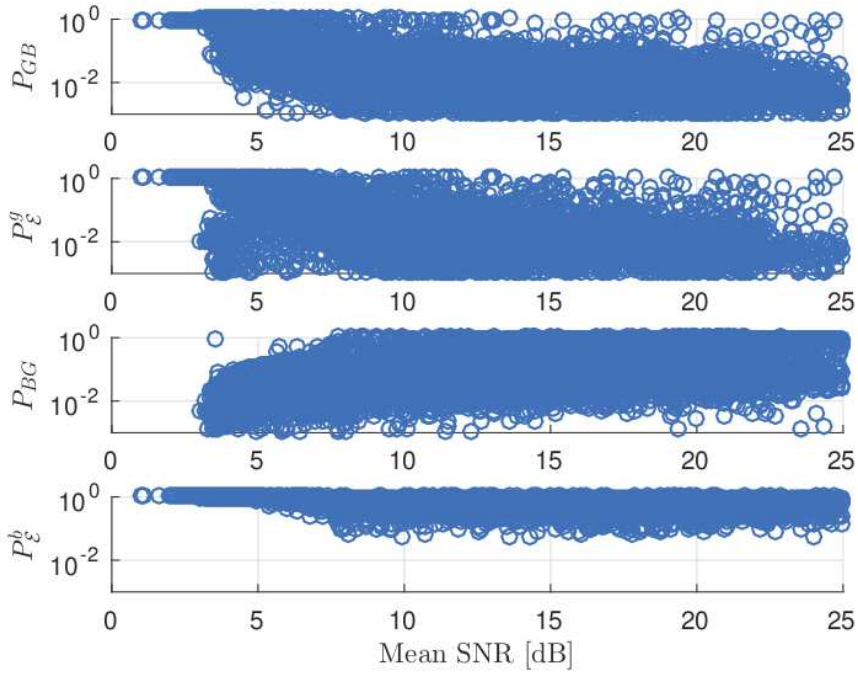

Figure 4.3: Parameter scatter plot of the block-constant fit.

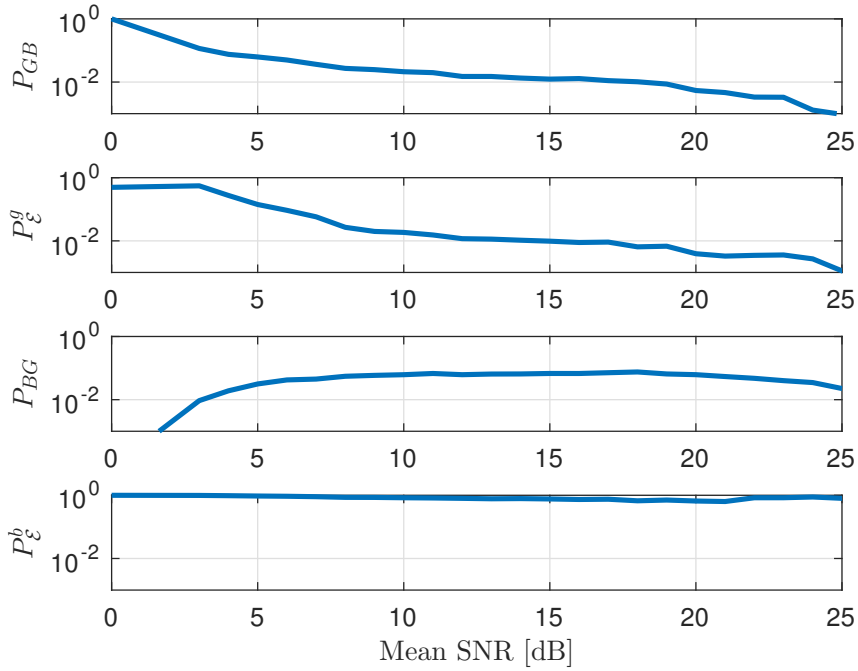

Figure 4.4: Calculated parameters for the mean SNR grouped fit.

Die approbierte gedruckte Originalversion dieser Dissertation ist an der TU Wien Bibliothek verfügbar.
The approved original version of this doctoral thesis is available in print at TU Wien Bibliothek.
TU Bibliothek Your knowledge hub WIEN

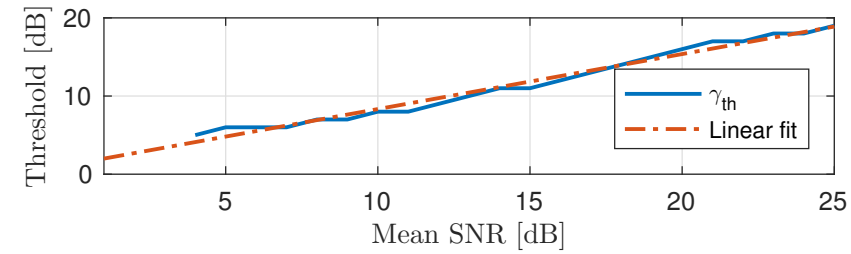

(a) Optimal threshold SNRs and linear fit.

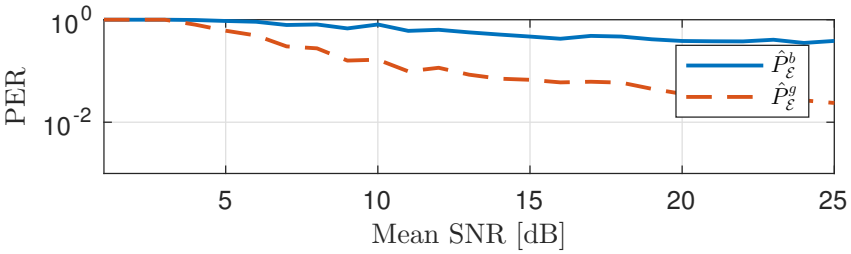

(b) Calculated PER curves for the threshold given in (a).

Figure 4.5: Optimal threshold and PER for the fading aware parameter fit.

also supported by $P_{\mathcal{E}}^{b}$, which stays above 0.6 over the whole range. For values above 22 dB, the number of realizations started to decrease, allowing measurement artifacts to influence the model (c.f. Fig. 4.4). Both transition probabilities being close to 0 over most of the SNR range is a strong indicator that the channel is generally bursty.

4.4.3 Fading Aware Fit

Figure 4.5 shows the optimal threshold SNR γ_{th} and the corresponding error probabilities plotted over the mean SNR. I see that the threshold function is well approximated by a linear fit

$$\tilde{\gamma_{th}}(\bar{\gamma}) = 1.29 + 0.7\bar{\gamma}. \tag{4.34}$$

Furthermore, the error probabilities provided by the fading aware model follow the corresponding error probabilities for the mean SNR grouped model. This result suggests that the fading behavior in this model does indeed result in at least in part the burst behavior modeled by the Gilbert-Elliott Model. Quantitatively, $P_{\mathcal{E}}^{g}$ does not decrease as fast or as far, while $P_{\mathcal{E}}^{b}$ is uniformly lower for the fading aware model than for the mean SNR grouped one. A sample time evolution of the parameters of all presented fits is shown in Fig. 4.6. The block constant fit shows a smooth time evolution of the parameters, which suggests that the time resolution of 1 s is fine enough to avoid discontinuities in the modeling. Using a new channel model every second is not usable for further work, but it gives a good baseline result to compare the other fits against. The figure shows that the mean SNR grouped fit does follow the block constant fit nicely, but it does show quantizing effects at some instances. The fading aware approach

Die approbierte gedruckte Originalversion dieser Dissertation ist an der TU Wien Bibliothek verfügbar.
The approved original version of this doctoral thesis is available in print at TU Wien Bibliothek.
TU Bibliothek Your knowledge hub WIEN

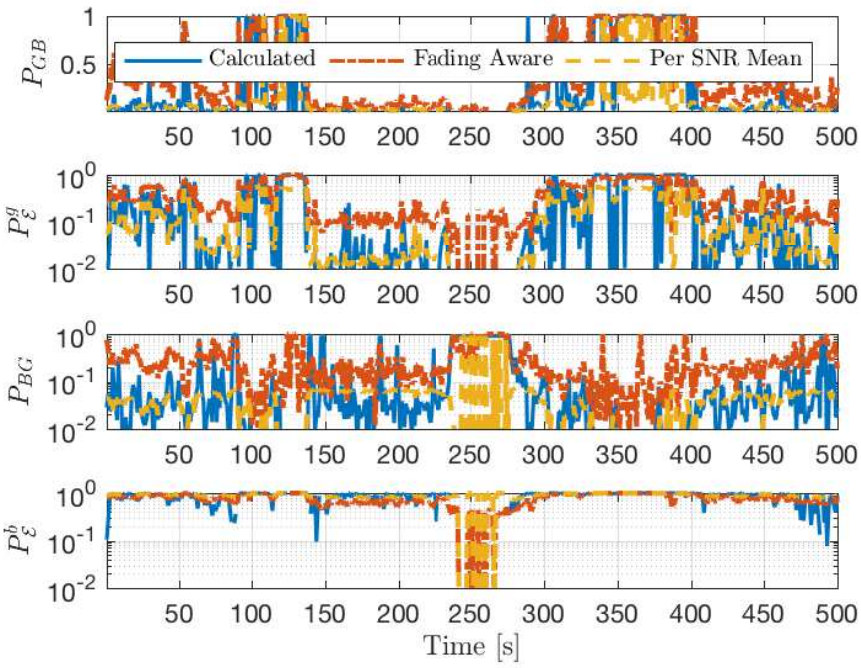

Figure 4.6: Time evolution of model parameter fits. Calculated refers to the block-constant fit.

avoids these quantizing effects, as the transition parameters are calculated per second from the given SNR trace. However, all probabilities tend to pull away from the extreme values for the fading aware model, indicating that averaging effects are introduced into the model. These averaging effects cause the model to estimate burst lengths to be shorter, which is demonstrated in the results section. Overall, both fits are closely following the reference of the block-constant fit, demonstrating the validity of the assumptions presented in the estimation section.

4.5 Evaluation of the Goodness of Fit

I now evaluate the goodness of fit of the models both with respect to the average quality and to how well the burst behavior is captured by the model. To compare the mean behavior, I calculate the measured PER, on the same per-second time frames as the model. I furthermore compare the results to the *static SNR to PER, estimate*, which represents current state of the art. I compare this to the PER, estimate produced by Eq. (4.3) for every model. Accurately calculating average burst lengths does not lend itself to analysis of time varying data, since long bursts can span 1000 events or more, translating to second long bursts. In this case, however, it is not possible average over the duration of multiple bursts, since the channel statistics vary strongly, within the period that is required to observe multiple bursts. I therefore use the previously introduced method of calculating first-order burst probabilities. I calculate

Die approbierte gedruckte Originalversion dieser Dissertation ist an der TU Wien Bibliothek verfügbar.
The approved original version of this doctoral thesis is available in print at TU Wien Bibliothek.
TU Bibliothek Your knowledge hub WIEN

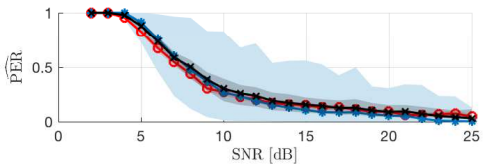

(a) Evaluated and estimated PER as a function of SNR.

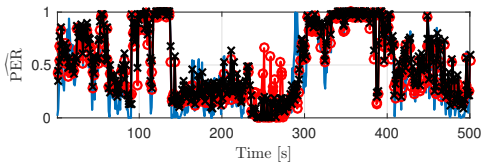

(b) Evaluated and estimated PER as a function of time.

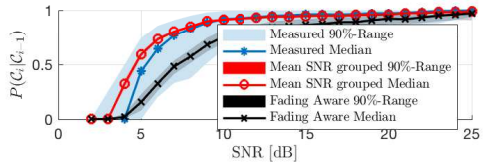

(c) $\Pr(\mathscr{C}_i|\mathscr{C}_{i-1})$ as function of SNR.

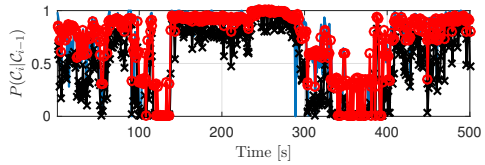

(d) $\Pr(\mathscr{C}_i|\mathscr{C}_{i-1})$ as function of time.

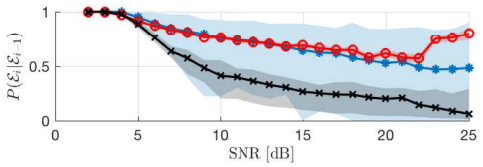

(e) $\Pr(\mathscr{E}_i|\mathscr{E}_{i-1})$ as function of SNR.

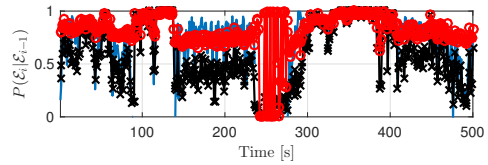

(f) $\Pr(\mathscr{E}_i|\mathscr{E}_{i-1})$ as function of time.

Figure 4.7: Evaluation of the mean SNR grouped and the fading aware model. The figures show an evaluation of the PER, as well as the burst lengths, represented by $\Pr(\mathscr{C}_i|\mathscr{C}_{i-1})$ and $\Pr(\mathscr{E}_i|\mathscr{E}_{i-1})$. Figures (a), (c) and (e) show the behaviors over mean SNR, while Figures (b), (d) and (f) display time evolutions over 500 s.

the probability of a correct transmission occurring given the previous was correct $\Pr(\mathscr{C}_i|\mathscr{C}_{i-1})$ as a measure for the error-free bursts, and conversely the probability of a transmission failing given the previous failed $\Pr(\mathscr{E}_i|\mathscr{E}_{i-1})$ for error bursts. In contrast to the burst lengths, This statistic sees sufficient events for stochastic analysis within the stationarity period of the channel.

I use the MSE of an estimate $\hat{\boldsymbol{a}}$ as defined by

$$\mathrm{MSE}(\hat{\boldsymbol{a}}, \boldsymbol{a}) = \frac{1}{N}\sum_{i=1}^{N}(\hat{a}[i] - a[i])^2, \tag{4.35}$$

as performance measure. I furthermore investigate the Squared Error (SE) at instance i, defined as $\mathrm{SE}[i] = (\hat{a}[i] - a[i])^2$. Since I also reduced the burst lengths to probability estimates, I use the same performance measure, to make the quality of estimation comparable.

Die approbierte gedruckte Originalversion dieser Dissertation ist an der TU Wien Bibliothek verfügbar.
The approved original version of this doctoral thesis is available in print at TU Wien Bibliothek.
TU Bibliothek Your knowledge hub WIEN

Table 4.2: Statistical analysis of the squared error of various estimators.

Estimator	MSE	5%	95%	$\lvert\cdot\rvert^2 < 0.1$
Static PER estimate	0.0348	$8.22 \cdot 10^{-6}$	0.156	0.83
fading aware	0.0283	$2.88 \cdot 10^{-6}$	0.125	0.85
Mean SNR grouped	0.0367	$4.1 \cdot 10^{-6}$	0.169	0.81

4.5.1 PER Estimation Performance

Figure 4.7a shows the median of the estimated PER, of both the mean SNR grouped and the fading aware estimator compared to the measured PER, as a function of the mean SNR . The plot furthermore depicts the interval in which 90 % of all realizations lie for all three quantities. The figure shows that the fading aware estimator is able to model the mean PER, very well for small SNR values, while the mean SNR grouped estimator is slightly underestimating the PER, in the same range. Both are marginally overestimating the median PER, for large SNR values. I can also see that the fading aware estimator is able to model a moderate amount of spread for the PER, while the packet derived estimator has virtually no spread. This is due to the fact that the fading aware estimator adapts dynamically to the fade durations, while the packet derived estimator has a fixed parameter set for each SNR value. The same effect is shown in Fig. 4.7b, where the PER estimates are plotted over a stretch of time. There, the fading aware estimator is able to follow the short PER-spikes more consistently. Table 4.2 shows the evaluation of the two estimators with respect to the MSE compared to the reference PER estimator. The fading aware estimator outperforms all others on all accounts. Both mean and the percentile values are uniformly lower than any other estimator. Additionally, the SE of the estimator is 85 % of the time lower than 0.1, which is the largest fraction of the presented estimators. The mean SNR grouped estimator provides the worst MSE, although the overall analysis suggests performance not significantly worse than the mean SNR based estimation.

4.5.2 Burst Estimation Performance

I analyze burst lengths by looking at the probability of immediately repeating a success $\Pr(\mathscr{C}_i|\mathscr{C}_{i-1})$ or repeating a failure $\Pr(\mathscr{E}_i|\mathscr{E}_{i-1})$. These probabilities are shown in Fig. 4.7c and Fig. 4.7e as functions of time. Both show that errors are to some extent always bursty, since $\Pr(\mathscr{E}_i|\mathscr{E}_{i-1})$ stays consistently above 0.5, even for high SNR values. I can also see burst tendencies for $\Pr(\mathscr{C}_i|\mathscr{C}_{i-1})$, where the probability of a success given a success rises above 0.9 at 10 dB, while the overall PER at that value is still at 0.3. The figures show that the mean SNR grouped model is capable of modeling the burst characteristics very well in most of the SNR range. Some deviations exist in the low SNR range, and obvious artifacts in the very high SNR range have to be ignored. In that regime, comparatively few measurements were taken, therefore effects seen at single points in time had a greater impact on the parameter estimation. On the other hand, the fading aware model is strongly underestimating the burst lengths. In fact, the fading aware model aligns well with the lower bound of the 90 % interval of the original

Die approbierte gedruckte Originalversion dieser Dissertation ist an der TU Wien Bibliothek verfügbar.
The approved original version of this doctoral thesis is available in print at TU Wien Bibliothek.
TU Bibliothek Your knowledge hub WIEN

measurement. The dominant contribution to this behavior is the estimation of the two packet error curves. When comparing Fig. 4.5b to Fig. 4.4, I see the mean SNR grouped model to apply more extreme values for the error probabilities. $P_{\mathscr{E}}^{g}$ decreases much more quickly towards 0, while $P_{\mathscr{E}}^{b}$ is close to 1 for the whole SNR range. Remarkably, the prediction of the fading aware model is a very viable pessimistic estimate on the burst behavior, and as such also of interest. This behavior is clearly shown in the time sample given in Figs. 4.7d and 4.7f, where the fading aware estimator consistently underestimates the true values. Table 4.3, which lists

Table 4.3: MSE behavior of $\Pr(\mathscr{C}_i|\mathscr{C}_{i-1})$ and $\Pr(\mathscr{E}_i|\mathscr{E}_{i-1})$

$\Pr(\mathscr{C}_i\|\mathscr{C}_{i-1})$	MSE	5%	95%	$\|\cdot\|^2 < 0.1$
fading aware	0.0313	$9.41 \cdot 10^{-5}$	0.143	0.33
Mean SNR grouped	0.021	$4.6 \cdot 10^{-6}$	0.111	0.87
$\Pr(\mathscr{E}_i\|\mathscr{E}_{i-1})$	MSE	5%	95%	$\|\cdot\|^2 < 0.1$
fading aware	0.1	$2.9 \cdot 10^{-4}$	0.324	0.20
Mean SNR grouped	0.054	$4.6 \cdot 10^{-5}$	0.33	0.64

the MSE evaluation of the burst probabilities, also confirms this results. With respect to burst length modeling, the mean SNR grouped model is strongly outperforming the threshold-based model.

4.5.3 Discussion: Necessity of Burst Modeling

Finally, I evaluate the loss of information when only modeling static SNR to PER mapping, as is the current state of the art, with respect to the burst behavior. Assuming only estimating the first-order PER, the resulting channel is a Binary Erasure Channel (BEC) with a time varying erasure probability. In such a channel, packet transmission does not depend on the past, and therefore $P_{\text{BEC}}(\mathscr{C}_i|\mathscr{C}_{i-1})$ and $P_{\text{BEC}}(\mathscr{E}_i|\mathscr{E}_{i-1})$ simplify to

$$\begin{aligned} P_{\text{BEC}}(\mathscr{E}_i|\mathscr{E}_{i-1})[i] &= PER[i], \\ P_{\text{BEC}}(\mathscr{C}_i|\mathscr{C}_{i-1})[i] &= 1 - PER[i]. \end{aligned} \tag{4.36}$$

I now analyze this claim by using the measured PER itself as estimation basis. I denote the deviation of the measured values for $\Pr(\mathscr{C}_i|\mathscr{C}_{i-1})$ from the BEC estimate as $\Delta_c^{BEC} = P_{\text{BEC}}(\mathscr{C}_i|\mathscr{C}_{i-1}) - \Pr(\mathscr{C}_i|\mathscr{C}_{i-1})$, and the deviation of the measured values for $\Pr(\mathscr{E}_i|\mathscr{E}_{i-1})$ as $\Delta_{\mathscr{E}}^{BEC} = P_{\text{BEC}}(\mathscr{E}_i|\mathscr{E}_{i-1}) - \Pr(\mathscr{E}_i|\mathscr{E}_{i-1})$. Figure 4.8a shows a histogram of these values. If the channel were not bursty in nature, these histograms concentrate around 0. However, the results show a large dispersion for both parameters, indicating a violation of the BEC assumption. The peak at 0 is largely due to extreme cases where the PER was 0 or 1, thus resulting in unbroken bursts. Further evaluation shows an average $\Delta_{\mathscr{C}}^{BEC}$ of 0.136 and average $\Delta_{\mathscr{E}}^{BEC}$ of −0.33, demonstrating that there burstiness in both components is completely lost by pure PER estimation. Figures 4.8b

Die approbierte gedruckte Originalversion dieser Dissertation ist an der TU Wien Bibliothek verfügbar.
The approved original version of this doctoral thesis is available in print at TU Wien Bibliothek.
TU Bibliothek Your knowledge hub WIEN

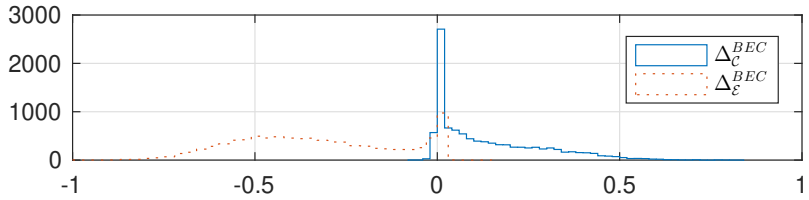

(a) $\Delta_{\mathscr{C}}$ and $\Delta_{\mathscr{E}}$ when only the PER is taken into account.

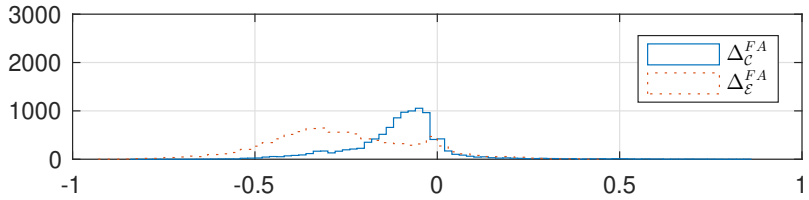

(b) $\Delta_{\mathscr{C}}$ and $\Delta_{\mathscr{E}}$ for the fading aware estimator.

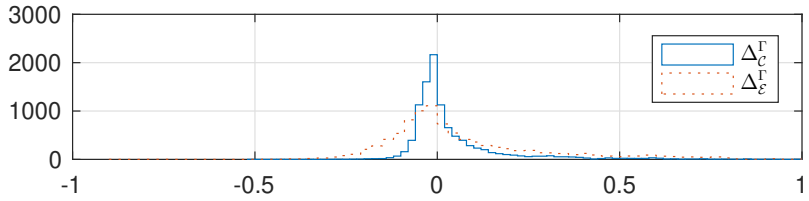

(c) $\Delta_{\mathscr{C}}$ and $\Delta_{\mathscr{E}}$ for the mean SNR grouped estimator.

Figure 4.8: Histograms for the burst-modeling capabilities of the fading aware and the mean SNR grouped estimators.

and 4.8c on the other hand depict the same histograms for the fading aware and the mean SNR grouped models. The fading aware model underestimates the bursts, with an average $\Delta_{\mathscr{E}}^{FA}$ of -2.6 and $\Delta_{\mathscr{C}}^{FA}$ of -0.1, although both are considerably better than not considering the bursts. The mean SNR grouped model provides the most accurate burst estimation, with the mean $\Delta_{\mathscr{C}}^{\Gamma}$ of 0.04 and mean $\Delta_{\mathscr{E}}^{\Gamma}$ of 0.06.

4.5.4 Discussion: Model Complexity

The execution cost for the presented model equals one SNR lookup to fetch the correct model parameters, two random events, two comparisons and one binary state per link (*good* or *bad*) with regards to modeling complexity. One binary state per link requires storage in the order of kilobytes even for large simulations, and thus negligible. Therefore, the simulation of packet loss is not even doubled in steps required compared to the typical model of static SNR to PER mapping.

Die approbierte gedruckte Originalversion dieser Dissertation ist an der TU Wien Bibliothek verfügbar.
The approved original version of this doctoral thesis is available in print at TU Wien Bibliothek.
TU Bibliothek Your knowledge hub WIEN

4.6 Combining Network Effects and Channel Effects

At this point, I want to provide a combined result for the decomposition of the Eq. (3.3), given as

$$\Pr(\mathscr{E}_{\text{total}}) = 1 - \Big(1 - \Pr(\mathscr{E}|\mathscr{H}[i])\Big)\Big(1 - \Pr(\mathscr{E}|\mathscr{N}[i])\Big). \tag{4.37}$$

I base this application on the Gilbert-Elliott-model for the channel modeling, and model the interference via network simulations. However, the overall approach can be adapted to other data sources.

The observed interference pattern crucially depends on the traffic density and street layout. To account for this, the mobility simulations and network simulations are combined to generate interference patterns that are accurate for the given use case. I use the microscopic traffic simulator TraffSim [86, 103] to generate highway traffic traces at high density. The coordinates from this are then used as node positions for OMNET++ VEINS simulations [104, 105]. I set the communication distance to 350 m and ensured that packet loss only happened due to interference to isolate this behavior. The resulting packet losses are shown in the results section.

I use two tools for employing the classification, and apply the tools to both modeling aspects. First, the information bottleneck method [98] reduces the modeling complexity in an adjustable fashion while retaining as much information as possible. Afterwards, I use the AIC [49] to evaluate what model complexity features the optimal trade-off between simplicity and accuracy.

4.6.1 The Information Bottleneck

Consider two random variables α and γ. If they are not statistically independent, the dependence of α on γ is given by the conditional probabilities $\Pr(\alpha|\gamma)$. However, the strength of the correlation between α and γ may be vastly different for different values of γ. In the interest of reducing complexity, I now want to replace the (possibly continuous) variable γ with a quantized version $\tilde{\gamma}$ of reduced complexity. Specifically, the goal is to quantize the variable γ, which can assume any value on the set $\gamma \in \Gamma$ into Q intervals. I want to choose this set of Q intervals $\tilde{\Gamma}$ in such a way that the maximum information about α is retained with the side constraint that exactly Q intervals are used.

The variables of interest are the performance metrics $\Pr(\mathscr{E})$, $\Pr(\mathscr{E}_i|\mathscr{E}_{i-1})$ and $\Pr(\mathscr{C}_i|\mathscr{C}_{i-1})$. Fig. 4.9 shows an example of the idea. I have $\Pr(\mathscr{E})$, and as parameter γ the SNR is used. In the range between 5 and 15 decibels, strong changes of $\Pr(\mathscr{E})$ in dependence of the SNR are observed. Outside that region, the correlation is very weak. The figure demonstrates the quantization idea with 2 different number of intervals. In both cases, large intervals are

Die approbierte gedruckte Originalversion dieser Dissertation ist an der TU Wien Bibliothek verfügbar.
The approved original version of this doctoral thesis is available in print at TU Wien Bibliothek.
TU Bibliothek Your knowledge hub WIEN

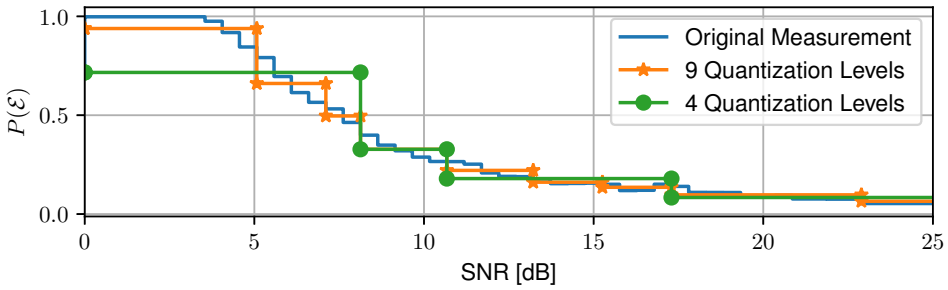

Figure 4.9: $\Pr(\mathscr{E})$ estimation for SNR quantization into 4 and 9 intervals.

assigned to regions that show weak correlation, while strong correlation regions are finely quantized.

Mathematically, the pmf conditioned on $\tilde{\gamma}$ $p(\Pr(\mathscr{E})|\tilde{\gamma})$ is to be as close as possible to the original conditionals $p(\Pr(\mathscr{E})|\gamma)$, which is equivalent to demanding that the mutual information $I(\Pr(\mathscr{E});\tilde{\Gamma})$ is to be maximal for a given quantization $\tilde{\Gamma}$. Finding the optimal quantization while maximizing this mutual information is called the information bottleneck [98] and is described via Lagrangian multipliers as

$$\tilde{\Gamma}_{\text{opt}} = \arg\min_{\tilde{\Gamma}} \mathscr{L}[p(\tilde{\gamma}|\gamma)] = \arg\min_{\tilde{\Gamma}} I(\Gamma;\tilde{\Gamma}) - \beta I(\tilde{\Gamma};\Pr(\mathscr{E})). \tag{4.38}$$

Here, $p(\tilde{\gamma}|\gamma)$ is the conditional probability density function (pdf). Slonim *et al.* presented the *agglomerative bottleneck*, which is a greedy algorithm that starts with N partitions and sequentially merges two partitions until only Q partitions are left [106]. This is done in a locally optimal manner that ensures that at every merge step, the currently optimal 2 regions are merged. The key to this approach is the fact that the merge of the SNR intervals γ_i and γ_j reduces $I(\tilde{\Gamma};\Pr(\mathscr{E}))$ by

$$d_{i,j}(\Pr(\mathscr{E})) = (p(\gamma_i) + p(\gamma_j))\, JS_{\Pi_2}[p(\Pr(\mathscr{E})|\gamma_i), p(\Pr(\mathscr{E})|\gamma_j)], \tag{4.39}$$

where JS_{Π_2} is the Jensen-Shannon divergence resulting from merging the two pdfs [107]. The Jensen-Shannon divergence is a measure for the similarity of two distributions that extends the concepts of the Kullback-Leibler divergence [100].

However, the goal is to choose the intervals in such a way that I retain the optimal modeling of the $\Pr(\mathscr{E})$ as well as the burst probabilities. Hence, I want to consider all three variables $\Pr(\mathscr{E})$,

Die approbierte gedruckte Originalversion dieser Dissertation ist an der TU Wien Bibliothek verfügbar.
The approved original version of this doctoral thesis is available in print at TU Wien Bibliothek.
TU Bibliothek Your knowledge hub WIEN

$\Pr(\mathscr{E}_i|\mathscr{E}_{i-1})$ and $\Pr(\mathscr{C}_i|\mathscr{C}_{i-1})$ in the optimization. I do this analogous to [108] by introducing a new objective function, the multi-feature (m-f) objective function

$$\mathscr{L}_{m-f} = I(\Gamma;\tilde{\Gamma}) - \beta \underbrace{\sum_{k=1}^{K} \lambda_k I(Y^k;\tilde{\Gamma})}_{T(\mathbf{Y},\lambda,\Gamma)}. \tag{4.40}$$

Here, I consider K relevant variables, Y^k represents the kth *relevance variable*, and λ_k is a weighting factor for the kth variable with $\sum\lambda = 1$. In this case $K = 3$, $Y^1 = \Pr(\mathscr{E})$, $Y^2 = \Pr(\mathscr{E}_i|\mathscr{E}_{i-1})$ and $Y^3 = \Pr(\mathscr{C}_i|\mathscr{C}_{i-1})$. Therefore, $T(\mathbf{Y},\lambda,\Gamma)$ represents a weighted average mutual information between the quantized SNR and the different relevance variables. For now, I do not specify the weighting factors λ.

The agglomerative bottleneck shows that $I(Y^k;\tilde{\Gamma})$ is reduced by $d_{i,j}(Y^k)$ if the clusters i and j are merged. As seen in Eq. (4.40), the single mutual information terms do not depend on each other. Thus, when merging the ith and jth SNR interval, the function $T(\mathbf{Y},\lambda,\Gamma)$ is in total reduced by

$$D_{i,j}(\mathbf{Y},\lambda) = \sum_{k=1}^{K} \lambda_k d_{i,j}(Y^k) \tag{4.41}$$

I apply the regular agglomerative information bottleneck algorithm to optimize (Eq. (4.40)), by optimizing with respect to $D_{i,j}$ instead of $d_{i,j}$. The quantization depends on the choice of the weighting coefficients λ_k.

4.6.2 Resulting Highway Scenarios

In the forthcoming sections I discuss the resulting scenario classifications. I first introduce the base data, on which the results are based. Then, I show the quantizations for the respective models.

Table 4.4: Measurement parameters

Bitrate	6 Mbps
Modulation/Coding	QPSK, Rate 1/2
Packet length	500 Bytes
Mean packet rate	970 s^{-1}
Transmit power	10 dBm

The scenario used in this contribution represents a typical highway setup with multiple lanes and an on-ramp serving as a potential bottleneck, as illustrated in Fig. 4.10. The considered road stretch is 12 km long, and the on-ramp is located at kilometer six, followed by a lane narrowing at kilometer seven. The inflows on the through lanes and the on-ramp are set to

Die approbierte gedruckte Originalversion dieser Dissertation ist an der TU Wien Bibliothek verfügbar.
The approved original version of this doctoral thesis is available in print at TU Wien Bibliothek.
TU Bibliothek Your knowledge hub WIEN

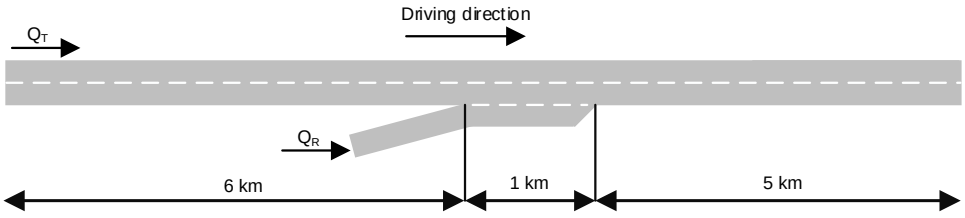

Figure 4.10: Schematic illustration of the simulated highway scenario.

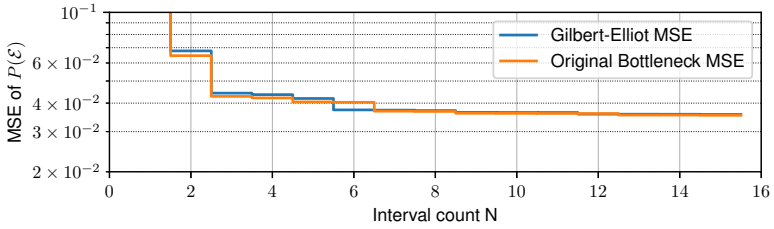

Figure 4.11: Gilbert-Elliott MSE and AIC as function of SNR interval count M.

$QT = 2200$ veh/h and $QR = 320$ veh/h, respectively, resulting in dense and congested traffic at the network's bottleneck. I use the microscopic traffic simulator TraffSim [86] to simulate one hour of driving, and apply the widely recognized IDM [109] and the MOBIL model [110] to simulate the longitudinal and lateral vehicle dynamics, respectively. For all vehicles in the simulation comprehensive trajectory data, that is their positions, speeds, and accelerations, are recorded at a temporal resolution of $10\,s^{-1}$. The location traces obtained thereof serve as input into the VEINS framework for OMNET++, which allows transmitting packets according to Table 4.5. Here, the parameters are set to typical data for periodic broadcast information that acts as basic announcement of cooperation awareness Base Safety Message (BSM).

Table 4.5: System Level Simulation Parameters

VEINS Parameters	Value
Message type	BSM
Packet Size	500
Message frequency [s^{-1}]	10
MCS	QPSK, Rate 1/2

4.6.3 Results

Point-to-Point Model

Analysis of the point-to-point PER is shown in Fig. 4.11. The figure shows the achieved MSE and AIC as a function of the number of intervals used for the SNR range. The MSE plot shows

Die approbierte gedruckte Originalversion dieser Dissertation ist an der TU Wien Bibliothek verfügbar.
The approved original version of this doctoral thesis is available in print at TU Wien Bibliothek.
TU Bibliothek Your knowledge hub WIEN

Table 4.6: Gilbert-Elliott parameters for 6 intervals.

Nr.	Start SNR	End SNR	P_{BG}	P_e^g	P_{GB}	P_e^b
1	-∞	5.072	0.014	0.337	0.080	0.980
2	5.072	7.108	0.033	0.129	0.054	0.945
3	7.108	9.657	0.046	0.046	0.033	0.896
4	9.657	12.203	0.062	0.019	0.023	0.845
5	12.203	16.786	0.065	0.011	0.015	0.783
6	16.786	∞	0.054	0.005	0.006	0.759

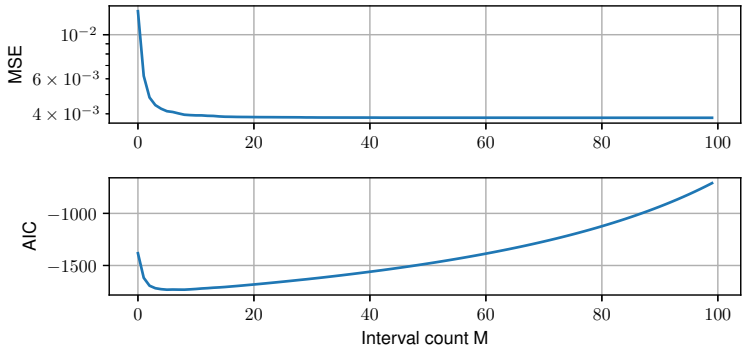

Figure 4.12: Interference MSE as a function of interval count M.

already that the modeling performance gains start to diminish beyond 6 to 8 SNR intervals. However, the AIC shows directly that the optimal trade-off between model order and modeling accuracy is with an interval count of $N = 6$. The resulting Gilbert-Elliott parameters, as well as the SNR boundaries for the intervals are shown in Table 4.6. The results show that the region between 5 and 12 decibels is highly resolved, as the performance changes the strongest within that region.

Interference Modeling

Figure 4.12 shows MSE and AIC for different numbers of interferer grouping intervals. Again, the plots show that in terms of the AIC, a total number of 6 intervals is optimal for this scenario. The plot shows a similar trend of drastic saturation of the MSE if the number of intervals is increased further. The packet error distributions for the optimal 6 intervals are shown in Fig. 4.13. Figure 4.13a shows the histograms of achieved PER due to interference for the 6 resulting intervals, as well as truncated Normal distribution fits. Figure 4.13b shows the parameters of the truncated Normal fits over numbers of neighbors. The same parameters are shown in table form in Table 4.7.

Die approbierte gedruckte Originalversion dieser Dissertation ist an der TU Wien Bibliothek verfügbar.
The approved original version of this doctoral thesis is available in print at TU Wien Bibliothek.
TU Bibliothek Your knowledge hub WIEN

Table 4.7: Interference parameters for Gaussian Fits of 6 intervals.

Nr.	Min Nr. Neighbors	Max Nr. Neighbors	μ	σ
1	0	31.0	0.143	0.069
2	47.0	87.0	0.189	0.070
3	87.0	105.0	0.273	0.051
4	105.0	121.0	0.332	0.040
5	121.0	133.0	0.404	0.035
6	133.0	∞	0.493	0.039

Die approbierte gedruckte Originalversion dieser Dissertation ist an der TU Wien Bibliothek verfügbar.
The approved original version of this doctoral thesis is available in print at TU Wien Bibliothek.

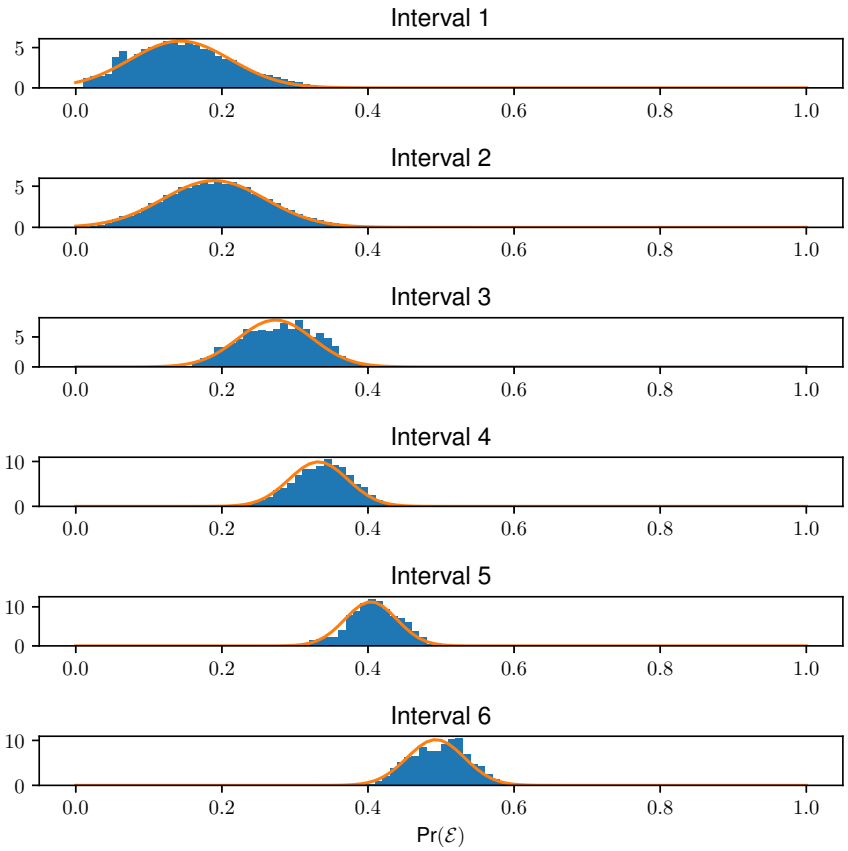

(a) Histograms of error probability due to interference.

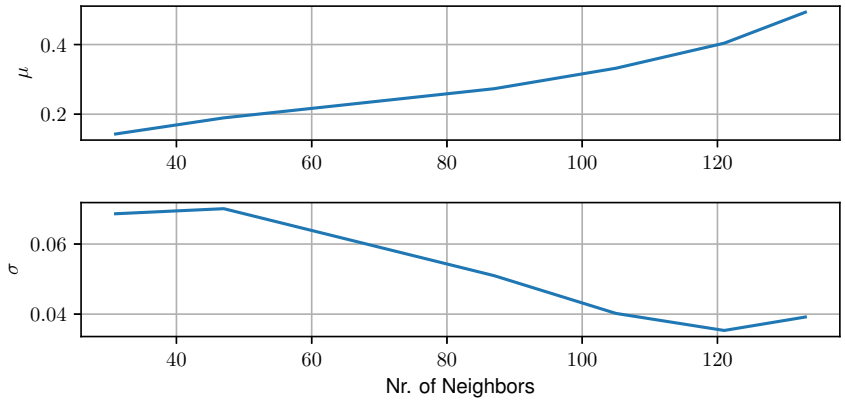

(b) Mean and standard deviation of Gaussian fits.

Figure 4.13: Resulting pdfs of the optimal intervals.

Die approbierte gedruckte Originalversion dieser Dissertation ist an der TU Wien Bibliothek verfügbar.
The approved original version of this doctoral thesis is available in print at TU Wien Bibliothek.

4.6.4 Total Resulting Packet Error Probabilities

Finally, I analyze the result of Eq. (4.37), by looking at the total resulting error probability. The error probability is shown in Fig. 4.14 and provides indication that for low SNR , SNR dominates the error probability, while for high SNRs, the interferer count dominates. However, there is also a noticeable range between 7 to 12.5 dB SNR and 40 to 80 vehicles where both parameters have comparable impact on the achievable performance.

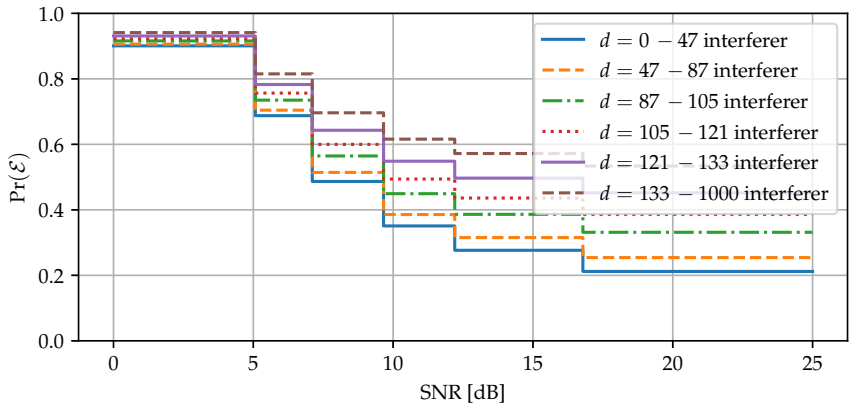

Figure 4.14: Total Pr($\mathscr{E}$) as function of SNR and Nr. of interferers.

4.7 Discussion

The results show that the scenario of dense highway traffic is classified based on the number of interferers and the achievable SNR . I present a modeling approach that provides each process with its own stochastic model that aims at replicating the underlying process at manageable complexity. A combination of the information bottleneck and the AIC shows that both models find an optimal trade-off between complexity and accuracy for 6 distinct parameter sets. Hence, I define 36 combinations of received SNR and numbers of neighbors for a combined analysis incorporating fading modeling and interference. These results demonstrate that while sometimes one parameter dominates and the other becomes irrelevant, for other parameter choices both contribute equally. It is thus vital to consider both when modeling and simulating V2X communications.

Die approbierte gedruckte Originalversion dieser Dissertation ist an der TU Wien Bibliothek verfügbar.
The approved original version of this doctoral thesis is available in print at TU Wien Bibliothek.
TU Bibliothek Your knowledge hub WIEN

Die approbierte gedruckte Originalversion dieser Dissertation ist an der TU Wien Bibliothek verfügbar.
The approved original version of this doctoral thesis is available in print at TU Wien Bibliothek.

5 Conclusions

Capturing the essential aspects of vehicular communications is a fool's errand. Much depends on the specific channel scenario, the chosen protocol, the chosen hardware, the antenna placement, and similar aspects. This is often portrayed as conventional wisdom and provided as argument why only small fractions of the communication chain are considered in a single analysis.

In this thesis, I demonstrate that the topic can still be tackled in a holistic manner, provided one is aware of the pitfalls. My approach is guided by parsimony, sparsity and simplicity at all design steps. Otherwise, the model complexity explodes right away. However, if proper care is taken to keep overall complexity feasible, important conclusions are provided by not just by the individual partial analyses, but also by their interlinking results.

The main tools to introduce sparsity used in this thesis are the information bottleneck and the c-LASSO. The information bottleneck allows clustering of random data according to estimates of the pdfs, while the c-LASSO finds sparse solutions in a deterministic mapping. Applying these tools to vehicular channel measurements shows that sparse channel models provide a great basis for channel estimation. Four to six multipath components usually provide an optimal trade-off between simplicity and accuracy. This indicates that sparsity enforcing measures, such as the AIC, are of high importance for channel modeling approaches. Otherwise, a tendency to overfit the problem often arises. I furthermore showed that by restricting the emulation bandwidth, one ensures that scatterer clusters are collapsed into one tap, leading to sparser overall models. Even when parallelizing this approach to estimate the full bandwidth, subband fitting outperforms regular delay line fitting due to the geometrical arguments. Similar statements are drawn from the two-dimensional delay-Doppler fitting approach. The results furthermore show that low-complexity stationary channel models are adequate at representing the communication challenge for a given timeframe. This holds true especially in applications where the emulation can be narrow-band, such as when the emulator output is bandpass-filtered by the receiver.

Die approbierte gedruckte Originalversion dieser Dissertation ist an der TU Wien Bibliothek verfügbar.
The approved original version of this doctoral thesis is available in print at TU Wien Bibliothek.
TU Bibliothek Your knowledge hub WIEN

Measuring the packet error probability by means of channel emulation further yielded important results. First and foremost, the results depend strongly on the investigated scenario, as well as the packet length. This confirms the assumptions, and shows that these aspects must not be left unattended when doing system level analysis. Stationary channel models are also a good way to tune the challenge in benchmarking of hardware. The results also show that network analysis can't always simplify at the physical layer, and keep the network layer complete. Sometimes, more representative results are obtained by simplifying the network, and considering all layers on a simplified network structure. In such an approach the interferer patterns deviate from the actual patterns. However, if done carefully, the patterns still show the same statistical properties, meaning that the network is representative of the original one. In this way, the reduced complexity allows investing in fully modeling the physical layer, meaning that overall the modeling accuracy has increased. This approach works well for the scenario presented in this thesis. The data clearly demonstrates that for ad-hoc schemes, it is vital that channel congestion is to be avoided, since interference deteriorates the communication performance quickly and severely.

Having obtained these estimates, I show that it is possible to provide single-link models that incorporate both propagation conditions as well as interference models. These have to be drawn from measurements or simulations, and fitted to apply to the stochastic model. I demonstrated that a Gilbert-Elliott model is sufficient to model the burst properties of the communication channel. I also showed that a model that uses 5 SNR intervals, as well as 8 different settings for numbers of neighbors is optimal in complexity for modeling communication performance on a dense highway.

The analysis shows that the actual packet error performance is sensitive both to single-link conditions and the network effects. Therefore, channel modeling, estimation and networking needs to be considered when modeling vehicular communications. Only with a good grasp on the specific operating domain of a scenario, careful simplifications can be taken without losing information.

These different layers allow to be interconnected, and may even be cooperatively treated, when considering the problem of vehicular communications. By considering consistently simple approaches, I was able to distill the essential aspects of each component. This thesis worked with specific scenarios and protocols, but I am convinced that the developed tools, and the general approach can be adapted to new challenges. I hope that by providing this tool set, more accurate holistic approaches can be developed.

The next goal is to perform a similar analysis for LTE-V2V based communications. Much of the thesis' steps can be reused in such a scenario, with only the graph reduction algorithm exploiting the properties of IEEE 802.11p specifically. Further investigation of traffic scenarios, as well as channel scenarios also provide more coverage for the results.

Die approbierte gedruckte Originalversion dieser Dissertation ist an der TU Wien Bibliothek verfügbar.
The approved original version of this doctoral thesis is available in print at TU Wien Bibliothek.
TU Bibliothek Your knowledge hub WIEN

A 5.6 GHz Channel Estimation

Die approbierte gedruckte Originalversion dieser Dissertation ist an der TU Wien Bibliothek verfügbar.
The approved original version of this doctoral thesis is available in print at TU Wien Bibliothek.

I applied the algorithm presented in Chapter 2 further to a measurement from a different channel sounding campaign. That campaign was conducted with omnidirectional antennas at 5.6 GHz, which is more representative for conventional protocols. The investigated scenario

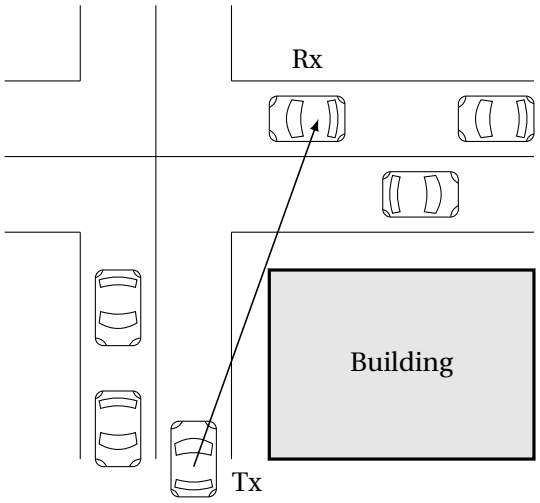

Figure A.1: Urban crossing channel scenario.

of the measurement is illustrated in Fig. A.1. In this section, I present results for memoryless estimation with and without subband fitting.

A.1 Channel Sounding Campaign

The measurements were taken in 2009 as part of the DRIVEWAY measurement campaign [84]. I chose a road crossing scenario, where transmitting and receiving vehicle both approach the road crossing, as depicted in Fig. A.1. The relevant parameters of the channel sounder measurement are given in Table A.1. Figure A.2 shows the channel sounder data for the given

Table A.1: Measurement Parameters

Center frequency [GHz]	5.6
Measurement bandwidth [MHz]	240
Transmit power [dBm]	27
Test signal length [μs]	3.2
Snapshot repetition time [μs]	307.2
Recording time [s]	10
Speed Tx [km/h]	10 – 20
Speed Rx [km/h]	30

measurement scenario. As is shown, for 7 seconds, the received power was low, and only afterwards, a noticeable power was detected.

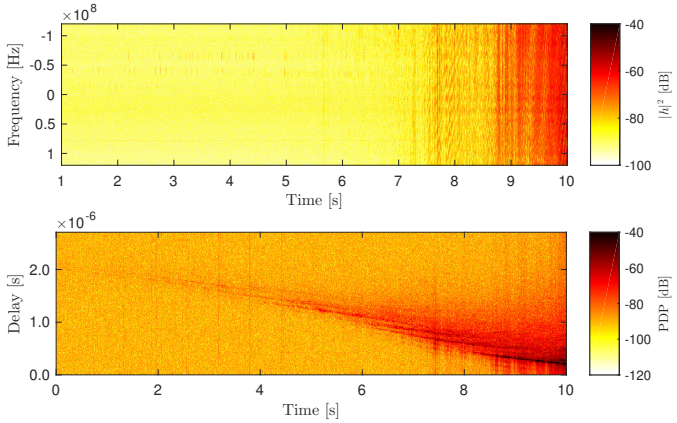

Figure A.2: Channel sounder results.

A.2 Estimation Results

An exemplary fit with 10-taps is shown in Fig. A.3. The 10-tap fit is already very well suited to estimate the measurement. Specific performance evaluation for four different timestamps in the measurement is shown in Fig. A.4. There are multiple aspects of note here. First, the MSE decreases with progressive time, due to the stronger received signal resulting in better SNR. The results further show that subband fitting also works very well with this trace, with $P = 4$ fits being uniformly the best estimates for a given model order. The analysis shows that for the early timesteps, the AIC indicates that the optimal model order is between 16 and 24, depending on the exact fit. Considering the fact that $M = 24$ means that $K_0 = 6$ for $P = 4$, I am still seeing a relatively sparse channel. But even for the high-SNR fits, $K_0 \approx 8$ results in high-quality fits for $P = 4$. Thus, this measurement also shows that a channel with only a relatively small amount of relevant clusters is observed. The fact that the number is higher

Die approbierte gedruckte Originalversion dieser Dissertation ist an der TU Wien Bibliothek verfügbar.
The approved original version of this doctoral thesis is available in print at TU Wien Bibliothek.

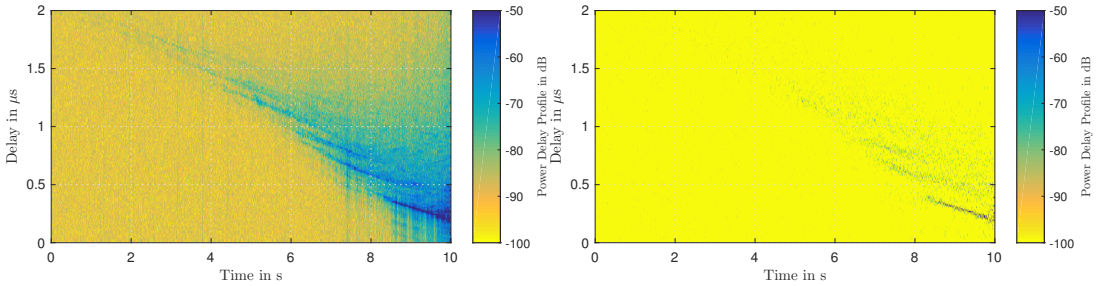

(a) Time-variant PDP of measured channel in urban crossing scenario.

(b) 10-tap fit of the given PDP.

Figure A.3: Measured PDP and 10-tap LASSO fit (c.f. [51]).

than for mmWave measurements is strongly related to the spatial filtering characteristics of mmWave measurements.

Die approbierte gedruckte Originalversion dieser Dissertation ist an der TU Wien Bibliothek verfügbar.
The approved original version of this doctoral thesis is available in print at TU Wien Bibliothek.

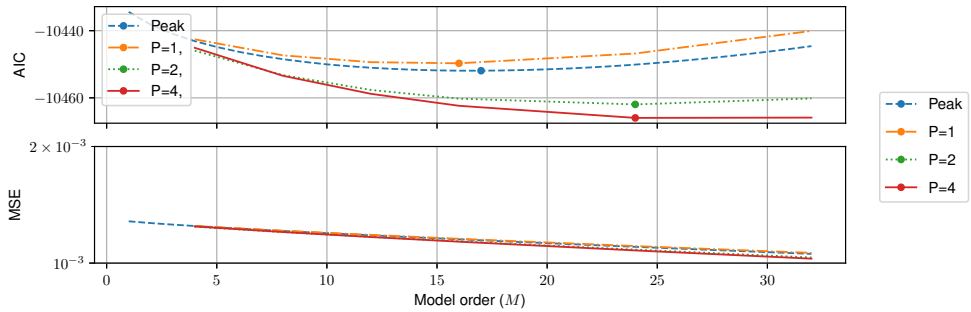

(a) Estimation quality at 2 s.

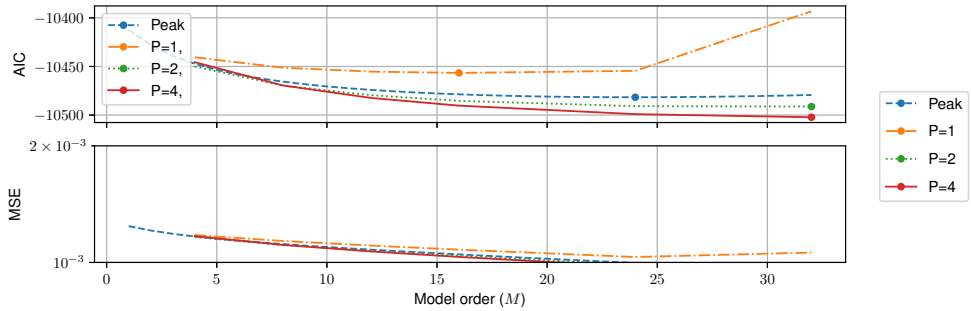

(b) Estimation quality at 4.5 s.

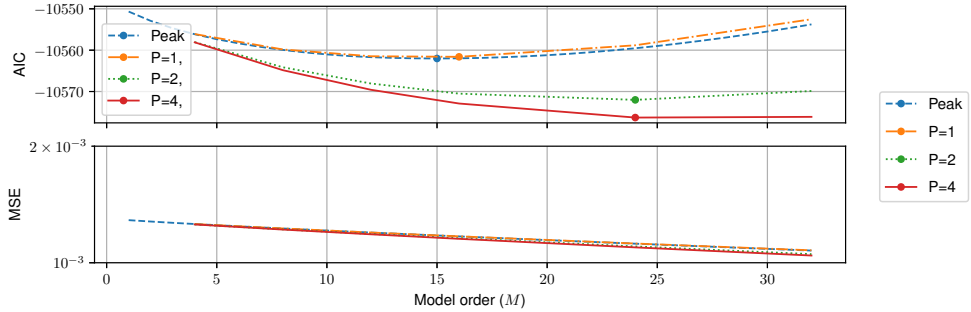

(c) Estimation quality at 7 s.

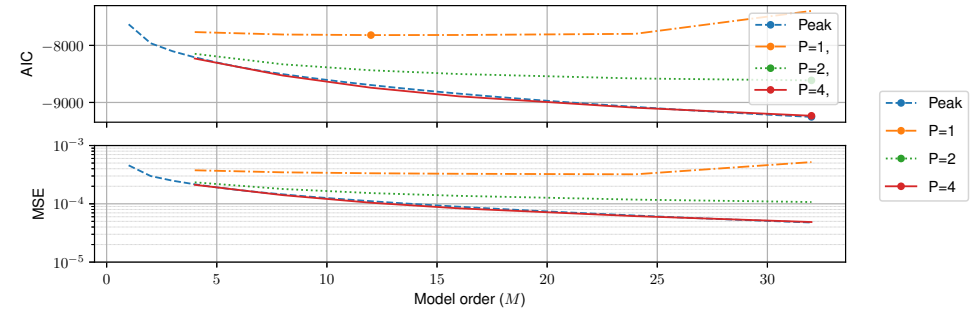

(d) Estimation quality at 9.5 s.

Figure A.4: MSE and AIC of the analyzed measurements (**(a)–(d)**).

Die approbierte gedruckte Originalversion dieser Dissertation ist an der TU Wien Bibliothek verfügbar.
The approved original version of this doctoral thesis is available in print at TU Wien Bibliothek.
TU Bibliothek Your knowledge hub WIEN

B Real-Time Emulator Design

Die approbierte gedruckte Originalversion dieser Dissertation ist an der TU Wien Bibliothek verfügbar.
The approved original version of this doctoral thesis is available in print at TU Wien Bibliothek.

Since time-variant convolution is the module which performs the real-time calculation in the FPGA, its architecture is the key to achieving the trade off between complexity and accuracy. The first option is to implement the most general from of convolution by calculation of the discrete version of Eq. (2.1). This architecture is capable of emulating any linear time-varying channel response by simple operations: complex number multiplication and additions

$$r[m] = \sum_{p=1}^{P} C_p[m]s[m-d_p]. \tag{B.1}$$

Here, $\tau_p = d_p T_s$, therefore d_p is the number of samples that a tap is offset. The drawback is that the rate of update of C_ps is determined by the necessary rate for accurate modeling of $e^{j2\pi\nu_p t}$ elements. This rate may become too high to stream to FPGAs in typical SDRs.

For this reason, a tapped-delay line architecture is implemented where each tap is parameterized by its delay, weighted in magnitude, and phase-rotated. The Doppler shift associated with a tap is explicitly parameterized which significantly reduces the required update rate for the channel parameters. Due to the time-discrete nature of the FPGA implementation, the architecture realizes only discrete delays, and assumes that delay lags are on the sampling grid: hence, the MPC delay lags which are off-grid are approximated by shifting them to one of the neighboring on-grid delay (In a future extension of this work, fractional delays are foreseen as well).

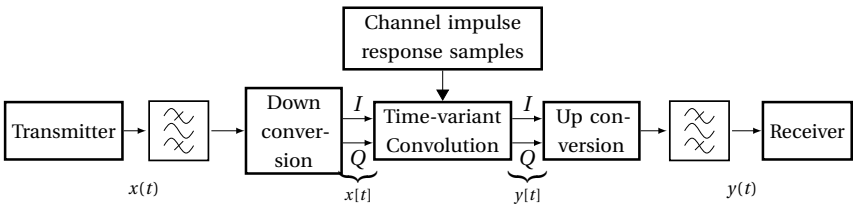

Figure B.1: System view of the emulator.

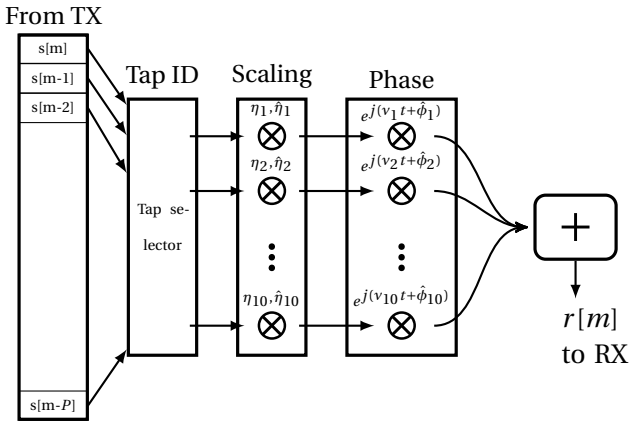

Figure B.2: Tapped-delay architecture for time-variant convolution.

The architecture shown in Fig. B.1 implements this tapped-delay line architecture restricted to on-grid delays according to the time-discrete approximation,

$$r[m] = \sum_{p=1}^{P} \eta_p \hat{\eta}_p \mathrm{e}^{j2\pi(\nu_p m T_s + \hat{\phi}_p)} s[m - d_p]. \tag{B.2}$$

The FPGA implementation follows the architecture in Fig. B.2 implementing Eq. (B.2). In each vehicular scenario snapshot, for each active tap, the index determines the relevant equalized delay which then is passed on to the FPGA along with four other parameters: η_p and $\hat{\eta}_p$ which represent the deterministic and stochastic pathloss components, along with ν_p and $\hat{\phi}_p(t)$ which represent the Doppler shift and the phase shift components for the selected tap. η_p and ν are slowly varying factors while $\hat{\eta}$ and $\hat{\phi}$ model the fast-varying behavior of the coefficients which are passed on through high speed DMA FIFO structures.

As for implementation of the real-time delays, this architecture relies on a shift-and-discard array structure in order to store the delayed input samples at equally sampled delay taps, rather than implementing the time-delay operation on the FPGA. At each instance of the FPGA clock, the new sample from emulator input arrives and the stored samples are shifted in the array. To perform the emulation, according to the delays of the taps in the channel model, the samples of the input data from the array are selected and then scaled by pathloss factor and rotated by corresponding Doppler/phase shifts. To keep the gate count of the FPGA in limits, the frequency and phase shift operation as well as the IQ additions and multiplications are implemented by a low complexity algorithm. The input $s[m]$and output $r[m]$ samples are complex numbers relating to inphase (I) and quadrature (Q) components. In the implementation, the system is designed to have a bandwidth of 20 MHz which relates to 40 MS/s and 25 ns of sampling time. In order to cover the contributions of the reflectors which are 0.5 km away from the transceiver, a total of 68 taps with delay resolution of 25 ns is dedicated from which a maximum of 10 taps may be active simultaneously. The impulse response samples are passed on to the emulator by the host PC as depicted in Fig. B.1.

Die approbierte gedruckte Originalversion dieser Dissertation ist an der TU Wien Bibliothek verfügbar.
The approved original version of this doctoral thesis is available in print at TU Wien Bibliothek.
TU Bibliothek Your knowledge hub WIEN

C Stationary Channel Models

C.1 Fading Trace Generation

I generate a small-scale fading trace for each tap individually. Since the models employ stationary processes with Rayleigh statistics, I assume the fading trace to be complex valued, with both real and imaginary parts distributed Gaussian with zero mean, which does not change under linear combination of such variables. I achieve the given half-bathtub shape in a two-step process. First I generate a process conforming with the usual Jakes' bathtub shape [111]. Such a process consists of circular symmetric Gaussian noise $H_i \sim \mathscr{CN}(0,1)$ with mean 0 and variance 1, with a filter $\boldsymbol{w}$ that fulfills these equations

$$S_{H_i}(f) = 1, \tag{C.1}$$

$$\boldsymbol{h}_i' = \boldsymbol{h}_i * \boldsymbol{w}, \tag{C.2}$$

$$S_{H_i'}(f) = \frac{1}{\pi f_{i,d}\sqrt{1-\left(\frac{f}{f_{i,d}}\right)^2}} u(f_{i,d}-|f|), \tag{C.3}$$

where $u(\cdot)$ denotes the unit step, $*$ the discrete convolution, $S_{H_i}(f)$ the PSD of the stochastic process H_i, and $\boldsymbol{h}_i$ a realization of that process of length M. Boldface symbols denote matrices, where lowercase symbols have dimension $N \times 1$ and uppercase $N \times N$.

I generate such a correlated noise sequence directly, using a variant of the *sum-of-sinusoids* algorithm presented in [91]. In the second step, I want to ensure the PSD is half-sided, which is equivalent to making the signal discrete-time *analytic* [112]. This is done using a discrete-time Hilbert transform [113]

$$\boldsymbol{h}_{i,RS}' = \boldsymbol{F}^H\left(\mathbf{g} \odot (\boldsymbol{F}\boldsymbol{h}_i')\right), \tag{C.4}$$

$$\boldsymbol{h}_{i,LS}' = \left[\boldsymbol{F}^H\left(\mathbf{g} \odot (\boldsymbol{F}\boldsymbol{h}_i')\right)\right]^*, \tag{C.5}$$

$$\mathbf{g} = \frac{1}{\sqrt{2}}[1, \underbrace{2,\ldots,2}_{M/2-1}, 1, \underbrace{0,\ldots,0}_{M/2-1}]^T. \tag{C.6}$$

Die approbierte gedruckte Originalversion dieser Dissertation ist an der TU Wien Bibliothek verfügbar.
The approved original version of this doctoral thesis is available in print at TU Wien Bibliothek.
TU Bibliothek Your knowledge hub WIEN

Here, $\boldsymbol{F}$ describes the unitary DFT matrix of size $M \times M$, $\mathbf{g}$ is the transfer function resulting in the Hilbert transform, normalized so the total transform remains unitary, and $\odot$ denotes the element-wise multiplication. This implements a circular convolution of $\boldsymbol{h}'_i$ with the impulse response corresponding to $\boldsymbol{g}$. The second line shows that a left-sided spectrum is achieved by taking the complex conjugate of the result.

Thus, I obtain the required half-bathtub shapes from a standard Jakes' trace, as shown for a chosen parameter set in Fig. 3.6. The half-sided spectrum concentrates the signal energy in half the frequency space, and therefore sees a 3 dB rise when compared to the original Jakes' spectrum. The resulting signal statistic still adheres to the Rayleigh distribution as can be seen through the Empirical Cumulative Distribution Functions (ECDFs) of the trace magnitudes ($|h_i|$) and phases ($\phi_i = \arg(h_i)$) compared to a Rayleigh Cumulative Distribution Function (CDF) in Fig. C.1.

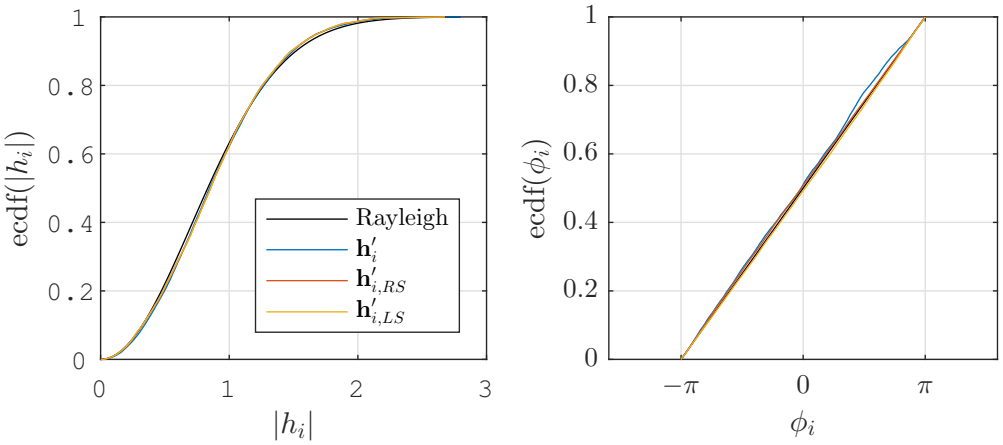

Figure C.1: Comparison of ECDFs of a Rayleigh distribution, and the magnitudes and phases of $\boldsymbol{h}'_i$, $\boldsymbol{h}'_{i,RS}$ and $\boldsymbol{h}'_{i,LS}$.

C.2 Tapped Delay Line Models

I model the channel using a tapped delay line, defined by the number of taps N, the deterministic parameters τ_i and η_i for every tap, and the stochastic characterization of the fading processes H_i. The used channel models, listed in Table C.1, encompass 5 scenarios. The chosen scenarios were selected to represent a wide range of important characteristic communication setups. Rural LOS is given as baseline, and behaves almost AWGN-like. This model is meant as comparison for the other models. The other models tackle the two extreme challenges for vehicles, high relative velocities and dense scattering environments. The former is represented by the Highway scenarios, and distinguishes LOS and NLOS models, that differ in the relative power of the scattering paths. The latter scenario is captured in the Urban models. Since Urban traffic setups are heterogeneous, two situations were picked that are of critical importance. Two cars approaching each other on the same street represent a LOS scenario,

Die approbierte gedruckte Originalversion dieser Dissertation ist an der TU Wien Bibliothek verfügbar.
The approved original version of this doctoral thesis is available in print at TU Wien Bibliothek.
TU Bibliothek Your knowledge hub WIEN

Table C.1: Link Level Channel Models

ETSI Draft	Tap	η_i^2 [dB]	τ_i [ns]	$f_{i,d}$ [Hz]	Profile
Rural LOS	$i=1$	0	0	0	Static
	$i=2$	−14	83	492	HalfBT
	$i=3$	−17	183	−295	HalfBT
Urban approaching LOS	$i=1$	0	0	0	Static
	$i=2$	−8	117	236	HalfBT
	$i=3$	−10	183	−157	HalfBT
	$i=4$	−15	333	492	HalfBT
Urban crossing NLOS	$i=1$	0	0	0	Static
	$i=2$	−3	267	295	HalfBT
	$i=3$	−4	400	−98	HalfBT
	$i=4$	−10	533	591	HalfBT
Highway LOS	$i=1$	0	0	0	Static
	$i=2$	−10	100	689	HalfBT
	$i=3$	−15	167	−492	HalfBT
	$i=4$	−20	500	886	HalfBT
Highway NLOS	$i=1$	0	0	0	Static
	$i=2$	−2	200	689	HalfBT
	$i=3$	−5	433	−492	HalfBT
	$i=4$	−7	700	886	HalfBT

while the NLOS setup is described by two cars approaching the same crossing from different directions. All of these sets have a total of 3 or 4 taps, of which the first path is static, and serves as normalization for the other taps. The other taps are uniformly defined as Rayleigh taps, meaning that $H_i \sim \mathcal{CN}(0,1)$ is drawn from a zero-mean circular symmetric Gaussian random variable with unit power. The shape of the PSD is specified as Half-Bathtub Shape (HalfBT), with the maximum Doppler frequency f_d as the design parameter. I implement the half-bathtub shape by starting from the usual Jakes' Doppler model [111], and setting one half of the Doppler spectrum to zero. Such a Doppler spectrum can be observed when the incident backscattered waves are not uniformly distributed in their power. As shown in Fig. C.2, this can be caused by non-omni-directional antenna patterns. Equivalently, the same Doppler spectrum is observed if the contributing scatterers are located only in front or behind of the receiving communication node. These situations are often encountered in vehicular contexts, due to the asymmetric scatterer placement, as well as the communication happening predominantly along the road, and not perpendicular. Measurements demonstrating asymmetric Doppler spreads were published in [114]. I use the most extreme Doppler frequency $f_{i,d}$ as the design parameter, which is signed, and thus also indicates the nonzero side of the spectrum. Finally, the tap gains η_i are shown in the table in terms of power η_i^2.

Die approbierte gedruckte Originalversion dieser Dissertation ist an der TU Wien Bibliothek verfügbar.
The approved original version of this doctoral thesis is available in print at TU Wien Bibliothek.
TU Bibliothek Your knowledge hub WIEN

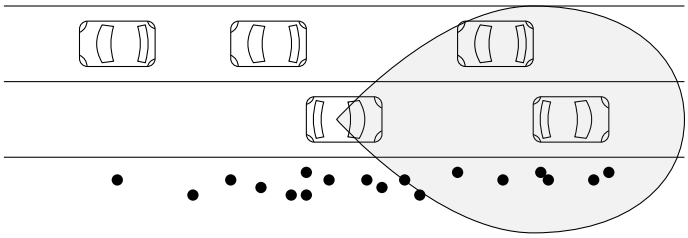

Figure C.2: Possible scatterer distribution. Dots represent static scatterers, and the grey area indicates a possible directional antenna pattern.

The purpose of the given models is to strike a balance between relevance to the specific scenarios, generality and ease of implementation. As such, the relative speed between transmitter and receiver does not factor into the LOS tap and a single representative set of Doppler profiles is used per model. Additionally, the one-sided Doppler spectra are not trying to represent a specific real situation, but instead aim at presenting a given challenge equivalent to real channels. Thus, all parameters of the models are fitted to demonstrate the RMS delay and Doppler spreads encountered in measurements [115–117]. Even with these limitations, the channel models use a sufficient amount of degrees of freedom to pose a varied challenge in terms of multi-path and Doppler combinations, allowing accurate receiver benchmarking via emulation.

The *Rural LOS* model defines a communication baseline, which is almost an AWGN channel in nature, with two early multi-path components that have moderate Doppler shifts, but are strongly attenuated compared to the LOS component. I will now illustrate the general road setup leading to the Urban and Highway scenarios.

Urban Scenarios

Figure C.3 illustrates a possible road setup in accordance with the *Urban Crossing* scenario. The direct path is barely free of obstacles, leading to a low power relative to the backscattered paths. A second group of scatterers is made up of moving cars positioned between the communication nodes. Due to this positioning, the scatterers result in small delays, and the Doppler shift is small, since the scatterer exhibiting positive relative velocities with respect to one, and negative to the other communication node. The second scatterer group can be seen as cars that are retreating from both vehicles, which results in negative Doppler shifts, as well as larger delays. The final, and weakest scatterer group is caused by scatterers positioned far away being approached by both, yielding the weakest signal with the largest positive Doppler shifts. The overall positive Doppler shift is based on the assumption of vehicles communicating that are both approaching the crossing, which represents the crossing scenario where transmission quality is most essential.

The chief difference of the *Urban Approaching* scenario lies in the fact that the receiving car is placed on the same road as the transmitter, in the oncoming lane. Therefore, backscattering

Die approbierte gedruckte Originalversion dieser Dissertation ist an der TU Wien Bibliothek verfügbar.
The approved original version of this doctoral thesis is available in print at TU Wien Bibliothek.
TU Bibliothek Your knowledge hub WIEN

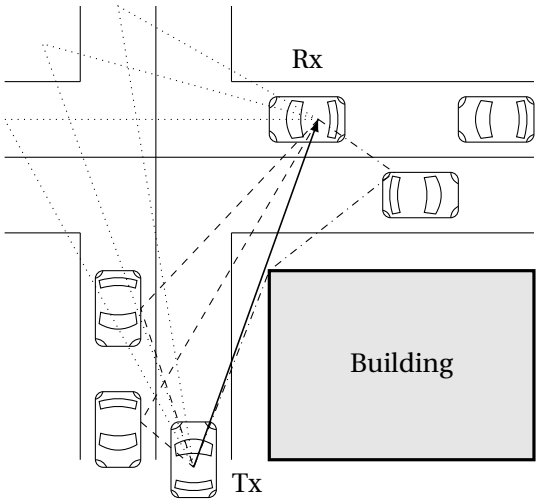

Figure C.3: Road crossing scenario. The lines indicate the LOS (arrow), scatterer that approach one, but retreat from the other node (dashed), retreat from both (dash-dotted) and are approached by both (dotted).

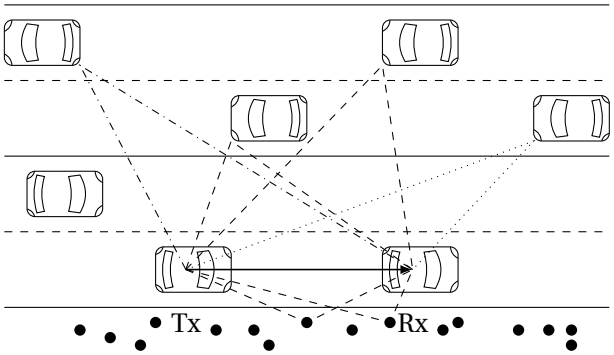

Figure C.4: Highway LOS. As above, the lines indicate LOS (arrow), scatterers that approach one, but retreat from the second node (dashed), retreat from both (dash-dotted) and approach both (dotted).

happens earlier as no corner traveling is possible, but with higher relative Doppler shifts, since higher relative movement speeds are used.

Highway Scenarios

Figure C.4 demonstrates the *Highway LOS* scenario. Similar to the *Urban* scenarios, the different scatterer groups can be identified by their relative placement. The highway setting naturally leads to larger Doppler shifts, as well as larger delays due to the open setting. The difference between LOS and NLOS scenarios is that NLOS assumes a large obstacle, such as a truck, between the communication nodes, which results in a weak LOS component, and allows larger delay spreads to contribute to the received signal.

Die approbierte gedruckte Originalversion dieser Dissertation ist an der TU Wien Bibliothek verfügbar.
The approved original version of this doctoral thesis is available in print at TU Wien Bibliothek.

Die approbierte gedruckte Originalversion dieser Dissertation ist an der TU Wien Bibliothek verfügbar.
The approved original version of this doctoral thesis is available in print at TU Wien Bibliothek.

List of Acronyms

5G fifth generation of cellular network technology

AC Access Class

ACK Acknowledgement

ADC Analog-Digital Converter

AIC Akaike Information Criterion

AGC Automatic Gain Control

AWGN Additive White Gaussian Noise

BEC Binary Erasure Channel

BSM Base Safety Message

C-ITS Cooperative Intelligent Transport Systems

c-LASSO Complex Least Absolute Shrinkage and Selection Operator

CAM Cooperative Awareness Message

CCA Clear Channel Assessment

CCH Control Channel

CDF Cumulative Distribution Function

CP Cyclic Prefix

COST Cooperation in Science and Technology

CRC Cyclic Redundancy Check

CSMA/CA Carrier Sense Multiple Access with Collision Avoidance

DCC Distributed Congestion Control

CVIS Cooperative Vehicle-Infrastructure Systems

Die approbierte gedruckte Originalversion dieser Dissertation ist an der TU Wien Bibliothek verfügbar.
The approved original version of this doctoral thesis is available in print at TU Wien Bibliothek.
TU Bibliothek Your knowledge hub WIEN

D2D Device-to-Device

DENM Decentralized Environmental Notification Message

DFT Discrete Fourier Transform

DSFT Discrete Symplectic Fourier Transform

ECDF Empirical Cumulative Distribution Function

EDCA Enhanced Distributed Channel Access

EIRP Effective Isotropic Radiated Power

ETSI European Telecommunications Standards Institute

FCS Frame Check Sequence

FPGA Field-Programmable Gate Array

GPS Global Positioning System

GSCM Geometry-based Stochastic Channel Model

HMM Hidden Markov Model

ICI Inter-Carrier Interference

IDFT Inverse DFT

IDM Intelligent Driver Model

IoT Internet of Things

ISI Inter-Symbol-Interference

ITS Intelligent Transportation Systems

ITS-G5 ITS at 5.9 GHz

LASSO Least Absolute Shrinkage and Selection Operator

LOS Line-of-Sight

LTE Long Term Evolution

LTS Long Training Sequence

MAC Medium Access Control

MCS Modulation and Coding Scheme

MMSE Minimum Mean Squared Error

Die approbierte gedruckte Originalversion dieser Dissertation ist an der TU Wien Bibliothek verfügbar.
The approved original version of this doctoral thesis is available in print at TU Wien Bibliothek.
TU Bibliothek Your knowledge hub WIEN

mmWave Millimeter Wave

MPC Multipath Component

MSE Mean Squared Error

NI National Instruments

NLOS Non Line-of-Sight

NMSE Normalized Mean Squared Error

NR New Radio

OAM Orbital Angular Momentum

OEW Open-Ended Waveguide

OFDM Orthogonal Frequency-Division Multiplexing

OSI Open Systems Interconnection

OTFS Orthogonal Time-Frequency Space

OTSM Off-the-Shelf Modem

PC Personal Computer

PCMA* Predictive Congestion Minimization in Combination with an A* based router

pdf probability density function

PDP Power Delay Profile

PDR Packet Delivery Rate

PER Packet Error Rate

PHY Physical Layer

pmf probability mass function

PSD Power Spectral Density

QPSK Quaternary Phase Shift Keying

RMS Root Mean Squared

RSSI Received Signal Strength Indicator

RSU Roadside Unit

SDR Software Defined Radio

Die approbierte gedruckte Originalversion dieser Dissertation ist an der TU Wien Bibliothek verfügbar.
The approved original version of this doctoral thesis is available in print at TU Wien Bibliothek.
TU Bibliothek Your knowledge hub WIEN

SE Squared Error

SIR Signal-to-Interference Ratio

SNR Signal-to-Noise Ratio

STS Short Training Sequence

SUV Sports Utility Vehicle

UDP Universal Datagram Protocol

USRP RIO Universal Software Radio Peripheral with Reconfigurable I/O

USRP Universal Software Radio Peripheral

V2I Vehicle-to-Infrastructure

V2V Vehicle-to-Vehicle

V2X Vehicle-to-Everything

VANET Vehicular Ad-Hoc Network

WAVE Wireless Access in Vehicular Environments

WSSUS Wide-Sense Stationary with Uncorrelated Scattering

WSS Wide-Sense Stationary

ZF Zero Forcing

Die approbierte gedruckte Originalversion dieser Dissertation ist an der TU Wien Bibliothek verfügbar.
The approved original version of this doctoral thesis is available in print at TU Wien Bibliothek.
TU Bibliothek Your knowledge hub WIEN

List of Figures

1.1 Comparison between cellular connectivity and vehicular ad-hoc connectivity. . 4

1.2 The OSI Layer model. A transmission (Tx) passes through the layers from top to bottom before being transmitted over the channel. Then, the transmission is received at the physical layer again, and passes upwards through the layers at the receiver (Rx). 6

1.3 PHY structure of an IEEE 802.11p frame. 7

1.4 Worst case SIR due to ICI. 9

1.5 Frequency allocations for IEEE 802.11p in the WAVE and ETSI ITS-G5 standards. ETSI has defined blocks of ITS-G5A to ITS-G5D, where ITS-G5C lies outside the 5.9 GHz bands at 5.4 to 5.7 GHz [23]. 10

1.6 Illustration of the hidden node problem. In a), all nodes are within communication range of each other. However, in b), nodes (1) and (3) are not able to sense each other. They are *hidden* with respect to each other, and may interfere. . . . 11

2.1 Necessary stages for channel emulation. **1)** depicts the encountered MPCs of a V2V transmission, **2)** shows a simplified channel impulse response representation of **1)**, and **3)** shows how a physical device applies the model from **2)** to a signal going from Transmitter (TX) to Receiver (TX). 16

2.2 System view of the emulator. 17

2.3 Magnitude realization of frequency response $\boldsymbol{h}$ and corresponding impulse response $\boldsymbol{g}$. The figure indicates the distribution of channel energy in different domains. 20

2.4 Example transfer function and impulse response snapshot from measurements. The strong components clearly arrive in clusters. Potential clusters are indicated with ellipses. 22

Die approbierte gedruckte Originalversion dieser Dissertation ist an der TU Wien Bibliothek verfügbar.
The approved original version of this doctoral thesis is available in print at TU Wien Bibliothek.
TU Bibliothek Your knowledge hub WIEN

2.5 Analysis of the $\boldsymbol{W}$ weighting matrix that indicates the implementation complexity. 25

2.6 Sample Saleh-Valenzuela PDPs. The plots show a realization for Conf. **(a)**,**(b)**,**(c)** and **(d)**, each produced with the same random seed. 32

2.7 Photograph of the measurement site. The transmitter and receiver are static and urban street traffic is driving by. 33

2.8 Zoomed photographs of the measurement site. On the left-hand side the photo shows the transmit horn antenna mounted on a tripod. As multiple reflection with the transmitter car are below the receiver sensitivity, the TX car is replaced with a tripod. On the right-hand side the photo shows the open-ended waveguide receive antenna mounted at roof height at the left, rear car side window. 33

2.9 Relative change of MSE for the 4 configurations **(a)–(d)** of the Saleh-Valenzuela models. 36

2.10 Sample impulse responses, estimated cluster impulse responses and cluster locations for $M = 16$ and $P \in \{1,2,4\}$ (**(a)**, **(b)** and **(c)**). 38

2.11 4-tap delay evolution for an overtaking SUV. Memoryless estimations on the left (**(a), (c), (e)**), sequential estimations on the right (**(b), (d), (f)**). 39

2.12 MSE and AIC of the analyzed measurements (**(a)–(d)**). 40

2.13 Optimal number of clusters K_0 for all presented estimation basis and measurements. The numbering is consistent with Fig. 2.12. 41

2.14 Image of measurement setup. 42

2.15 Channel estimations with Sparseness $M = 4$ and time aggregations of $T \in \{4,8,16,32,64\}$. The left plots show the positions of the delay estimates, the right plots the positions in Doppler domain. The grid is circularly shifted to avoid wraparounds in delay domain. 43

2.16 Comparison of AIC and AIC$^{(n)}$. 45

2.17 Histogram of the computed Akaike weights, for non-normalized AIC (above) and normalized AIC (below). 46

3.1 Final description of the communication decomposition. 49

3.2 System Level Model for the Single Link Channel. 50

3.3 Testbed setup: Transmitter (Tx), vehicular channel emulator (Em), stepped attenuator, and receiver (Rx) wired by RF coaxial cables. 51

Die approbierte gedruckte Originalversion dieser Dissertation ist an der TU Wien Bibliothek verfügbar.
The approved original version of this doctoral thesis is available in print at TU Wien Bibliothek.
TU Bibliothek Your knowledge hub WIEN

3.4 Urban crossing channel scenario. 52

3.5 Measured PDP and 10-tap LASSO fit (c.f. [51]). 53

3.6 PSD of an original Jakes' trace, and the right and left sided versions. The simulation is done at 5.9 GHz, and the maximum relative velocity is 10 m/s. 54

3.7 Packet error ratio (left) and packet error probability (right) estimates from emulated nonstationary vehicular channel. 56

3.8 PER (left) and packet error probability (right) estimates from emulated stationary vehicular channel. 57

3.9 Mean and burst behavior for 500 and 100 Bytes packet size. 60

3.10 Traffic congestion. in Linz, Austria. Green dots are vehicles traveling from north to south, simulation results from [85]. 61

3.11 Four snapshots at different simulation times of the traffic flow simulation. The blue dots show vehicle positions at the given snapshots. 62

3.12 Representation of a physical scenario with seven nodes (a), as well as a MAC layer abstraction of the same scenario (b). 62

3.13 Two possible channel performance models representing the scenario in Fig. 3.12. 64

3.14 Graph approximation evaluation. 67

3.15 Magnitude of the autocorrelation function of the frequency domain channels. . 67

3.16 Measurement setup. 68

3.17 PER versus SIR for interfering cliques of different sizes. For 500 bytes, no difference exists for 100 and 140 interferers. 69

3.18 Snapshot of clique distribution [85]. 70

3.19 Change of clique parameters over simulation time. 70

3.20 PER simulation time for 1 and 3 used channels, and distances of 25, 50 and 100 m to the receiver. 71

4.1 System Model. 74

4.2 The Gilbert-Elliott model has two states, good and bad, and assigns packet error probabilities ($P_{\mathscr{E}}^{g}$ and $P_{\mathscr{E}}^{b}$) and transition probabilities (P_{GB} and P_{BG}) to both. . 75

4.3 Parameter scatter plot of the block-constant fit. 83

Die approbierte gedruckte Originalversion dieser Dissertation ist an der TU Wien Bibliothek verfügbar.
The approved original version of this doctoral thesis is available in print at TU Wien Bibliothek.
TU Bibliothek Your knowledge hub WIEN

4.4 Calculated parameters for the mean SNR grouped fit. 83

4.5 Optimal threshold and PER for the fading aware parameter fit. 84

4.6 Time evolution of model parameter fits. Calculated refers to the block-constant fit. 85

4.7 Evaluation of the mean SNR grouped and the fading aware model. The figures show an evaluation of the PER, as well as the burst lengths, represented by $\Pr(\mathscr{C}_i|\mathscr{C}_{i-1})$ and $\Pr(\mathscr{E}_i|\mathscr{E}_{i-1})$. Figures (a), (c) and (e) show the behaviors over mean SNR, while Figures (b), (d) and (f) display time evolutions over 500 s. . . 86

4.8 Histograms for the burst-modeling capabilities of the fading aware and the mean SNR grouped estimators. 89

4.9 $\Pr(\mathscr{E})$ estimation for SNR quantization into 4 and 9 intervals. 91

4.10 Schematic illustration of the simulated highway scenario. 93

4.11 Gilbert-Elliott MSE and AIC as function of SNR interval count M. 93

4.12 Interference MSE as a function of interval count M. 94

4.13 Resulting pdfs of the optimal intervals. 96

4.14 Total $\Pr(\mathscr{E})$ as function of SNR and Nr. of interferers. 97

A.1 Urban crossing channel scenario. 101

A.2 Channel sounder results. 102

A.3 Measured PDP and 10-tap LASSO fit (c.f. [51]). 103

A.4 MSE and AIC of the analyzed measurements (**(a)–(d)**). 104

B.1 System view of the emulator. 105

B.2 Tapped-delay architecture for time-variant convolution. 106

C.1 Comparison of ECDFs of a Rayleigh distribution, and the magnitudes and phases of $\boldsymbol{h}'_i$, $\boldsymbol{h}'_{i,RS}$ and $\boldsymbol{h}'_{i,LS}$. 108

C.2 Possible scatterer distribution. Dots represent static scatterers, and the grey area indicates a possible directional antenna pattern. 110

C.3 Road crossing scenario. The lines indicate the LOS (arrow), scatterer that approach one, but retreat from the other node (dashed), retreat from both (dash-dotted) and are approached by both (dotted). 111

Die approbierte gedruckte Originalversion dieser Dissertation ist an der TU Wien Bibliothek verfügbar.
The approved original version of this doctoral thesis is available in print at TU Wien Bibliothek.
TU Bibliothek Your knowledge hub WIEN

C.4 Highway LOS. As above, the lines indicate LOS (arrow), scatterers that approach one, but retreat from the second node (dashed), retreat from both (dash-dotted) and approach both (dotted). 111

Die approbierte gedruckte Originalversion dieser Dissertation ist an der TU Wien Bibliothek verfügbar.
The approved original version of this doctoral thesis is available in print at TU Wien Bibliothek.

Die approbierte gedruckte Originalversion dieser Dissertation ist an der TU Wien Bibliothek verfügbar.
The approved original version of this doctoral thesis is available in print at TU Wien Bibliothek.

List of Tables

1.1 Allowed MCSs, along with the required channel quality and packet durations. [19] 8

2.1 Saleh-Valenzuela parameter combinations. 31

2.2 Channel sounding measurement parameters 33

2.3 Channel sounding measurement parameters 42

3.1 ETSI draft channel model parameters. 55

3.2 Measurement setup parameters for nonstationary model test. 58

4.1 Measurement parameters 74

4.2 Statistical analysis of the squared error of various estimators. 87

4.3 MSE behavior of $\Pr(\mathscr{C}_i|\mathscr{C}_{i-1})$ and $\Pr(\mathscr{E}_i|\mathscr{E}_{i-1})$ 88

4.4 Measurement parameters 92

4.5 System Level Simulation Parameters 93

4.6 Gilbert-Elliott parameters for 6 intervals. 94

4.7 Interference parameters for Gaussian Fits of 6 intervals. 95

A.1 Measurement Parameters 102

C.1 Link Level Channel Models 109

Die approbierte gedruckte Originalversion dieser Dissertation ist an der TU Wien Bibliothek verfügbar.
The approved original version of this doctoral thesis is available in print at TU Wien Bibliothek.
TU Bibliothek Your knowledge hub WIEN

Die approbierte gedruckte Originalversion dieser Dissertation ist an der TU Wien Bibliothek verfügbar.
The approved original version of this doctoral thesis is available in print at TU Wien Bibliothek.

Bibliography

[1] M. Castells, "The information age: Economy, society and culture (3 volumes)," *Blackwell, Oxford*, vol. 1997, p. 1998, 1996.

[2] L. K. Grossman, *Electronic republic: Reshaping American democracy for the information age*. Viking Books, 1995.

[3] D. C. Schleher, *Electronic warfare in the information age*. Artech House, Inc., 1999.

[4] A. Melucci, *Challenging codes: Collective action in the information age*. Cambridge University Press, 1996.

[5] M. Weiser, "The computer for the 21 st century," *Scientific American*, vol. 265, no. 3, pp. 94–105, 1991. [Online]. Available: http://www.jstor.org/stable/24938718

[6] K. Ashton *et al.*, "That 'internet of things' thing," *RFID journal*, vol. 22, no. 7, pp. 97–114, 2009.

[7] P. Ritchie, *Cause of Death*. Black & White Publishing Ltd, 2017, vol. 1.

[8] T. B. Sheridan, "Human centered automation: oxymoron or common sense?" in *1995 IEEE International Conference on Systems, Man and Cybernetics. Intelligent Systems for the 21st Century*, vol. 1. IEEE, 1995, pp. 823–828.

[9] H. Seo, K.-D. Lee, S. Yasukawa, Y. Peng, and P. Sartori, "Lte evolution for vehicle-to-everything services," *IEEE communications magazine*, vol. 54, no. 6, pp. 22–28, 2016.

[10] A. Paier, "The end-to-end intelligent transport system (its) concept in the context of the european cooperative its corridor," in *2015 IEEE MTT-S International Conference on Microwaves for Intelligent Mobility (ICMIM)*. IEEE, 2015, pp. 1–4.

[11] M. Laner, P. Svoboda, P. Romirer-Maierhofer, N. Nikaein, F. Ricciato, and M. Rupp, "A comparison between one-way delays in operating hspa and lte networks," in *2012 10th International Symposium on Modeling and Optimization in Mobile, Ad Hoc and Wireless Networks (WiOpt)*. IEEE, 2012, pp. 286–292.

[12] W. Sun, E. G. Ström, F. Brännström, Y. Sui, and K. C. Sou, "D2d-based v2v communications with latency and reliability constraints," in *2014 IEEE Globecom Workshops (GC Wkshps)*. IEEE, 2014, pp. 1414–1419.

[13] E. Ström, P. Popovski, and J. Sachs, "5G Ultra-Reliable Vehicular Communication," Oct 2015. [Online]. Available: http://arxiv.org/abs/1510.01288

[14] G. Naik, B. Choudhury, and J. Park, "Ieee 802.11bd 5g nr v2x: Evolution of radio access technologies for v2x communications," *IEEE Access*, vol. 7, pp. 70 169–70 184, 2019.

[15] R. Molina-Masegosa and J. Gozalvez, "System level evaluation of lte-v2v mode 4 communications and its distributed scheduling," in *2017 IEEE 85th Vehicular Technology Conference (VTC Spring)*, June 2017, pp. 1–5.

[16] K. Sjoberg, P. Andres, T. Buburuzan, and A. Brakemeier, "Cooperative intelligent transport systems in europe: Current deployment status and outlook," *IEEE Vehicular Technology Magazine*, vol. 12, no. 2, pp. 89–97, 2017.

[17] A. M. S. Abdelgader and W. Lenan, "The physical layer of the ieee 802.11p wave communication standard: The specifications and challenges," 2014.

Die approbierte gedruckte Originalversion dieser Dissertation ist an der TU Wien Bibliothek verfügbar.
The approved original version of this doctoral thesis is available in print at TU Wien Bibliothek.
TU Bibliothek Your knowledge hub WIEN

[18] H. Wen, P.-H. Ho, and G. Gong, "A novel framework for message authentication in vehicular communication networks," in *GLOBECOM 2009-2009 IEEE Global Telecommunications Conference*. IEEE, 2009, pp. 1–6.

[19] A. Bazzi, B. M. Masini, A. Zanella, and G. Pasolini, "Vehicle-to-vehicle and vehicle-to-roadside multi-hop communications for vehicular sensor networks: Simulations and field trial," in *2013 IEEE International Conference on Communications Workshops (ICC)*. IEEE, 2013, pp. 515–520.

[20] T. S. Rappaport *et al.*, *Wireless communications: principles and practice*. prentice hall PTR New Jersey, 1996, vol. 2.

[21] L. Bernado, T. Zemen, F. Tufvesson, A. F. Molisch, and C. F. Mecklenbräuker, "Delay and Doppler Spreads of Nonstationary Vehicular Channels for Safety-Relevant Scenarios," *IEEE Transactions on Vehicular Technology*, vol. 63, no. 1, pp. 82–93, Jan 2014.

[22] ETSI, "TS 102 637-2 - V1.2.1 - Intelligent Transport Systems (ITS); Vehicular Communications; Basic Set of Applications; Part 2: Specification of Cooperative Awareness Basic Service." [Online]. Available: http://www.etsi.orghttp://portal.etsi.org/tb/status/status.asphttp://portal.etsi.org/chaircor/ETSI_support.asp

[23] ——, "302 663," *Intelligent Transport Systems (ITS)*, pp. 2012–11, 2013.

[24] S. Eichler, "Performance Evaluation of the IEEE 802.11p WAVE Communication Standard," in *Veh. Technol. Conf.* IEEE, Sep 2007, pp. 2199–2203.

[25] Y. Zang, B. Walke, G. Hiertz, and C. Wietfeld, "IEEE 802.11p-based Packet Broadcast in Radio Channels with Hidden Stations and Congestion Control," Dec 2016.

[26] T. Abbas, K. Sjöberg, J. Karedal, and F. Tufvesson, "A Measurement Based Shadow Fading Model for Vehicle-to-Vehicle Network Simulations," *Int. J. Antennas Propag.*, vol. 2015, pp. 1–12, 2015.

[27] R. He, A. F. Molisch, F. Tufvesson, Z. Zhong, B. Ai, and T. Zhang, "Vehicle-to-Vehicle Propagation Models With Large Vehicle Obstructions," *IEEE Trans. Intell. Transp. Syst.*, vol. 15, no. 5, pp. 2237–2248, 2014.

[28] C. Gustafson, K. Haneda, S. Wyne, and F. Tufvesson, "On mm-wave multipath clustering and channel modeling," *IEEE Transactions on Antennas and Propagation*, vol. 62, no. 3, pp. 1445–1455, Mar 2014.

[29] T. Abbas, L. Bernado, A. Thiel, C. Mecklenbräuker, and F. Tufvesson, "Radio Channel Properties for Vehicular Communication: Merging Lanes Versus Urban Intersections," *IEEE Veh. Technol. Mag.*, vol. 8, no. 4, pp. 27–34, 2013.

[30] J. Karedal, N. Czink, A. Paier, F. Tufvesson, and A. F. Molisch, "Path Loss Modeling for Vehicle-to-Vehicle Communications," *Trans. Veh. Technol.*, vol. 60, no. 1, pp. 323–328, Jan 2011.

[31] C. F. Mecklenbräuker, A. F. Molisch, J. Karedal, F. Tufvesson, A. Paier, L. Bernado, T. Zemen, O. Klemp, and N. Czink, "Vehicular Channel Characterization and Its Implications for Wireless System Design and Performance," *Proc. IEEE*, vol. 99, no. 7, pp. 1189–1212, Jul 2011.

[32] E. Zöchmann *et al.*, "Measured delay and Doppler profiles of overtaking vehicles at 60 GHz," in *Proc. of the 12th European Conference on Antennas and Propagation (EuCAP)*, London, Great Britain, 2018, pp. 1–5.

[33] H. Groll, E. Zöchmann, S. Pratschner, M. Lerch, D. Schützenhöfer, M. Hofer, J. Blumenstein, S. Sangodoyin, T. Zemen, A. Prokes, A. Molisch, and S. Caban, "Sparsity in the Delay-Doppler domain for measured 60 GHz Vehicle-to-Infrastructure communication channels," in *2019 IEEE International Conference on Communications (ICC)*, Shanghai, P.R. China, May 2019.

[34] D. W. Matolak, I. Sen, W. Xiong, and N. T. Yaskoff, "5 GHz wireless channel characterization for vehicle to vehicle communications," in *Proc. IEEE Mil. Commun. Conf.*, vol. 5, 2005, pp. 3016–3022.

[35] R. Sun, D. W. Matolak, and P. Liu, "5-GHz V2V Channel Characteristics for Parking Garages," *IEEE Trans. Veh. Technol.*, pp. 1–1, 2016.

[36] P. Liu, B. Ai, D. W. Matolak, R. Sun, and Y. Li, "5-GHz Vehicle-to-Vehicle Channel Characterization for Example Overpass Channels," *IEEE Trans. Veh. Technol.*, vol. 65, no. 8, pp. 5862–5873, Aug 2016.

[37] B. Ai, X. Cheng, T. Kürner, Z.-D. Zhong, K. Guan, R.-S. He, L. Xiong, D. W. Matolak, D. G. Michelson, and C. Briso-Rodriguez, "Challenges toward wireless communications for high-speed railway," *IEEE Transactions on Intelligent Transportation Systems*, vol. 15, no. 5, pp. 2143–2158, 2014.

Die approbierte gedruckte Originalversion dieser Dissertation ist an der TU Wien Bibliothek verfügbar.
The approved original version of this doctoral thesis is available in print at TU Wien Bibliothek.
TU Bibliothek Your knowledge hub WIEN

[38] M. Hofer, Z. Xu, D. Vlastaras, B. Schrenk, D. Loeschenbrand, F. Tufvesson, and T. Zemen, "Validation of a real-time geometry-based stochastic channel model for vehicular scenarios," in *Proc. of 87th Vehicular Technology Conference (VTC Spring)*. Porto, Portugal: IEEE, June 2018, pp. 1–5.

[39] M. Hofer, Z. Xu, and T. Zemen, "Real-time channel emulation of a geometry-based stochastic channel model on a SDR platform," in *Proc. of 18th International Workshop on Signal Processing Advances in Wireless Communications (SPAWC)*. Hokkaido, Japan: IEEE, 2017, pp. 1–5.

[40] V. Shivaldova, A. Winkelbauer, and C. F. Mecklenbräuker, "Vehicular Link Performance: From Real-World Experiments to Reliability Models and Performance Analysis," *IEEE Veh. Technol. Mag.*, vol. 8, no. 4, pp. 35–44, Dec 2013.

[41] F. Abrate, A. Vesco, and R. Scopigno, "An Analytical Packet Error Rate Model for WAVE Receivers," in *Veh. Technol. Conf. (VTC Fall), 2011 IEEE*, Sep 2011, pp. 1–5.

[42] M. Sepulcre, J. Gozalvez, O. Altintas, and H. Kremo, "Integration of congestion and awareness control in vehicular networks," *Ad Hoc Networks*, vol. 37, 2016.

[43] H. D. Schotten, R. Sattiraju, D. G. Serrano, Z. Ren, and P. Fertl, "Availability indication as key enabler for ultra-reliable communication in 5G," in *2014 Eur. Conf. Networks Commun.* IEEE, Jun 2014, pp. 1–5.

[44] J. Gozalvez, M. Sepulcre, and R. Bauza, "Impact of the radio channel modelling on the performance of communication VANET protocols," *Telecommun. Syst.*, vol. 50, no. 3, pp. 149–167, 2012. [Online]. Available: http://dx.doi.org/10.1007/s11235-010-9396-x

[45] ——, "IEEE 802.11p vehicle to infrastructure communications in urban environments," *IEEE Commun. Mag.*, vol. 50, no. 5, pp. 176–183, 2012.

[46] K. Bilstrup, E. Uhlemann, E. Ström, and U. Bilstrup, "On the Ability of the 802.11p MAC Method and STDMA to Support Real-Time Vehicle-to-Vehicle Communication," *EURASIP J. Wirel. Commun. Netw.*, vol. 2009, pp. 1–13, 2009. [Online]. Available: http://jwcn.eurasipjournals.com/content/2009/1/902414

[47] K. Sjöberg, E. Uhlemann, and E. Ström, "Scalability Issues of the MAC Methods STDMA and CSMA of IEEE 802.11p When Used in VANETs," in *Int. Conf. Commun. Work.* IEEE, May 2010, pp. 1–5.

[48] C. F. Mecklenbräuker, P. Gerstoft, and E. Zöchmann, "c–LASSO and its dual for sparse signal estimation from array data," *Signal Processing*, vol. 130, pp. 204–216, 2017.

[49] D. Posada, T. R. Buckley, and J. Thorne, "Model Selection and Model Averaging in Phylogenetics: Advantages of Akaike Information Criterion and Bayesian Approaches Over Likelihood Ratio Tests," *Syst. Biol.*, vol. 53, no. 5, pp. 793–808, Oct 2004.

[50] T. Blazek, E. Zöchmann, and C. F. Mecklenbräuker, "Millimeter Wave Vehicular Channel Emulation: A Framework for Balancing Complexity and Accuracy," *Sensors*, vol. 18, no. 11, p. 3997, 2018.

[51] T. Blazek and C. Mecklenbräuker, "Sparse time-variant impulse response estimation for vehicular channels using the c-LASSO," in *Proc. of 28th Annual International Symposium on Personal, Indoor, and Mobile Radio Communications (PIMRC)*. Montreal, Canada: IEEE, 2018.

[52] T. Blazek, E. Zöchmann, and C. F. Mecklenbräuker, "Model order selection for LASSO fitted millimeter wave vehicular channel data," in *Proc. of 29th Annual International Symposium on Personal, Indoor, and Mobile Radio Communications (PIMRC)*. Bologna, Italy: IEEE, Sep 2018, pp. 1–5. [Online]. Available: https://publik.tuwien.ac.at/files/publik_271471.pdf

[53] ——, "Approximating clustered millimeter wave vehicular channels by sparse subband fitting," in *Proc. of 29th Annual International Symposium on Personal, Indoor, and Mobile Radio Communications (PIMRC)*. Bologna, Italy: IEEE, Sep 2018, pp. 1–5. [Online]. Available: https://publik.tuwien.ac.at/files/publik_271472.pdf

[54] T. Blazek, H. Groll, S. Pratschner, and E. Zochmann, "Vehicular channel characterization in orthogonal time-frequency space," in *2019 IEEE International Conference on Communications Workshops (ICC Workshops)*, May 2019, pp. 1–5.

Die approbierte gedruckte Originalversion dieser Dissertation ist an der TU Wien Bibliothek verfügbar.
The approved original version of this doctoral thesis is available in print at TU Wien Bibliothek.
TU Bibliothek Your knowledge hub WIEN

[55] G. Ghiaasi, T. Blazek, M. Ashury, R. R. Santos, and C. Mecklenbräuker, "Real-time emulation of nonstationary channels in safety-relevant vehicular scenarios," *Wireless Communications and Mobile Computing*, 2018.

[56] T. Blazek, G. Ghiaasi, C. Backfrieder, G. Ostermayer, and C. Mecklenbräuker, "Performance modeling and analysis for vehicle-to-anything connectivity in representative high-interference channels," *Accepted for publication at IET microwaves, antennas & propagation*, vol. 99, no. 99, pp. 1–9, 2019.

[57] T. Blazek, C. Backfrieder, C. Mecklenbräuker, and G. Ostermayer, "Improving communication reliability in intelligent transport systems through cooperative driving," in *10th IFIP Wireless and Mobile Networking Conference*, Sep. 2017.

[58] T. Blazek, C. Mecklenbräuker, D. Smely, G. Ghiaasi, and M. Ashury, "Vehicular channel models: A system level performance analysis of tapped delay line models," in *15th International Conference on ITS Telecommunications*, May 2017.

[59] T. Blazek, G. Ghiaasi, C. Backfrieder, G. Ostermayer, and C. Mecklenbräuker, "IEEE 802.11p Performance for Vehicle-to-Anything Connectivity in Urban Interference Channels," in *12th Eur. Conf. Antennas Propag.*, 2018, pp. 1–5.

[60] T. Blazek and C. Mecklenbräuker, "Measurement-Based Burst-Error Performance Modeling for Cooperative Intelligent Transport Systems," *IEEE Trans. Intell. Transp. Syst.*, 2018.

[61] T. Blazek and C. F. Mecklenbräuker, "Complexity SNR-Based Packet Level Burst-Error Model for Vehicular Ad-Hoc Networks," in *IEEE VTC Fall 2018*. Chicago: IEEE, 2018, p. 5.

[62] T. Blazek, H. Groll, S. Pratschner, and E. Zochmann, "Vehicular channel characterization in orthogonal time-frequency space," in *2019 IEEE International Conference on Communications Workshops (ICC Workshops)*. IEEE, 2019, pp. 1–5.

[63] J. Yang, B. Ai, K. Guan, D. He, X. Lin, B. Hui, J. Kim, and A. Hrovat, "A geometry-based stochastic channel model for the millimeter-wave band in a 3gpp high-speed train scenario," *IEEE Transactions on Vehicular Technology*, vol. 67, no. 5, pp. 3853–3865, May 2018.

[64] N. Dreyer, A. Moeller, J. Baumgarten, Z. H. Mir, T. Kuerner, and F. Filali, "On building realistic reference scenarios for ieee 802.11 p/lte-based vehicular network evaluations," in *Proc. of 87th Vehicular Technology Conference (VTC Spring)*. Porto, Portugal: IEEE, 2018, pp. 1–7.

[65] G. Acosta-Marum and M. A. Ingram, "Six Time-and Frequency- Selective Empirical Channel Models for Vehicular Wireless LANs," *IEEE Vehicular Technology Magazine*, vol. 2, no. 4, pp. 4–11, 2007.

[66] H. Asplund, A. A. Glazunov, A. F. Molisch, K. I. Pedersen, and M. Steinbauer, "The cost 259 directional channel model-part ii: macrocells," *IEEE Transactions on Wireless Communications*, vol. 5, no. 12, p. 3434, 2006.

[67] J. Meinilä, P. Kyösti, T. Jämsä, and L. Hentilä, "Winner ii channel models," *Radio Technologies and Concepts for IMT-Advanced*, pp. 39–92, 2009.

[68] D. E. Knuth, "Teach calculus with big o," *Notices of the American Mathematical Society*, vol. 45, no. 6, p. 687, 1998.

[69] T. Zemen, M. Hofer, D. Löschenbrand, and C. Pacher, "Iterative Detection for Orthogonal Precoding in Doubly Selective Channels," in *2018 IEEE 29th Annual International Symposium on Personal, Indoor and Mobile Radio Communications (PIMRC)*, Sep. 2018, pp. 1–7.

[70] S. Boyd and L. Vandenberghe, *Convex optimization*. Cambridge university press, 2004.

[71] M. Grant and S. Boyd, "Cvx: Matlab software for disciplined convex programming."

[72] R. J. Tibshirani and J. Taylor, "The solution path of the generalized lasso," *Ann. Statist.*, vol. 39, no. 3, pp. 1335–1371, 06 2011. [Online]. Available: https://doi.org/10.1214/11-AOS878

[73] E. Zöchmann, P. Gerstoft, and C. F. Mecklenbräuker, "Density evolution of sparse source signals," in *2015 3rd International Workshop on Compressed Sensing Theory and its Applications to Radar, Sonar and Remote Sensing (CoSeRa)*. Pisa, Italy: IEEE, Jun 2015, pp. 124–128.

Die approbierte gedruckte Originalversion dieser Dissertation ist an der TU Wien Bibliothek verfügbar.
The approved original version of this doctoral thesis is available in print at TU Wien Bibliothek.
TU Bibliothek Your knowledge hub WIEN

[74] A. Saleh and R. Valenzuela, "A Statistical Model for Indoor Multipath Propagation," *IEEE Journal on Selected Areas of Communications*, vol. 5, no. 2, pp. 128–137, Feb 1987.

[75] O. E. Ayach, R. W. Heath, S. Abu-Surra, S. Rajagopal, and Z. Pi, "The capacity optimality of beam steering in large millimeter wave MIMO systems," in *Proc. of 13th International Workshop on Signal Processing Advances in Wireless Communications (SPAWC)*. Cesme, Turkey: IEEE, Jun 2012, pp. 100–104.

[76] M. K. Samimi, G. R. MacCartney, S. Sun, and T. S. Rappaport, "28 GHz Millimeter-Wave Ultrawideband Small-Scale Fading Models in Wireless Channels," in *2016 83rd Vehicular Technology Conference (VTC Spring)*. Nanjing, China: IEEE, May 2016, pp. 1–6.

[77] C. Kim, X. Sun, L. Chiam, B. Kannan, F. Chin, and H. Garg, "Characterization of ultra-wideband channels for outdoor office environment," in *Wireless Communications and Networking Conference*, vol. 2. New Orleans, LA, USA: IEEE, 2005, pp. 950–955.

[78] A. Meijerink and A. F. Molisch, "On the Physical Interpretation of the Saleh–Valenzuela Model and the Definition of Its Power Delay Profiles," *IEEE Transactions on Antennas and Propagation*, vol. 62, no. 9, pp. 4780–4793, Sep 2014.

[79] K. P. Burnham and D. R. Anderson, "Multimodel inference: understanding AIC and BIC in model selection," *Sociological methods & research*, vol. 33, no. 2, pp. 261–304, 2004.

[80] H. Akaike, "A new look at the statistical model identification," *IEEE Transactions on Automatic Control*, vol. 19, no. 6, pp. 716–723, December 1974.

[81] W. K. Newey and D. McFadden, "Large sample estimation and hypothesis testing," *Handbook of econometrics*, vol. 4, pp. 2111–2245, 1994.

[82] R. He, A. F. Molisch, F. Tufvesson, Z. Zhong, B. Ai, and T. Zhang, "Vehicle-to-vehicle propagation models with large vehicle obstructions," *IEEE Transactions on Intelligent Transportation Systems*, vol. 15, no. 5, pp. 2237–2248, 2014.

[83] E. S. Sousa, V. M. Jovanovic, and C. Daigneault, "Delay spread measurements for the digital cellular channel in Toronto," *IEEE Transactions on Vehicular Technology*, vol. 43, no. 4, pp. 837–847, 1994.

[84] A. Paier, L. Bernado, J. Karedal, O. Klemp, and A. Kwoczek, "Overview of Vehicle-to-Vehicle Radio Channel Measurements for Collision Avoidance Applications," in *Proc. 71st Veh. Technol. Conf. (VTC Spring)*, 2010.

[85] C. Backfrieder, G. Ostermayer, and C. F. Mecklenbräuker, "Increased Traffic Flow Through Node-Based Bottleneck Prediction and V2X Communication," *Trans. Intell. Transp. Syst.*, vol. 18, no. 2, pp. 349–363, Feb 2017.

[86] C. Backfrieder, G. Ostermayer, and C. F. Mecklenbräuker, "TraffSim - A traffic simulator for investigations of congestion minimization through dynamic vehicle rerouting," *International Journal of Simulation Systems, Science and Technology*, vol. 15, no. 4, pp. 38–47, Aug. 2014.

[87] M. Treiber, A. Hennecke, and D. Helbing, "Congested traffic states in empirical observations and microscopic simulations," *Phys. Rev. E*, vol. 62, pp. 1805–1824, Aug 2000. [Online]. Available: https://link.aps.org/doi/10.1103/PhysRevE.62.1805

[88] C. Backfrieder and G. Ostermayer, "Modeling a Continuous and Accident-Free Intersection Control for Vehicular Traffic in TraffSim," in *2014 European Modelling Symposium*, Oct. 2014, pp. 332–337.

[89] C. Lee, F. Reid, A. Mcdaid, and N. Hurley, "Detecting Highly Overlapping Community Structure by Greedy Clique Expansion," 2010. [Online]. Available: https://arxiv.org/abs/1002.1827v2

[90] S. Sharma and M. Singh, "Generalized similarity measure for categorical data clustering," in *Int. Conf. Adv. Comput. Commun. Informatics*. IEEE, Sep 2016, pp. 765–769.

[91] T. Zemen and C. Mecklenbräuker, "Time-variant channel estimation using discrete prolate spheroidal sequences," *IEEE Trans. Signal Process.*, vol. 53, no. 9, pp. 3597–3607, Sep 2005.

[92] ETSI, "EN 302 663 - V1.2.0 - Intelligent Transport Systems (ITS); Access layer specification for Intelligent Transport Systems operating in the 5 GHz frequency band," 2012.

Die approbierte gedruckte Originalversion dieser Dissertation ist an der TU Wien Bibliothek verfügbar.
The approved original version of this doctoral thesis is available in print at TU Wien Bibliothek.
TU Bibliothek Your knowledge hub WIEN

[93] S. Subramanian and Others, "Congestion Control for Vehicular Safety: Synchronous and Asynchronous MAC Algorithms," in *Proc. Ninth ACM Int. Work. Veh. Inter-networking, Syst. Appl.* New York, NY, USA: ACM, 2012, pp. 63–72.

[94] E. O. Elliott, "Estimates of Error Rates for Codes on Burst-Noise Channels," *Bell Syst. Tech. J.*, vol. 42, no. 5, pp. 1977–1997, Sep 1963.

[95] E. N. Gilbert, "Capacity of a Burst-Noise Channel," *Bell Syst. Tech. J.*, vol. 39, no. 5, pp. 1253–1265, 1960.

[96] "Project "Robust And Distributed Safety-Improved Traffic Telematics" (ROADSAFE)," Available online: https://portal.ftw.at/projects/roadsafe/.

[97] "Cooperative vehicle-infrastructure systems (CVIS) project," Available online: http://www.cvisproject.org/.

[98] N. Tishby, F. C. Pereira, and W. Bialek, "The information bottleneck method," in *Proc. 37th Allert. Conf. Commun. Control Comput.*, Apr 1999, pp. 368–377. [Online]. Available: http://citeseerx.ist.psu.edu/viewdoc/summary?doi=10.1.1.6.9199

[99] L.-T. Yang, H. Jiang, C.-C. Guo, Y.-H. Wang, J. Wu, and L.-J. Chen, "A Four-State Markov Model Based on Measurements for Evaluating the Packet-level Performance of VANET," in *Proc. 68th IEEE Veh. Technol. Conf. (VTC Fall)*, 2008.

[100] T. M. Cover and J. A. Thomas, *Elements of Information Theory*. Hoboken, NJ, USA: John Wiley & Sons, Inc., Sep 2005. [Online]. Available: http://doi.wiley.com/10.1002/047174882X

[101] S. R. Eddy, "Hidden Markov models," *Curr. Opin. Struct. Biol.*, vol. 6, no. 3, pp. 361–365, 1996.

[102] L. Rabiner and B. Juang, "An introduction to hidden Markov models," *IEEE ASSP Mag.*, vol. 3, no. 1, pp. 4–16, 1986.

[103] M. Lindorfer, C. F. Mecklenbräuker, and G. Ostermayer, "Modeling the imperfect driver: Incorporating human factors in a microscopic traffic model," *IEEE Transactions on Intelligent Transportation Systems*, vol. 19, no. 9, pp. 2856–2870, 2017.

[104] C. Sommer, S. Joerer, M. Segata, O. K. Tonguz, R. L. Cigno, and F. Dressler, "How Shadowing Hurts Vehicular Communications and How Dynamic Beaconing Can Help," *IEEE Trans. Mob. Comput.*, vol. 14, no. 7, pp. 1411–1421, Jul 2015.

[105] C. Sommer, O. Tonguz, and F. Dressler, "Traffic information systems: efficient message dissemination via adaptive beaconing," *IEEE Commun. Mag.*, vol. 49, no. 5, pp. 173–179, May 2011.

[106] N. Slonim and N. Tishby, "Agglomerative Information Bottleneck," *Adv. Neural Inf. Process. Syst.*, pp. 617–623, 2000.

[107] J. Lin, "Divergence measures based on the Shannon entropy," *IEEE Trans. Inf. Theory*, vol. 37, no. 1, pp. 145–151, 1991.

[108] Z. Lou, Y. Ye, and X. Yan, "The Multi-Feature Information Bottleneck with Application to Unsupervised Image Categorization," in *Twenty-Third Int. Jt. Conf. Artif. Intell.*, 2013, pp. 1508–1515.

[109] M. Treiber, A. Hennecke, and D. Helbing, "Congested Traffic States in Empirical Observations and Microscopic Simulations," *Physical Review E*, vol. 62, no. 2, pp. 1805–1824, Aug 2000.

[110] A. Kesting, M. Treiber, and D. Helbing, "General Lane-Changing Model MOBIL for Car-Following Models," *Transportation Research Record: Journal of the Transportation Research Board*, vol. 1999, pp. 86–94, Jan. 2007.

[111] W. C. Jakes, *Microwave mobile communications*. Wiley, 1974.

[112] S. Marple, "Computing the discrete-time 'analytic' signal via FFT," in *Conf. Rec. Thirty-First Asilomar Conf. Signals, Syst. Comput.*, vol. 2, Pacific Grove, CA, USA, 1997, pp. 1322–1325.

[113] M. Pätzold, U. Killat, Y. Li, and F. Laue, "Modeling, analysis, and simulation of nonfrequency-selective mobile radio channels with asymmetrical Doppler power spectral density shapes," *IEEE Trans. Veh. Technol.*, vol. 46, no. 2, pp. 494–507, May 1997.

Die approbierte gedruckte Originalversion dieser Dissertation ist an der TU Wien Bibliothek verfügbar.
The approved original version of this doctoral thesis is available in print at TU Wien Bibliothek.
TU Bibliothek Your knowledge hub WIEN

[114] Xiongwen Zhao, J. Kivinen, P. Vainikainen, and K. Skog, "Characterization of Doppler spectra for Mobile Communications at 5.3 GHz," *IEEE Trans. Veh. Technol.*, vol. 52, no. 1, pp. 14–23, Jan 2003.

[115] I. Tan, W. Tang, K. Laberteaux, and A. Bahai, "Measurement and Analysis of Wireless Channel Impairments in DSRC Vehicular Communications," in *Proc. IEEE Int. Conf. Commun.*, 2008, pp. 4882–4888.

[116] P. Alexander, D. Haley, and A. Grant, "Cooperative Intelligent Transport Systems: 5.9-GHz Field Trials," *Proc. IEEE*, vol. 99, no. 7, pp. 1213–1235, Jul 2011.

[117] L. Bernadó, T. Zemen, F. Tufvesson, A. F. Molisch, and C. F. Mecklenbräuker, "Delay and Doppler Spreads of Non-Stationary Vehicular Channels for Safety Relevant Scenarios."

Die approbierte gedruckte Originalversion dieser Dissertation ist an der TU Wien Bibliothek verfügbar.
The approved original version of this doctoral thesis is available in print at TU Wien Bibliothek.